

Error correction of parity-encoding-based annealing through post-readout decoding

Yoshihiro Nambu

*NEC-AIST Quantum Technology Cooperative Research Laboratory
National Institute of Advanced Industrial Science and Technology*

Lechner, Hauke, and Zoller proposed a parity-encoded spin-embedding scheme for quantum annealing (QA) with all-to-all connectivity to avoid the issue of limited connectivity in near-term QA hardware and to enable the implementation thereof using only geometrically local interactions between spins fabricated on the planar substrate. Nevertheless, the redundant encoding of logical information, i.e., using a large number of spins to embed the logical information, increases the computational cost and reduces the efficiency. In this study, we show through Monte Carlo simulation that this redundant encoding may be exploited to solve the problems of the inefficiency and computational cost of the parity-encoded scheme by incorporating appropriate decoding, namely classical post-processing, of the spins to retrieve the logical information. Our findings open up the possibility of parity-encoded schemes for realizing the QA with near-term quantum technologies.

I. INTRODUCTION

In recent years, there has been a growing demand to solve industry-relevant combinatorial optimization problems. It is well known that such problems can be recast as a sampling of the ground state of the Ising spin Hamiltonian, where the problem is encoded in the coupling coefficients of the spin pairs [1]. Many studies have been devoted to nature-inspired approaches to sample the ground state efficiently, such as quantum annealing (QA) [2]. However, coding an arbitrary optimization problem into Ising models requires the dataset of the coupling coefficients between arbitrary pairs of spins in the Ising spin Hamiltonian, and solving them using QA computers is highly demanding for near-term QA devices. This is because it requires a physical implementation of the long-range interaction between any pair of spins. To avoid this problem, several schemes, such as minor embedding (ME) [3, 4] and parity-encoded (PE) schemes, have been proposed [5], which logically embed the spins into a larger physical spin system to avoid long-range interactions.

In the ME scheme, each fully connected spin (logical spin) is encoded on an associated chain of physical spins, and physical spins belonging to the same chain are connected by strong ferromagnetic interactions to align them energetically. Long-range interactions between logical spins are replaced by short-range interactions between chains of physical spins. As a result, a general Ising problem that is defined on a fully connected graph of many nodes can be described by an equivalent problem that is defined on a sparse graph with a larger number of nodes [6]. In contrast, in the PE scheme, which was first proposed by Surlas [7] and later by Lechner, Hauke, and Zoller (LHZ) [5], the parity of each pair of logical spins is encoded on an associated physical spin that is arranged on a two-dimensional lattice. Four nearest-neighbor physical spins are coupled by four-body interactions and constitute a PE spin network. Although this approach can avoid long-range interactions, it requires four-body interactions, which appears physically unnatural and

unfeasible. However, Puri et al. later suggested that the PE spin network is realizable by mapping it to a network of two-photon-driven Kerr parametric oscillators (KPOs) with only local interactions, where a four-body interaction is mapped to a four-wave mixing of four-mode oscillator fields in the Josephson junction coupler [8]. Such a network of KPOs can be implemented using a circuit QED platform employing superconducting devices, which has been studied extensively to realize quantum computing with the current noisy intermediate-scale quantum devices [5, 9]. The KPOs have been experimentally realized by using trapped ions [10] and Josephson parametric oscillators [11–14]. A network of two KPOs has been recently realized using a static capacitive coupling [15]. Chancellor, Zohren, and Warburton independently designed a four-body coupling of a superconducting flux quantum bit (qubit), which is a more naive model of the quantum spin, using additional ancillary qubits [16]. In the PE scheme, the optimization problem is encoded in the dataset of the magnitudes as well as orientations of the local fields that act independently on each physical spin, whereas problem-independent four-body couplings among the neighboring physical spins enforce the parity constraints.

In this study, we investigated another aspect of the PE scheme, that is, its error-correcting capability, by comparing it with that of the quantum annealing correction (QAC) scheme [6, 17–24]. QAC is a QA system that is merged with the classical repetition code to mitigate the errors arising in the QA algorithm. Its error-correcting capability has been discussed in terms of that of the classical repetition code. The error-correcting capability of the PE scheme is more subtle. LHZ suggested that the PE scheme includes intrinsic fault tolerance because the logical spins are encoded redundantly and nonlocally in the physical spins. Pastawski and Preskill suggested that the PE scheme can be viewed as a classical low-density parity-check (LDPC) code that makes the scheme highly robust against weakly correlated spin-flip noise [25]. However, a numerical study using simulated QA and parallel tempering showed no clear evidence that intrinsic fault

tolerance can be used to improve the sampling efficiency of the ground state of logical spins [9]. To elucidate this inconsistency, we conducted discrete-time Markov chain Monte Carlo (DT-MCMC) simulations to sample the sequence of state of physical spins under various constant simulation parameters. As our MCMC is reversible, the sequence converges with the stationary distribution related to the Boltzmann distribution. Through the MCMC simulation, we stored the states of the physical spins sampled during the MCMC iteration in the buffer memory. After completing the simulation, we decoded the physical state using one-step majority vote decoding (one-step MVD) [26–30] to infer the state of the logical spins and calculated their energies for all the elements in the stored sequence of the physical states. Their energy spectra indicated that a substantial number of non-code states contributed to the logical ground state after the decoding. In particular, we found that the optimal simulation parameters for sampling the physical ground state using no post-readout decoding and the logical ground states using one-step MVD are very different.

We investigated our one-step MVD in detail and unfortunately found a drawback in that our method is not robust, that is, its performance is dependent on the problem instance. However, this drawback can be addressed by modifying the algorithm to consider high-weight parity-check constraints. We explain the necessary modification to solve the problem and demonstrate that the error-correcting capability of the algorithm is improved. We speculate that an unfair choice of a member of spin variables for majority voting or inadequate selection of simulation parameters may account for the inconsistent conclusions of previous studies and our study.

The remainder of this paper is organized as follows. In Sec. II, we introduce the formulation known as soft annealing [7], which explains how to incorporate error-correcting codes with logical spin systems and obtain larger physical spin systems. In this formalism, prior knowledge of the parity constraints that characterize the codes are naturally incorporated into the Hamiltonian of the physical spin systems. In Sec. III, we discuss the post-readout decoding. We consider one-step MVD as an example and explain how the prior knowledge about parity constraints can be used to infer the correct result. In Sec. IV, we demonstrate the results of the simulation of one-step MVD when it is applied to the PE scheme. We also propose a novel method for improving the efficiency and robustness of one-step MVD for PE schemes. Section V concludes the paper. In addition, we describe our simulation method, i.e., rejection-free Markov chains, in detail in the Appendix.

II. CLASSICAL ERROR-CORRECTING CODE AND SOFT ANNEALING

Before starting our discussion, we must address two major viewpoints regarding the error-correcting codes considered in this study. One is the communication application viewpoint, where the mathematical model is discussed in terms of a collection of bits or symbols. The other is the optimization application viewpoint, where the mathematical model is discussed in terms of a system of spins or qubits. The purpose of this study is to examine how the findings obtained by the former can be extended to the latter. The concepts used in these two viewpoints have one-to-one correspondence. Figure 1 provides an overview of the correspondence between the concepts used in the two viewpoints for the reader’s reference. For example, “source word” and “code word,” which are concepts used in the communication application viewpoint, are associated with “logical spins” and “physical spins” used in the optimization application viewpoint, respectively. We begin our discussion by introducing the concept of soft annealing proposed by Sourlas [7, 31, 32]. In this proposal, the formulation of the error-correcting codes given by a collection of bits or symbols is mapped to the formulation given by a system of spins or qubits. Based on this mapping, we discuss the constructive contribution of error-correcting codes to the optimization application.

A. Soft annealing

Sourlas established a mathematical equivalence between the classical error-correcting codes and spin-glass models for an arbitrary code [7, 31, 32]. In this study, we address two error-correcting codes relevant to QA: the classical repetition code and the PE scheme. We briefly introduce the formulation proposed by Sourlas. Let us focus on linear codes, which comprise the most important family of error-correcting codes [29, 30]. Suppose that each information message consists of a sequence of K bits and is represented by the binary vector $\mathbf{u} = (u_1, \dots, u_K) \in \{0, 1\}^K$, which is called the source word. We assume that we have no prior information on the choice of the source word, so that a prior probability $P(\mathbf{u})$ is uniform over \mathbf{u} (ignorance prior distribution). The source word is encoded into a redundant sequence of $N (> K)$ bits represented by the binary vector $\mathbf{c} = (c_1, \dots, c_N) = \mathbf{u}\mathbf{G} \pmod{2} \in \{0, 1\}^N$. The vector \mathbf{c} is called code word and a $K \times N$ Boolean matrix \mathbf{G} is the generating matrix of the code. The matrix equation $\mathbf{c} = \mathbf{u}\mathbf{G} \pmod{2}$ consists of N independent scalar equations

$$c_i = \bigoplus_{j=1}^K u_j G_{ji} \in \{0, 1\} \quad (i = 1, \dots, N), \quad (1)$$

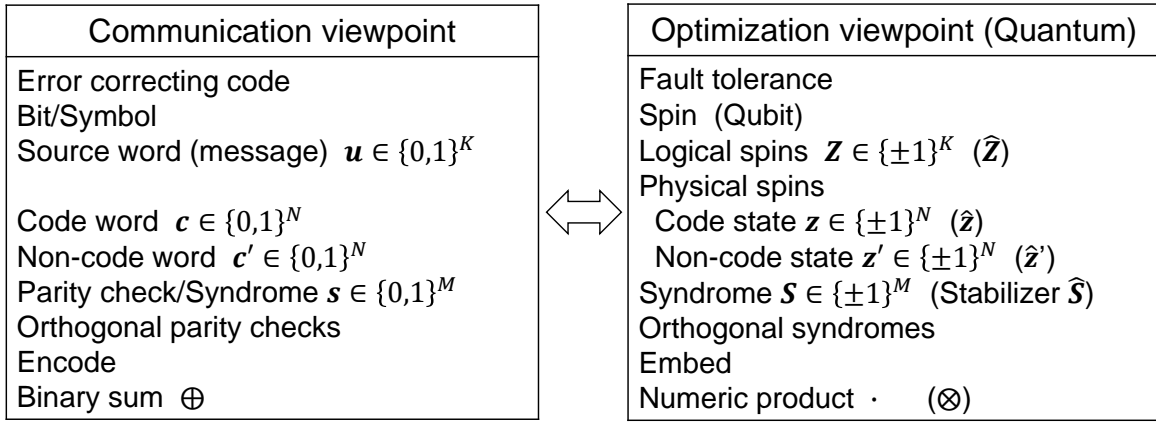


FIG. 1. One-to-one correspondence between the concepts used in the two viewpoints discussed in this paper. Left hand side: concepts used in the communication application viewpoint. Right hand side: concepts used in the optimization application viewpoint. The symbolic notations used in this paper are also shown for the reader's reference. The symbols in parentheses are used in the quantum mechanical version.

where \oplus denotes the Boolean (modulo-2) sum. We consider the linear block code C , where the code word \mathbf{c} consists of a source word \mathbf{u} and $N - K$ redundant parity check bits. We assume that $c_i = u_i$ ($i = 1, \dots, K$), that is, \mathbf{c} is arranged so that its first K bits contain the source word \mathbf{u} and the remaining $N - K$ bits contain the redundant parity check bits. Thus, \mathbf{G} has the following form: $\mathbf{G} = [I_K, P]$, where I_K is a $K \times K$ identity matrix and P is a $K \times (N - K)$ matrix [29, 30]. The ratio $R = K/N < 1$ characterizes the redundancy of the code and is called the rate of the code. The N components c_i in the code word \mathbf{c} are not independent. Among all 2^N code words, only 2^K words have one-to-one correspondence with the source words. Code words must satisfy the constraint $\mathbf{c}\mathbf{H}^T = (0, \dots, 0) = \mathbf{0} \pmod{2}$, where \mathbf{H} is an $(N - K) \times N$ Boolean matrix and is called a parity check matrix. The constraints are called parity check equations and comprise $N - K$ independent scalar equations.

$$\bigoplus_{j=1}^N H_{ij}c_j = 0 \quad (i = 1, \dots, N - K). \quad (2)$$

Owing to these constraints, the prior probability $P(\mathbf{c})$ may depend on the parity check bits in the code word \mathbf{c} , and its distribution reflects the information regarding the choice of code words \mathbf{c} .

Suppose that \mathbf{c} is transmitted through a noisy communication channel and received as $\mathbf{r} = (r_1, \dots, r_N) = \mathbf{c} \oplus \mathbf{e} \in \{0, 1\}^N$, where $\mathbf{e} = (e_1, \dots, e_N) \in \{0, 1\}^N$ denotes the error pattern. We call $\mathbf{s} = (s_1, \dots, s_{N-K}) = \mathbf{r}\mathbf{H}^T \in \{0, 1\}^N$ the syndrome pattern. It should be noted that the syndrome pattern \mathbf{s} depends only on the error pattern \mathbf{e} as $\mathbf{s} = \mathbf{e}\mathbf{H}^T$, and any element in \mathbf{s} is 0 if and only if \mathbf{r} is a code word [26, 29, 30].

The connection between the error-correcting codes and statistical physics of a spin network is established

based on isomorphism between the additive Boolean group $(\{0, 1\}, \oplus)$ and multiplicative bipolar (Ising) group $(\{\pm 1\}, \cdot)$. The source word \mathbf{u} is mapped to the bipolar vector $\mathbf{Z} = (Z_1, \dots, Z_K) \in \{\pm 1\}^K$ by $Z_i = (-1)^{u_i} \in \{\pm 1\}$, and $Z_i Z_j = (-1)^{u_i \oplus u_j}$. Similarly, the code word \mathbf{c} is mapped to the bipolar vector $\mathbf{z} = (z_1, \dots, z_N) \in \{\pm 1\}^N$ by $z_i = (-1)^{c_i}$, and $z_i z_j = (-1)^{c_i \oplus c_j}$. It follows that

$$z_i = (-1)^{\bigoplus_{j=1}^K u_j G_{ji}} = C_{k_1 \dots k_p}^i \prod_{l=1}^p Z_{k_l} \in \{\pm 1\} \quad (i = 1, \dots, N; 1 \leq p \leq K). \quad (3)$$

Note that $z_i = (-1)^{u_i}$ for $i = 1, \dots, K$ according to our convention. As noted previously, we regard Z_i and \mathbf{Z} as a logical spin variable and state of K logical spins, respectively. Similarly, we regard z_i and \mathbf{z} as a physical spin variable and state of N physical spins, respectively. Equation (3) defines the physical spin state \mathbf{z} in terms of the Boolean matrix \mathbf{C} and logical spin state \mathbf{Z} ; it describes the embedding of the K logical spin system into a larger N ($> K$) physical spin system. The matrix defined by the elements $C_{k_1 \dots k_p}^i$ is called the ‘‘connectivity matrix.’’ It defines the codes and describes how the i th physical spin state z_i depends on the logical spin state \mathbf{Z} . The element $C_{k_1 \dots k_p}^i$ is 1 if c_i is the Boolean sum of u_{k_l} ($l = 1, \dots, p$). Thus, a parity-check bit in the linear code C that is formed by the Boolean sum of p bits of the form $\bigoplus_{l=1}^p u_{k_l}$ is mapped onto a p -spin coupling $\prod_{l=1}^p Z_{k_l}$. (Each logical spin variable Z_{k_l} is understood to appear only once in the i th physical spin variable z_i .)

Similarly, the parity check equations can be rewritten

in terms of the physical state \mathbf{z} :

$$S_i(\mathbf{z}) = (-1)^{\bigoplus_{j=1}^N H_{ij} c_j} = M_{k_1 \dots k_q}^i \prod_{l=1}^q z_{k_l} = +1$$

$$(i = 1, \dots, N - K; 1 \leq q \leq N). \quad (4)$$

This defines the Boolean matrix \mathbf{M} called the ‘‘parity constraint matrix’’ that is associated with the parity check matrix \mathbf{H} of the code. $M_{k_1 \dots k_q}^i$ is 1 if each parity equation consists of the Boolean sum of c_{k_l} ($l = 1, \dots, q$). The physical state \mathbf{z} that satisfies Eq. (4) is called a code state. For the general physical state \mathbf{z}' , we refer to $S_i(\mathbf{z}')$ syndrome, which is the classical counterpart of the stabilizer operator defined in terms of the quantum correcting codes [17, 33]. In some studies, it is also called the parity check in the context of the communication application [26, 27].

Sourlas discussed decoding of the classical error-correcting codes based on statistical inference according to the Bayes theorem. Based on the above connection, the physical spin state \mathbf{z} before being exposed to a noisy environment can be inferred from the physical spin state that is corrupted by the environment by analyzing the statistical physics of the associated spin network. Suppose that the i th physical spin is prepared in the state $z_i \in \{\pm 1\}$ and exposed to an environment. Then, the spin may be corrupted and measured to be, in general, a real number J_i . This process is stochastic and statistical by nature. The purpose of the error-correcting codes is to infer the logical spin state \mathbf{Z} from the readout $\mathbf{J} = (J_1, \dots, J_N)$ of the physical spin state as faithfully and efficiently as possible by exploiting the information on the statistical property of the environment and redundancy in the physical spin state \mathbf{z} . To this end, we consider the conditional probability $P(\mathbf{z}|\mathbf{J}) d\mathbf{J}$ that the prepared state is \mathbf{z} when the observed readout is between \mathbf{J} and $\mathbf{J} + d\mathbf{J}$. According to the Bayesian inference, the Bayes-optimal estimate is obtained when we maximize $P(\mathbf{z}|\mathbf{J})$, called the posterior probability, or its sidelight that is discussed later. The Bayes theorem states that

$$P(\mathbf{z}|\mathbf{J}) = \frac{P(\mathbf{J}|\mathbf{z}) P(\mathbf{z}) P(\mathbf{Z})}{\sum_{\mathbf{z}} P(\mathbf{J}|\mathbf{z}) P(\mathbf{z}) P(\mathbf{Z})}$$

$$= \kappa P(\mathbf{J}|\mathbf{z}) P(\mathbf{z}) P(\mathbf{Z}), \quad (5)$$

where κ is a constant independent of \mathbf{z} , which is to be determined by the normalization condition $\sum_{\mathbf{z}} P(\mathbf{z}|\mathbf{J}) = 1$. $P(\mathbf{z})$ and $P(\mathbf{Z})$ are the prior probabilities for the physical spin state \mathbf{z} and logical spin state \mathbf{Z} , respectively [34]. In the present scenario, we assume an informative prior for the parity constraints of the physical spin state \mathbf{z} but ignorance prior for the logical spin state \mathbf{Z} , that is,

$$P(\mathbf{z}) = \mu \prod_{l=1}^{N-K} \delta(S_l(\mathbf{z}), +1), \quad (6)$$

and $P(\mathbf{Z}) = \text{const.}$, where μ is a normalization constant and $\delta(i, j)$ is Kronecker’s delta. $P(\mathbf{J}|\mathbf{z})$ is called the

likelihood, which describes the statistical property of the environmental noise and is supposed to be known. In addition, the environmental noise is supposed to be identical and independent of z_i (a ‘‘memoryless or Markovian noise model’’), i.e.,

$$P(\mathbf{J}|\mathbf{z}) = \prod_{i=1}^N P(J_i|z_i), \quad (7)$$

where $P(J_i|z_i)$ is called the extrinsic likelihood.

Maximizing the posterior probability $P(\mathbf{z}|\mathbf{J})$ is equivalent to maximizing log posterior probability expressed by

$$L(\mathbf{z}, \mathbf{J}) = \log P(\mathbf{z}|\mathbf{J})$$

$$= \sum_{i=1}^N L_c(J_i, z_i) + \sum_{i=1}^{N-K} L_p(z_i) + \text{const.}, \quad (8)$$

where $L_c(J_i, z_i)$ and $L_p(z_i)$ are the extrinsic log-likelihood and log-posterior probability, respectively, and are defined as

$$L_c(J_i, z_i) = \log P(J_i|z_i)$$

$$= \frac{1}{2} \log P(J_i|z_i = +1) P(J_i|z_i = -1)$$

$$+ \frac{z_i}{2} \log \frac{P(J_i|z_i = +1)}{P(J_i|z_i = -1)}$$

$$= K_i z_i + c_2, \quad (9)$$

$$L_p(z_i) = \log P(z_i) = \log \delta(S_i(\mathbf{z}), +1), \quad (10)$$

$$K_i = K_i(J_i) = \frac{1}{2} \log \frac{P(J_i|z_i = +1)}{P(J_i|z_i = -1)}, \quad (11)$$

where c_2 is a constant independent of z_i . K_i is called the extrinsic log-likelihood ratio (LLR) in the coding theory. It should be noted that maximizing $P(\mathbf{z}|\mathbf{J})$ is equivalent to maximizing $L(\mathbf{z}, \mathbf{J})$ because $\log x$ is a monotonically increasing function of x . $L_p(z_i)$ describes the parity constraints for z_i ($i = 1, \dots, N - K$) and is independent of J_i that may be corrupted by environmental noise, whereas $L_c(J_i, z_i)$ describes the noise property and depends on the relationship between the two types of information, z_i and J_i , which were prepared and measured, respectively.

To present the concrete expression for K_i , we need to specify a model for the environmental noise. We address two examples of a symmetric channel having a common property

$$P(J_i|z_i) = P(-J_i|-z_i). \quad (12)$$

The first is the binary symmetric channel

$$\begin{cases} P(J_i|z_i) = (1 - p_i) \delta(J_i, z_i) + p_i \delta(J_i, -z_i) \\ K_i = \frac{J_i}{2} \ln \frac{1-p_i}{p_i} = \beta_i J_i \end{cases}, \quad (13)$$

where $0 \leq p_i \leq 1$. The other example is the additive white Gaussian noise channel

$$\begin{cases} P(J_i|z_i) = \frac{1}{\sqrt{2\pi w_i}} \exp\left[-\frac{(J_i - v_i z_i)^2}{2w_i^2}\right] \\ K_i = \frac{v_i}{w_i^2} J_i = \beta_i J_i \end{cases}, \quad (14)$$

where v_i and w_i^2 are the amplitude of the prepared signal $v_i z_i$ and variance of the Gaussian noise for the i th physical spin, respectively. The parameter β_i is called the inverse temperature.

Sourlas eventually deduced two different types of spin Hamiltonians associated with the error-correcting codes. The first is written in terms of only the variables associated with the logical spins $\mathbf{Z} = (Z_1, \dots, Z_K) = (z_1, \dots, z_K)$, as follows:

$$\begin{aligned} H^{\text{logi}}(\mathbf{Z}) &= -L(\mathbf{z}, \mathbf{J}) \\ &= -\sum_{i=1}^N L_c \left(C_{k_1 \dots k_p}^i \prod_{l=1}^p z_{k_l}, J_i \right) \\ &= -\sum_{i=1}^N \beta_i J_i C_{k_1 \dots k_p}^i \prod_{l=1}^p Z_{k_l}, \end{aligned} \quad (15)$$

which is obtained by expressing the physical spin state \mathbf{z} in terms of the logical spin state \mathbf{Z} . In Eq. (15), we have omitted an unimportant constant term for the present discussion. $H^{\text{logi}}(\mathbf{Z})$ obviously has the form of a spin Hamiltonian with p -body interactions. The distribution of the coupling coefficients is determined by the extrinsic LLR K_i . In contrast, the second type of spin Hamiltonian is expressed in terms of the variables associated with the physical spins \mathbf{z} :

$$\begin{aligned} H^{\text{phys}}(\mathbf{z}) &= -L(\mathbf{z}, \mathbf{J}) \\ &= -\sum_{i=1}^N L_c(z_i, J_i) - \sum_{i=1}^{N-K} L_p(z_i) \\ &= -\sum_{i=1}^N \beta_i J_i z_i \\ &\quad + \lim_{\gamma \rightarrow \infty} \gamma \sum_{i=1}^{N-K} \frac{1 - S_i(\mathbf{z})}{2}, \end{aligned} \quad (16)$$

where we have used the identity

$$\delta(x, +1) = \lim_{\gamma \rightarrow \infty} \exp\left[-\gamma \frac{1-x}{2}\right] \quad (17)$$

to replace the δ in $L_p(z_i)$ with an associated soft constraint given by the second term of Eq. (16). We have also omitted an unimportant constant term in Eq. (16). $H^{\text{phys}}(\mathbf{z})$ describes a spin system with infinite ferromagnetic couplings and couplings with local magnetic fields. It should be noted that the space of the logical spin state \mathbf{Z} and that of the physical spin state \mathbf{z} differ, e.g., the dimension of \mathbf{Z} is K , whereas that of \mathbf{z} is $N (> K)$. Therefore, the state space associated

with $H^{\text{phys}}(\mathbf{z})$ is larger than that of $H^{\text{logi}}(\mathbf{Z})$. The code space is the space of the degenerated ground states of the Hamiltonian $H^{\text{pen}}(\mathbf{z}) = \sum_{i=1}^{N-K} \frac{1 - S_i(\mathbf{z})}{2}$ in Eq. (16), which satisfies $N - K$ soft constraints $S_i(\mathbf{z}) = +1$ ($i = 1, \dots, N - K$). It has 2^K -degeneracy, which agrees with the state space of $H^{\text{logi}}(\mathbf{Z})$. This penalty Hamiltonian $H^{\text{pen}}(\mathbf{z})$ originates from the informative prior for parity constraints and suppresses the excitation outside the code space.

We note that a set of the syndromes has one-to-one correspondence with a set of mutually commuting stabilizer generators $\hat{\mathbf{S}}(\hat{\mathbf{z}}) = \{\hat{S}_1(\hat{\mathbf{z}}), \dots, \hat{S}_{N-K}(\hat{\mathbf{z}})\}$ of the stabilizer group in a quantum-mechanical context, if we identify the classical bipolar variables Z_i and z_i with the quantum mechanical Pauli- z operators \hat{Z}_i and \hat{z}_i . (We designate the quantum mechanical non-commuting operator as $\hat{\cdot}$.) Consider the logical basis state $\{|0_L\rangle, |1_L\rangle\}^K$, which is the eigenspace of $\hat{S}_i(\hat{\mathbf{z}})$ associated with the eigenvalue $+1$ for $i = 1, \dots, N - K$. The code space is spanned by the basis state $\{|0_L\rangle, |1_L\rangle\}^K$ and is a 2^K -dimensional subspace of the space of the physical spin state as well as the 2^K -degenerated ground states of the quantum mechanical Hamiltonian $\hat{H}^{\text{pen}}(\hat{\mathbf{z}}) = \sum_{i=1}^{N-K} \frac{1 - \hat{S}_i(\hat{\mathbf{z}})}{2}$. The code space projector can be written in terms of the stabilizer generators: $\hat{P}_c(\hat{\mathbf{z}}) = \prod_{i=1}^K (|0_L\rangle\langle 0_L| + |1_L\rangle\langle 1_L|)_i = \prod_{i=1}^{N-K} \frac{1 + \hat{S}_i(\hat{\mathbf{z}})}{2}$. Its orthogonal complement $\hat{P}_{nc}(\hat{\mathbf{z}}) = \hat{I} - \hat{P}_c(\hat{\mathbf{z}})$ defines the complementary non-code space. The family of stabilizers $\hat{\mathbf{S}}(\hat{\mathbf{z}})$ defines the stabilizer codes, which can correct only the spin-flip error, as the spin-flip error operator (Pauli- x operator) \hat{x}_k for any physical spin k anti-commutes with at least one stabilizer generator $\hat{S}_i(\hat{\mathbf{z}})$. A collection of the syndrome subspaces is defined according to the set of eigenvalues of $\hat{\mathbf{S}}(\hat{\mathbf{z}})$. Note that because the stabilizer operator $\hat{S}_i(\hat{\mathbf{z}})$ multiplied by another operator $\hat{S}_j(\hat{\mathbf{z}})$ is also a stabilizer operator (any binary sum of parity checks is also a parity check from the classical communication perspective), it follows that the parity check matrix \mathbf{H} and associated parity constraint matrix \mathbf{M} are not unique. This gives us freedom of choice of the stabilizer operator $\hat{S}_i(\hat{\mathbf{z}})$ as well as its classical counterpart, i.e., syndrome $S_i(\mathbf{z})$. Later, we shall use this fact to discuss the method for encoding and decoding the physical spin state.

B. Classical repetition code

As an illustrative example of soft annealing, let us consider the classical repetition code that is a simple but important example of linear block codes. The classical repetition code encodes one bit of information into n bits. From the optimization application viewpoint,

one bit of information is embedded into n physical spins. The minimum code distance can be increased by repeating the logical information several times, which helps to mitigate errors in the physical spins. An (n, k, d) linear block code (encoding k logical spins (source word) into n physical spins (code word) and with a code distance d) can be defined by a set of syndromes \mathbf{S} . We consider the case of the $(n, k) = (N, 1)$ repetition code, where a state Z of a single logical spin is encoded to form N physical spin states $\mathbf{z} = (z_1, \dots, z_N)$ with $z_1 = Z$. This code can be defined by the set of syndromes $S_i(\mathbf{z}) = z_1 z_{i+1}$ ($i = 1, \dots, N-1$). Note that we can consider another set of syndromes $S'_i(\mathbf{z}) = z_i z_{i+1}$ ($i = 1, \dots, N-1$) under freedom of choice as $S'_i(\mathbf{z}) = S_{i-1}(\mathbf{z}) S_i(\mathbf{z})$. This code can correct up to $t = \lfloor \frac{d}{2} \rfloor$ errors and can be reliably decoded using one-step MVD if the number of errors does not exceed t , which is discussed later. In the quantum-mechanical context, z_i is identified with the Pauli- z operator \hat{z}_i of the i th physical spin and $\hat{S}_i(\hat{\mathbf{z}}) = \hat{z}_1 \hat{z}_{i+1}$ ($i = 1, \dots, N-1$). Such a quantum repetition bit-flip code has the logical basis state

$$|0_L\rangle = \prod_{i=1}^N |0\rangle_i; |1_L\rangle = \prod_{i=1}^N |1\rangle_i, \quad (18)$$

where $|0\rangle_i$ and $|1\rangle_i$ denote the eigenstates of \hat{z}_i associated with the eigenvalues -1 and $+1$, respectively. The basis $\{|0_L\rangle, |1_L\rangle\}$ spans the space of the code state for the repetition spin-flip code, which is the eigenspace of $\hat{S}_i(\hat{\mathbf{z}})$ associated with the eigenvalue $+1$ for $i = 1, \dots, N-1$, as well as the degenerate ground states of $\hat{H}^{pen}(\hat{\mathbf{z}}) = \sum_{i=1}^{N-1} \frac{1 - \hat{S}_i(\hat{\mathbf{z}})}{2}$. The logical Pauli operators are defined as operators that preserve the space of the code state and have the same effect on the logical basis states as their corresponding Pauli operators have on the corresponding basis states. They are expressed as

$$\hat{Z}_L = \hat{z}_1 \text{ and } \hat{X}_L = \prod_{i=1}^N \hat{x}_i, \quad (19)$$

which commute with all stabilizers \hat{S}_i as well as the projector for the space of the code states $\hat{P}_c(\hat{\mathbf{z}}) = |0_L\rangle\langle 0_L| + |1_L\rangle\langle 1_L| = \prod_{i=1}^{N-1} \frac{1 + \hat{S}_i(\hat{\mathbf{z}})}{2}$, and satisfy the anti-commutation relation $\{\hat{X}_L, \hat{Z}_L\} = 0$. The logical Pauli- x operator \hat{X}_L is the product of N Pauli- x operators (N -body interaction) acting on the physical spins, which is to be expected because $d = N$ [6, 21].

The merit of this code is that its physical Hamiltonian $H^{phys}(\mathbf{z})$ can be realized using up to two-body interactions. These operators should be compared with the logical operators for the PE scheme, as demonstrated in the following discussion. We note that QAC [6, 17–24] uses this quantum repetition spin-flip code as its building block. We revisit this point later.

C. Parity encoding

We consider another interesting example. Sourlas proposed an advantage of using $H^{phys}(\mathbf{z})$ instead of $H^{logi}(\mathbf{Z})$ to solve optimization problems [7]. It was suggested that the computational difficulties of some hard optimization problems may be alleviated by embedding the original system into a larger system and imposing necessary soft constraints, where the weight γ of the constraints term in $H^{phys}(\mathbf{z})$ is assumed to be a large yet finite value, to reduce the enlarged system to the original system. This proposal, called soft annealing, was based on the empirical observation that it is easier to minimize $H^{phys}(\mathbf{z})$ rather than $H^{logi}(\mathbf{Z})$, despite the fact that the number of variables is much larger for $H^{phys}(\mathbf{z})$. Sourlas provided intuitive explanations; for example, in a large-dimensional space, it is possible to circumvent barriers to find the minimum, which makes the optimization easier. It was pointed out that the PE schemes

$$H^{phys}(\mathbf{z}) = \beta H^{loc}(\mathbf{z}) + \gamma H^{pen}(\mathbf{z}), \quad (20)$$

where $\beta, \gamma > 0$, and

$$H^{loc}(\mathbf{z}) = \sum_{\langle i, j \rangle} J_{ij} z_{ij}, \quad (21)$$

$$H^{pen}(\mathbf{z}) = \sum_{\text{plaquettes}} \frac{1 - S_{ij}(\mathbf{z})}{2}, \quad (22)$$

with $S_{ij}(\mathbf{z}) = S_{ij}^{4w}(\mathbf{z}) = z_{ij} z_{i+1} z_{j+1} z_{i+1} z_{j+1}$, where $1 \leq i < j \leq K-1$ [35], are nontrivial examples of the soft annealing of a spin-glass model with all-to-all two-body interactions, i.e.,

$$H^{logi}(\mathbf{Z}) = \beta \sum_{\langle i, j \rangle} J_{ij} Z_i Z_j, \quad (23)$$

where $\sum_{\text{plaquettes}}$ runs over all plaquettes, i.e., the elementary squares, of the lattice of physical spins, whereas $\sum_{\langle i, j \rangle}$ runs over all spin pairs (i, j) taken from all logical spins.

Here, we consider an extended layout shown in Fig. 2 with an additional row of physical spins, which have a direct correspondence to logical spins, that is, $z_{0i} = Z_i$ ($i = 1, \dots, K$) for the case of $K = 7$ [36–38]. Without this row, the layout of the physical spins is reduced to the original LHZ layout that is fully consistent with the Hamiltonian $H^{phys}(\mathbf{z})$ [5]. With the addition of this row, we can incorporate the local interaction terms originating from the local field h_i for $1 \leq i \leq K$. In this figure, the green circles indicate the spins associated with the K logical spins z_{0i} ($1 \leq i \leq K$), whereas the blue circles indicate the physical spins z_{ij} ($1 \leq i < j \leq K$). Note that the brown circles are ancillary spins whose

states are fixed to the spin-up ($z_{ii} = +1$) states. If we omit the ancillary spins, the system has a total of $N = \frac{K(K+1)}{2}$ spins with K logical spins and $N - K = \frac{K(K-1)}{2}$ physical spins, so that $(n, k) = (N, K)$. The system should have $N - K$ parity constraints for the logical and physical spins. For example, we can consider $N - K$ weight-three parity-check equations $S_{ij}^{3w}(\mathbf{z}) = z_{0i}z_{0j}z_{ij} = +1$ ($1 \leq i < j \leq K$). Although S_{ij}^{3w} differs from S_{ij}^{4w} , we can observe that the parity constraints $S_{ij}^{3w} = +1$ and $S_{ij}^{4w} = +1$ are consistent because $S_{ij}^{4w} = S_{ij}^{3w}S_{i,j+1}^{3w}S_{i+1,j}^{3w}S_{i+1,j+1}^{3w}$ for any $1 \leq i < j \leq K - 1$. This is a consequence of the freedom of choice of syndromes. The physical spins of the four corners around each small red solid circle in Fig. 2 define all elements S_{ij}^{4w} , which are called plaquettes. In addition, it should be remembered that if $h_i = 0$ for $1 \leq i \leq K$, only a random local field J_{ij} acts on the physical spins, which justifies the use of the ignorance prior for the readout of the logical spin state \mathbf{Z} for error correction. Therefore, provided that the local fields are absent in Eq. (23), it is sufficient to consider only the physical spins bounded by the red broken line in Fig. 2, which is simply the original LHZ layout. In this case, we have the $(n, k) = (N - K, K - 1) = (K(K - 1)/2, K - 1)$ linear block code, which means that only $K - 1$ physical variables are logically independent, i.e., we can determine \mathbf{Z} only up to a global spin flip.

Let us examine how the PE spin network is described in the quantum-mechanical context. We introduce the concept of logical lines Q_i , or constraint-preserving driver lines [37], which define the subsets of the physical operators that preserve the space of the code state and have one-to-one correspondence with the Pauli operators on the logical spins [36–41]. Consider the Pauli- z operators \hat{z}_{ij} that are associated with the physical spins in the PE spin network. We consider the following $(K + 1) \times (K + 1)$ symmetric matrix with Pauli- z operators as the entries for the relevant spins arranged consistently with the PE spin network shown in Fig. 2,

$$\hat{\mathbf{z}} = \begin{bmatrix} \hat{1} & \hat{z}_{01} & \hat{z}_{02} & \hat{z}_{03} & \cdots & \hat{z}_{0K-1} & \hat{z}_{0K} \\ \hat{z}_{10} & \hat{1} & \hat{z}_{12} & \hat{z}_{13} & \cdots & \hat{z}_{1K-1} & \hat{z}_{1K} \\ \hat{z}_{20} & \hat{z}_{21} & \hat{1} & \hat{z}_{23} & \cdots & \hat{z}_{2K-1} & \hat{z}_{2K} \\ \hat{z}_{30} & \hat{z}_{31} & \hat{z}_{32} & \hat{1} & \cdots & \hat{z}_{3K-1} & \hat{z}_{3K} \\ \vdots & \vdots & \vdots & \vdots & \ddots & \cdots & \vdots \\ \hat{z}_{K-10} & \hat{z}_{K-11} & \hat{z}_{K-12} & \hat{z}_{K-13} & \cdots & \hat{1} & \hat{z}_{K-1K} \\ \hat{z}_{K0} & \hat{z}_{K1} & \hat{z}_{K2} & \hat{z}_{K3} & \cdots & \hat{z}_{K-1K} & \hat{1} \end{bmatrix}, \quad (24)$$

where $\hat{1}$ is an identity operator acting on a physical spin and $\hat{z}_{ij} = \hat{z}_{ji}$ by construction. $\hat{\mathbf{z}}$ is a matrix with entries given by $N = \frac{K(K+1)}{2}$ projectors associated with the measurement of the configuration of the PE spin network on the computational basis. Each entry \hat{z}_{ij} is observable for the physical spins having two possible eigenstates with eigenvalues ± 1 . Let us consider the Pauli- x operators \hat{X}_i and \hat{x}_{ij} acting on the logical and physical spins, respectively. These Pauli operators satisfy the following

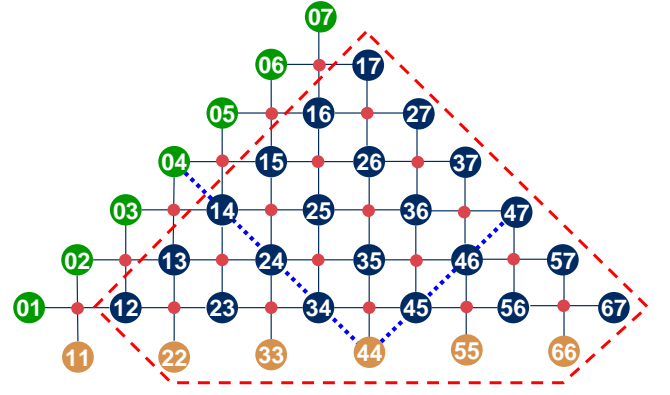


FIG. 2. Original and extended LHZ layouts. The blue and brown circles indicate physical and ancillary spins, respectively. The green circles correspond to logical spins. The label in the circle corresponds to the label specifying a physical spin. The small red solid circles indicate plaquettes associated with S_{ij}^{4w} . The red broken line indicates the original LHZ layout. The blue dotted line indicates the logical line Q_4 .

anti-commutation and commutation relations:

$$\{\hat{X}_i, \hat{Z}_i\} = [\hat{X}_i, \hat{Z}_j] = 0, \quad (25)$$

for $j \neq i$ and

$$\{\hat{x}_{ij}, \hat{z}_{ij}\} = [\hat{x}_{ij}, \hat{z}_{kl}] = 0, \quad (26)$$

$$[\hat{X}_i, \hat{x}_{jk}] = [\hat{Z}_i, \hat{z}_{jk}] = [\hat{X}_i, \hat{z}_{jk}] = [\hat{Z}_i, \hat{x}_{jk}] = 0 \quad (27)$$

for $k \neq i$ or $l \neq j$. We also define $\hat{\mathbf{Z}} = (\hat{Z}_1, \dots, \hat{Z}_K)$. Then, if we replace $Z_i \rightarrow \hat{Z}_i$ and $z_{ij} \rightarrow \hat{z}_{ij}$ for the classical Hamiltonians, the resultant Hamiltonians $\hat{H}^{logi} = \hat{H}^{logi}(\hat{\mathbf{Z}})$ and $\hat{H}^{phys} = \hat{H}^{phys}(\hat{\mathbf{z}})$ are identified with the Hamiltonians in the quantum-mechanical context. Then, we can consider the logical Pauli operators similar to the repetition spin-flip code. It is easy to show that

$$\hat{Z}_{Li} = \hat{Z}_i = \hat{z}_{0i} = \hat{z}_{i0} \text{ and } \hat{X}_{Li} = \prod_{j=0}^{K-1} \hat{x}_{ij} = \prod_{j=0}^{K-1} \hat{x}_{ji} \quad (28)$$

commute with the stabilizer operators

$$\hat{S}_{ij}(\hat{\mathbf{z}}) = \hat{z}_{ij}\hat{z}_{i,j+1}\hat{z}_{i+1,j}\hat{z}_{i+1,j+1} \quad (0 \leq i < j \leq K - 1) \quad (29)$$

as well as the penalty Hamiltonian

$$\hat{H}^{pen}(\hat{\mathbf{z}}) = \sum_{\text{plaquettes}} \frac{1 - \hat{S}_{ij}(\hat{\mathbf{z}})}{2}, \quad (30)$$

and the projector to the space of the code states

$$\begin{aligned}\hat{P}_c(\hat{z}) &= \prod_{\text{plaquettes}} \frac{1 + \hat{S}_{ij}(\hat{z})}{2} \\ &= \prod_{i=1}^K (|0_L\rangle\langle 0_L| + |1_L\rangle\langle 1_L|)_i \\ &= \prod_{i=1}^K (|0\rangle\langle 0| + |1\rangle\langle 1|)_i,\end{aligned}\quad (31)$$

where $|0\rangle_i$ and $|1\rangle_i$ denote the eigenstates of $\hat{Z}_i = \hat{z}_{0i} = \hat{z}_{i0}$ associated with the eigenvalues -1 and $+1$, respectively. The logical Pauli operators satisfy the (anti-) commutation relations

$$\{\hat{X}_{Li}, \hat{Z}_{Lj}\} = [\hat{X}_{Lj}, \hat{Z}_{Li}] = 0 \quad (32)$$

for $i = 1, \dots, K$ with $j \neq i$. We can also confirm that

$$\{\hat{X}_{Li}, \hat{z}_{ij}\} = \{\hat{X}_{Lj}, \hat{z}_{ij}\} = 0. \quad (33)$$

The logical Pauli- x operator \hat{X}_{Li} is determined by the product of K Pauli- x operators associated with physical spins with a label involving i . Such a chain of spins in the PE spin network is called the logical line (or constraint-preserving driver line [37]). The stabilizer operator $\hat{S}_{ij}(\hat{z})$ commutes with $\hat{H}^{phys}(\hat{z})$ and anti-commutes with the spin-flip operators \hat{x}_{ij} for the physical spins involved in the plaquette given in Eq. (29).

Now, let us consider the action of \hat{X}_{Li} on every element of \hat{z} , i.e., $\hat{z} \rightarrow \hat{z}' = \hat{X}_{Li}\hat{z}\hat{X}_{Li}$. The operator \hat{X}_{Li} inverts the sign of the matrix elements of \hat{z} along the $(i+1)$ th row and $(i+1)$ th column except for the diagonal elements collectively. Note that the diagonal element should be preserved as it belongs to both the $(i+1)$ th row and column and its sign is inverted twice. In the Heisenberg picture, this implies that the logical Pauli- x operator \hat{X}_{Li} collectively flips the orientation of the set of $2K$ physical spins in the logical lines. The logical Pauli- x operators \hat{X}_{Li} are counterparts of the logical Pauli- x operator \hat{X}_L of the repetition spin-flip code given in Eq. (19). Such high-weight operators flip all the physical spins associated with a logical spin \hat{Z}_i collectively. The resultant collective operation maps a code state to another code state for both the repetition spin-flip code and PE scheme, as it commutes with the projector to the space of the code states. This implies that the code distance d of K logical spins is expressed by $d = K$ for this extended LHZ layout. Similarly, we obtain $d = K - 1$ for the original LHZ layout. The repetition spin-flip code and parity encoding guarantees correction of up to $t = \lfloor \frac{d-1}{2} \rfloor$ spin-flip errors. We can describe the QA of the PE scheme by combining the standard transverse-field driver Hamiltonian

$$\hat{H}_1^{tr}(\hat{x}) = \kappa \sum_{\langle i,j \rangle} \hat{x}_{ij} \quad (34)$$

with $\hat{H}^{phys}(\hat{z})$ and introducing a temporal dependence for β , γ , and κ , where $\hat{x}_{ji} = \hat{x}_{ij}$ is always assumed for any $1 \leq i < j \leq K$. We may select another transverse-field driver Hamiltonian based on K logical Pauli- x operators [37, 39–42]

$$\hat{H}_2^{tr}(\hat{x}) = \kappa \sum_{i=1}^K \hat{X}_{Li} \neq \hat{H}_1^{tr}(\hat{x}), \quad (35)$$

which requires K -body interactions and is difficult to implement practically using current technologies.

D. QAC

QAC is a heuristic method that was designed to protect the logical spin systems from spin-flip errors by introducing a classical repetition code independently for each spin [6, 17–24]. We investigated QAC to compare it with the PE scheme, as the PE scheme somewhat resembles QAC. The typical layouts of the physical spins in QAC are illustrated in Figs. 3 and 4. We consider K copies of the spin systems, each comprising N spins described by the logical spin Hamiltonian, which we call replicas. Hence, every spin in the logical spin system is accompanied by its $K-1$ replicas. To form a K repetition spin-flip code, the K physical spins are ferromagnetically coupled by two-body interaction to form a logical group associated with the logical spin.

The Hamiltonian for the physical spin system is considered as follows. Suppose we designate a Pauli- z operator for the spin i ($= 1, \dots, N$) in the logical Hamiltonian as \hat{Z}_i . The encoding introduces a new index, k ($= 1, \dots, K$), specifying the replica to which the spin i belongs, so that $\hat{Z}_i \mapsto \hat{z}_{ik}$. Let $\hat{z} = \{\hat{z}_{ik}\}_{i=1, \dots, N, k=1, \dots, K}$ be the set of $N \times K$ physical spin operators. Then, the subsets $\{\hat{z}_{ik}\}_{k=1, \dots, K} \subset \hat{z}$ and $\{\hat{z}_{ik}\}_{i=1, \dots, N} \subset \hat{z}$ correspond to the physical spin operators in the logical group i and in the replica k , respectively. If there is no coupling between the logical spins with different indices i , the logical groups specified by the different i are mutually independent. Then, the physical Hamiltonian of the repetition spin-flip code is expressed as

$$\begin{aligned}\hat{H}^{phys}(\hat{z}) &= \sum_{i=1}^N \left(\beta h_i \sum_{k=1}^K \hat{z}_{i,k} + \gamma \sum_{k=2}^K \frac{1 - \hat{S}_{ik}(\hat{z})}{2} \right) \\ &= \beta \sum_{k=1}^K \sum_{i=1}^N h_i \hat{z}_{i,k} \\ &\quad + \gamma \sum_{i=1}^N \sum_{k=2}^K \frac{1 - \hat{S}_{ik}(\hat{z})}{2},\end{aligned}\quad (36)$$

where $\beta, \gamma > 0$, and

$$\hat{S}_{ik}(\hat{z}) = \hat{z}_{i1} \hat{z}_{ik+1} \quad (k = 1, \dots, K-1), \quad (37)$$

or

$$\hat{S}_{ik}(\hat{z}) = \hat{z}_{ik}\hat{z}_{i,k+1} \quad (k = 1, \dots, K-1) \quad (38)$$

denotes the $K-1$ stabilizer operator, which is the origin of the ferromagnetic coupling between the spins in each logical group. The stabilizer operator $\hat{S}_{ik}(\hat{z})$ commutes with $\hat{H}^{phys}(\hat{z})$ and anti-commutes with the spin-flip errors for the physical spins involved in Eq. (37) or (38).

Note that, although this Hamiltonian is applicable to the communication application where the physical spins within a replica are assumed to be mutually independent, it is not necessarily applicable to QA because coupling among the spins within a replica is crucial in QA. To extend this Hamiltonian to describe QA, the two-body coupling has been heuristically introduced between the spins within each replica in some studies, that is,

$$\begin{aligned} \hat{H}^{two}(\hat{z}) &= \sum_{k=1}^K \left(\beta \sum_{\langle i,j \rangle}^N J_{ij} \hat{z}_{i,k} \hat{z}_{j,k} \right) \\ &= \beta \sum_{k=1}^K \sum_{\langle i,j \rangle}^N J_{ij} \hat{z}_{i,k} \hat{z}_{j,k}, \end{aligned} \quad (39)$$

into the physical Hamiltonian, and the use of

$$\begin{aligned} \hat{H}^{QAC}(\hat{z}) &= \hat{H}^{phys}(\hat{z}) + \hat{H}^{two}(\hat{z}) \\ &= \beta \hat{H}^{enc}(\hat{z}) + \gamma \hat{H}^{pen}(\hat{z}) \end{aligned} \quad (40)$$

was proposed for the Hamiltonian of the QAC, where $\langle i, j \rangle$ indicates that the sum runs over the coupled spins within the replica, and β and γ are positive weight parameters [6, 18–20, 24]. We refer to $\hat{H}^{QAC}(\hat{z})$ as the QAC Hamiltonian. The last equation indicates that $\hat{H}^{QAC}(\hat{z})$ comprises two components. The first is an encoded Hamiltonian

$$\hat{H}^{enc}(\hat{z}) = \sum_{k=1}^K \hat{H}^{logi}(\hat{Z}) \Big|_{\hat{Z}_i \mapsto \hat{z}_{i,k}}, \quad (41)$$

where

$$\hat{H}^{logi}(\hat{Z}) = \sum_{\langle i,j \rangle}^N J_{ij} \hat{Z}_i \hat{Z}_j + \sum_{i=1}^N h_i \hat{Z}_i, \quad (42)$$

and $\hat{Z} = \{\hat{Z}_i\}_{i=1, \dots, N}$ is the set of N logical spin operators. $\hat{H}^{logi}(\hat{Z})$ is the embedded Hamiltonian for N logical spins, which is our main interest. The second is the penalty Hamiltonian

$$\hat{H}^{pen}(\hat{z}) = \sum_{i=1}^N \sum_{k=1}^{K-1} \frac{1 - \hat{S}_{ik}(\hat{z})}{2}, \quad (43)$$

which commutes with $\hat{H}^{enc}(\hat{z})$ and is introduced to take advantage of the prior knowledge of $K-1$ sets of the parity constraints on the K physical spin variables \hat{z}_{ik} for

$k = 1, \dots, K$ in the Bayes inference. $\hat{H}^{pen}(\hat{z})$ enforces the alignment of the K physical spins in each logical group. The Hamiltonian $\hat{H}^{two}(\hat{z})$ introduces correlations between the physical spins in different logical groups, which are absent in the Hamiltonian $\hat{H}^{phys}(\hat{z})$ in the communication scenario. In the limit $\gamma \rightarrow 0$, $\hat{H}^{QAC}(\hat{z})$ approaches the Hamiltonian for K independent copies of the N spin system, each of which is described by the logical Hamiltonian $\hat{H}^{logi}(\hat{Z}) \Big|_{\hat{Z}_i \mapsto \hat{z}_{i,k}}$. Hence, we refer to a set of N physical spins specified by k as a replica. In contrast, in the limit $\beta \rightarrow 0$, $\hat{H}^{QAC}(\hat{z})$ approaches the Hamiltonian $\hat{H}^{pen}(\hat{z})$ that energetically penalizes the non-code state of the $[N, 1]$ repetition spin-flip code. In this case, it should be noted that if we select the weight-two stabilizer in Eq. (38), $\hat{H}^{QAC}(\hat{z})$ is formally identical to that in simulated QA (SQA) using the path-integral Monte Carlo method [43–46]. This implies that SQA may be re-investigated from the viewpoint of the classical error-correcting code. We can describe the quantum dynamics of QAC by combining the standard transverse-field driver Hamiltonian based on local Pauli- x operators

$$\hat{H}_1^{tr}(\hat{x}) = \kappa \sum_{i=1}^N \sum_{k=1}^K \hat{x}_{i,k} \quad (44)$$

with $\hat{H}^{QAC}(\hat{z})$ and introducing the temporal dependence for β , γ , and κ . Note that the logical Pauli operators for QAC are expressed as

$$\hat{Z}_{Li} = \hat{z}_{i,1} \text{ and } \hat{X}_{Li} = \prod_{k=1}^K \hat{x}_{i,k}. \quad (45)$$

We can select another transverse-field driver Hamiltonian based on the K -body logical Pauli- x operator [6, 37, 39, 40, 42, 47, 48]

$$\hat{H}_2^{tr}(\hat{x}) = \kappa \sum_{i=1}^N \hat{X}_{Li} \neq \hat{H}_1^{tr}(\hat{x}), \quad (46)$$

which requires K -body interactions and is difficult to implement practically using current technologies.

III. DECODING OF POST-READOUT SPIN STATE

The purpose of decoding is to infer the correct logical and physical target states \mathbf{Z} and \mathbf{z} , respectively, given the coupling \mathbf{J} (and local field \mathbf{h}). From the communication application viewpoint, we identify \mathbf{J} (and \mathbf{h}) as the readout associated with the physical state \mathbf{z} . If \mathbf{J} is corrupted by environmental noise, the target states are expected to be the state maximizing the posterior probability $P(\mathbf{Z}|\mathbf{J})$ or $P(\mathbf{z}|\mathbf{J})$ if the environmental noises in the spins are mutually weakly correlated [25, 49]. Then, the optimal estimators for \mathbf{Z} and \mathbf{z} are expressed as

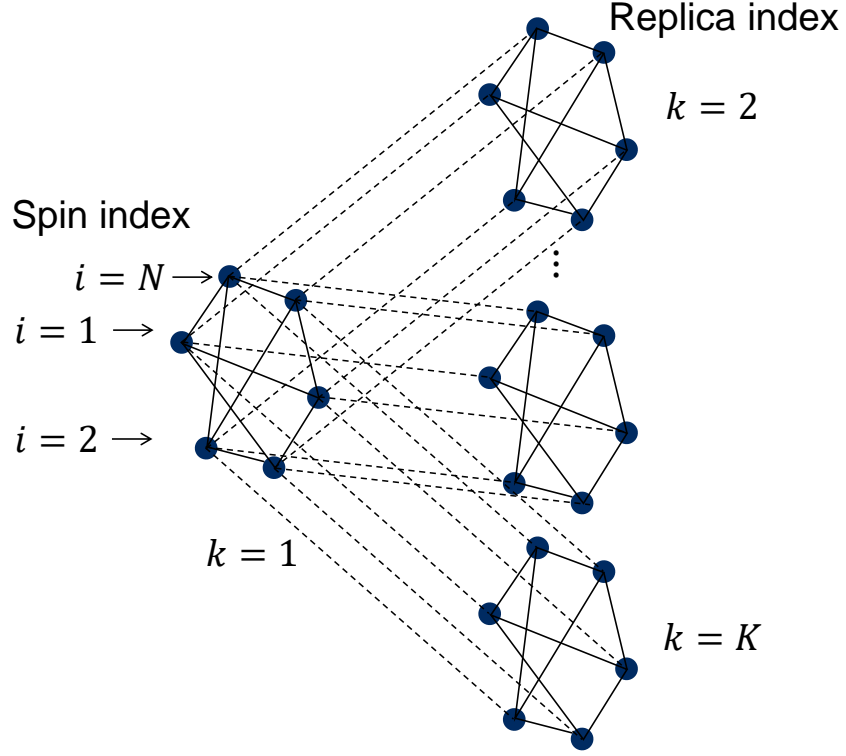


FIG. 3. Layout of physical spins in QAC when $\hat{S}_{ik}(\hat{z})$ is given by Eq. (37). The spins specified with the same index i are ferromagnetically coupled and constitute the logical group associated with the logical spin i . The index k specifies the replica to which the spin belongs. The solid lines indicate mutual spin couplings within a replica. The broken lines indicate ferromagnetic couplings.

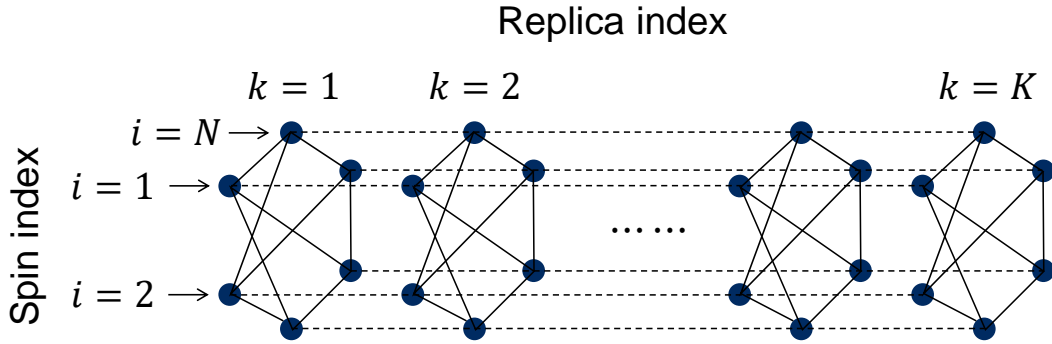


FIG. 4. Layout of physical spins in QAC with $\hat{S}_{ik}(\hat{z})$ given by Eq. (38). In this case, the ferromagnetic couplings in each logical group differ from those in Fig. 3.

$$\mathbf{Z}^* = \arg \max_{\mathbf{Z} \in \{\pm 1\}^K} P(\mathbf{Z}|\mathbf{J}) = \arg \max_{\mathbf{Z} \in \{\pm 1\}^K} L(\mathbf{Z}, \mathbf{J}) = \arg \min_{\mathbf{Z} \in \{\pm 1\}^K} H^{\text{logi}}(\mathbf{Z}) = \mathbf{Z}_g \quad (47)$$

in terms of the logical spins, or equivalently,

$$\mathbf{z}^* = \arg \max_{\mathbf{z} \in \{\pm 1\}^N} P(\mathbf{z}|\mathbf{J}) = \arg \max_{\mathbf{z} \in \{\pm 1\}^N} L(\mathbf{z}, \mathbf{J}) = \arg \min_{\mathbf{z} \in \{\pm 1\}^N} H^{\text{phys}}(\mathbf{z}) = \mathbf{z}_g \quad (48)$$

in terms of the physical spins, where \mathbf{Z}_g and \mathbf{z}_g are the ground states of the perturbed Hamiltonians $H^{logi}(\mathbf{Z})$ and $H^{phys}(\mathbf{z})$, respectively. It should be noted that the two formulations are equivalent if and only if the one-to-one correspondence between \mathbf{Z}_g and \mathbf{z}_g is preserved, that is, \mathbf{z}_g needs to be the code state. Therefore, Eq. (48) should be complemented with the parity constraints $S_i(\mathbf{z}_g) = +1$ ($i = 1, \dots, N - K$). To this end, one needs to select an appropriate set of weight parameters $\{\beta, \lambda\}$ in the physical Hamiltonian $H^{phys}(\mathbf{z})$, as discussed later. Equations (47) and (48) are called the maximum a posteriori (MAP) estimators. The target state \mathbf{z}_g should be a code state that is nearest to \mathbf{J} and minimizes the block-wise error probability p_B in the communication application. Similarly, in the optimization application, the target states are the logical ground state \mathbf{Z}_g and the associated physical code states $\mathbf{z}_g = \mathbf{Z}_g \otimes \mathbf{Z}_g$ given \mathbf{J} (and \mathbf{h}), which encode the combinatorial optimization problem to be solved. Therefore, they are common target states to be inferred from both viewpoints.

Nevertheless, it should be noted that if the readout \mathbf{J} is significantly perturbed, the target states may be one of many excited states that are neighboring states of the ground states of the perturbed Hamiltonian [49, 50]. In such a case, we can alternatively select the marginal posterior maximizer (MPM) estimators, i.e.,

$$\begin{aligned} \mathbf{Z}_i^* &= \arg \max_{Z_i \in \{\pm 1\}} P(Z_i | \mathbf{J}) = \text{sgn} \left[\sum_{Z_i = \pm 1} Z_i P(Z_i | \mathbf{J}) \right] \\ &= \text{sgn} \left[\langle Z_i \rangle_{P(\mathbf{Z} | \mathbf{J})} \right] \end{aligned} \quad (49)$$

in terms of the logical spins and

$$\begin{aligned} z_i^* &= \arg \max_{z_i \in \{\pm 1\}} P(z_i | \mathbf{J}) = \text{sgn} \left[\sum_{z_i = \pm 1} z_i P(z_i | \mathbf{J}) \right] \\ &= \text{sgn} \left[\langle z_i \rangle_{P(\mathbf{z} | \mathbf{J})} \right] \end{aligned} \quad (50)$$

in terms of the physical spins, where

$$P(Z_i | \mathbf{J}) = \sum_{\{Z_k: k \neq i\}} P(\mathbf{Z} | \mathbf{J}) \quad (51)$$

and

$$P(z_i | \mathbf{J}) = \sum_{\{z_k: k \neq i\}} P(\mathbf{z} | \mathbf{J}) \quad (52)$$

are the marginal posterior distributions. The angular brackets in Eqs. (49) and (50) denote the average over the thermal distributions $P(\mathbf{Z} | \mathbf{J}) = \exp(-H^{logi}(\mathbf{Z}))$ and $P(\mathbf{z} | \mathbf{J}) = \exp(-H^{phys}(\mathbf{z}))$, respectively, where the inverse temperature β_i has been absorbed in the perturbed Hamiltonians $H^{logi}(\mathbf{Z})$ and $H^{phys}(\mathbf{z})$. They may offer a better estimate of the target states given the prior information regarding the environmental noise through the parameter β_i . It is known that MPM

decoding is better than MAP decoding if we calculate the thermal average of the spin variables in Eqs. (49) and (50) using the perturbed Hamiltonian at the Nishimori temperature [49–51]. We can infer the optimal estimator \mathbf{Z}^* by reconstructing the sets of optimal estimators Z_i^* for $i = 1, \dots, K$ as well as \mathbf{z}^* by reconstructing z_i^* for $i = 1, \dots, N$. This is called maximal entropy decoding [50, 52].

In the following, we focus on the case where the target states are the logical ground states \mathbf{Z}_g and associated physical code state $\mathbf{z}_g = \mathbf{Z}_g \otimes \mathbf{Z}_g$. This is because our main objective is the development of an efficient solver for combinatorial optimization problems by taking advantage of nature-inspired approaches. It is assumed that we have a method that can statistically sample the neighboring states of the physical target state $\mathbf{r} \sim \mathbf{z}_g$, such as simulated annealing based on Monte Carlo simulation and QA. The readout state \mathbf{r} may be a non-code state. We address the decoding of the interim readout \mathbf{r} to infer the target state \mathbf{z}^* by taking advantage of the informative prior for parity constraints incorporated by the error-correcting codes. Let us consider the following scenario. Given \mathbf{J} and \mathbf{h} , we statistically sample the interim readout \mathbf{r} in the first stage. Successively, we decode \mathbf{r} with some deterministic algorithms in the second stage and attempt to improve it by taking advantage of the information involved in the syndrome that is derived from \mathbf{r} . If the inferred state \mathbf{z}^* is better than \mathbf{r} , we select \mathbf{z}^* as the estimate of \mathbf{z} . We can iterate this post-readout decoding until saturation, that is, no further improvement occurs. Therefore, our algorithm can be considered as a hybrid computation of earlier stochastic and later deterministic algorithms, as shown schematically in Fig. 5. If the stochastic algorithm is executed by a quantum computer including a quantum annealer, our algorithm is merely a hybrid quantum and classical computation. We studied how such decoding can be implemented from the classical viewpoint. We analyzed the similarities and differences between decoding for the PE scheme and QAC. For deterministic decoding in the second stage, we focus on one-step MVD, which is the simplest conventional decoding method for classical repetition codes. We compare the one-step MVD for QAC and that for the PE scheme. The one-step MVD relies on a priori probability (APP) decoding, which resembles MPM decoding. Its theoretical foundation was first described by Massey [26, 27], who considered a special set of syndromes called orthogonal parity checks and their correlation with errors. Massey's theory suggests that we should be careful to compare the correct set of readouts of the physical states in order to perform fair majority voting and derive the correct inference. Let us briefly review Massey's theory, called threshold decoding, using spin representation.

Let us consider the (n, k) linear block code C . Let the vectors $\mathbf{Z} = (Z_1, \dots, Z_k) \in \{\pm 1\}^k$ and $\mathbf{z} = (z_1, \dots, z_n) \in \{\pm 1\}^n$ denote the classical logical and

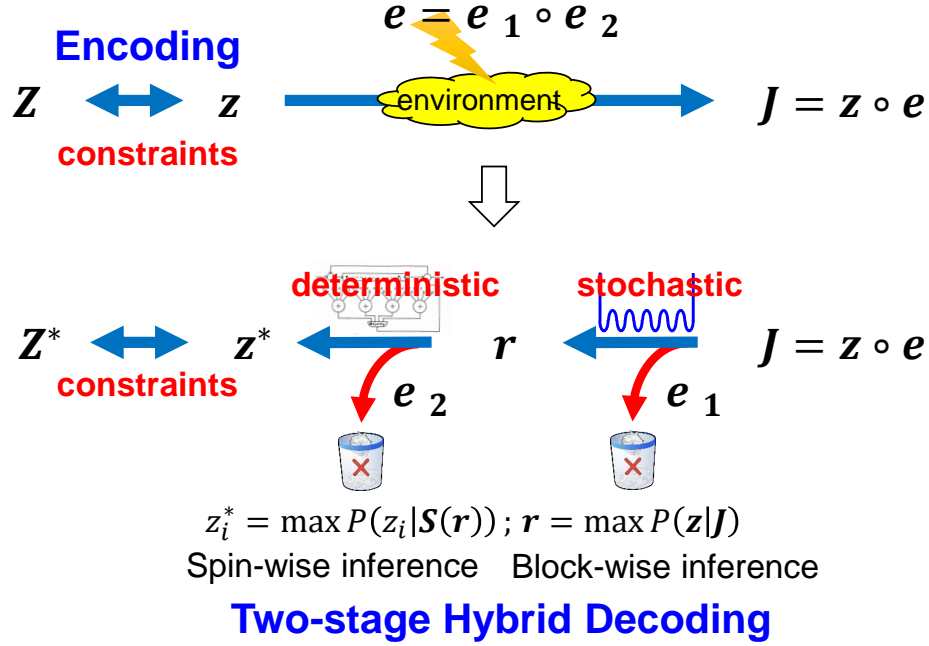


FIG. 5. Two-stage hybrid decoding scheme considered in this study. In the first stage, we decode the readout \mathbf{J} using a stochastic decoding method and obtain the interim readout \mathbf{r} . In the second stage, we decode the readout \mathbf{r} using a deterministic decoding method and obtain the optimal estimator \mathbf{z}^* . The deterministic decoding is the one-step MVD in this study. The errors in \mathbf{J} are entirely corrected in the sequence of the two decoding stages.

physical spin states, respectively. The logical state \mathbf{Z} is assumed to be encoded by the code C in the physical state \mathbf{z} according to Eq. (3). The physical state \mathbf{z} is assumed to be constrained by the $n - k$ parity check equations, as shown in Eq. (4). Suppose that we sample $\mathbf{r} = (r_1, \dots, r_n) \in \{\pm 1\}^n$ in the first stage, each element of which is hard-decided to bipolar values. The readout \mathbf{r} may be corrupted by noise and expressed using a set of random noise $\mathbf{e} = (e_1, \dots, e_n) \in \{\pm 1\}^n$ as an element-wise (Hadamard) product $\mathbf{r} = \mathbf{z}_g \circ \mathbf{e}$, that is, $e_i = (z_g)_i r_i$ ($i = 1, \dots, n$), where e_i is the error in the readout r_i . We consider the syndrome pattern $\mathcal{S}(\mathbf{r}) = (S_1(\mathbf{r}), \dots, S_{n-k}(\mathbf{r})) \in \{\pm 1\}^{n-k}$ associated with the parity check equations as $S_i(\mathbf{r}) = M_{k_1 \dots k_q}^i \prod_{l=1}^q r_{k_l} \in \{\pm 1\}$. The key point of one-step MVD is forming a special subset of J composite syndromes $\mathbf{A}_m = (A_{m1}, A_{m2}, \dots, A_{mJ}) \in \{\pm 1\}^J$ with $J \leq n - k$ from the product of the appropriately selected S_i values to check the error e_m of the m th physical spin ($m = 1, \dots, n$). This is defined as

$$A_{mi} = r_m \prod_{j \in C_i(m)} r_j = e_m \prod_{j \in C_i(m)} e_j, \quad (53)$$

where $C_i(m)$ is an $n_{mi} = |C_i(m)|$ tuple of the indices of \mathbf{r} comprising the syndrome A_{mi} . Note that the second equality in Eq. (53) holds because A_{mi} is a product of S_i and is itself a syndrome. In addition, because any code

word \mathbf{c} satisfies $\mathbf{c}\mathbf{H}^T = \mathbf{0}$,

$$z_m \left(\prod_{j \in C_i(m)} z_j \right) = +1 \quad (54)$$

holds for any code state \mathbf{z} . Thus, A_{mi} is a function of only e . \mathbf{A}_m has another notable property: every A_{mi} involves the noise component e_m , but no other noise component e_i ($i \neq m$) is involved in more than one syndrome in the set, i.e., every e_i ($i \neq m$) appears in only one of the sets $\{C_1(m), \dots, C_J(m)\}$. Such a subset \mathbf{A}_m of composite syndromes is said to be orthogonal on e_m . Massey showed that a set \mathbf{A}_m of syndromes orthogonal on e_m is a good APP estimator for e_m [26, 27].

Consider the posterior probability distribution $P(\mathbf{e} | \mathbf{A}_m)$, which describes the conditional probability that \mathbf{e} is the noise pattern when the syndrome \mathbf{A}_m orthogonal on e_m has been observed, and its marginals $P(e_m | \mathbf{A}_m) = \sum_{\mathbf{e} \neq e_m} P(\mathbf{e} | \mathbf{A}_m)$. We focus on e_m instead of σ_m because we can expect a nontrivial statistical correlation between e_m and \mathbf{A}_m , as A_{mi} is a function of only \mathbf{e} , as shown in Eq. (53). Once the Bayes optimal estimator e_m^* for e_m is obtained for $m = 1, \dots, n$, we can determine the optimal estimator z_m^* for z_m by $z_m^* = r_m e_m^*$. In the non-algebraic decoding scheme, Bayesian inference can be used to obtain the most probable error e_m of the m th physical state z_m , similar to MPM decoding. Then, the optimal estimator e_m^* is

expressed as

$$\begin{aligned} e_m^* &= \arg \max_{e_m = \pm 1} [P(e_m | \mathbf{A}_m)] = \operatorname{sgn} \left[\sum_{e_m = \pm 1} e_m P(e_m | \mathbf{A}_m) \right] \\ &= \operatorname{sgn} \left[\langle e_m \rangle_{P(e_m | \mathbf{A}_m)} \right], \end{aligned} \quad (55)$$

where the angular bracket in Eq. (55) indicates the average over the distribution $P(e_m | \mathbf{A}_m)$. Equation (55) can be interpreted as the decoding strategy, where e_m^* is determined by the majority vote of e_m associated with the statistically independent ensemble with the posterior distribution $P(e_m | \mathbf{A}_m)$. In general, the evaluation of such an average requires the computation of the summations of 2^{n-1} terms for determining the two-valued marginal posterior, which may require computational resources that scale exponentially with n . Otherwise, we need to use approximate methods, e.g., Monte Carlo sampling or a computationally more efficient probability propagation algorithm [25]. In contrast, if we can construct a syndrome \mathbf{A}_m orthogonal on e_m successfully from the syndrome \mathbf{S} and use a simplifying assumption, we can evaluate $\langle e_m \rangle_{P(e_m | \mathbf{A}_m)}$ cheaply using the knowledge of $P(e_m | \mathbf{A}_m)$.

Based on the orthogonality on e_m of \mathbf{A}_m and the assumption of spin-by-spin independence of the noise, any set of distinct states in the syndromes \mathbf{A}_m is disjoint. Then, because of the Bayes theorem and monotonicity of logarithmic functions, it follows that

$$e_m^* = \operatorname{sgn} \left[w_{m0} + \sum_{i=1}^J w_{mi} A_{mi} \right], \quad (56)$$

where

$$\begin{aligned} P(A_{mi} = -1 | e_m = +1) &= P(A_{mi} = +1 | e_m = -1) \\ &= p_i, \end{aligned} \quad (57)$$

$$\begin{aligned} P(A_{mi} = -1 | e_m = -1) &= P(A_{mi} = +1 | e_m = +1) \\ &= 1 - p_i, \end{aligned} \quad (58)$$

$w_{m0} = \log \frac{1-\xi_m}{\xi_m}$, $w_{mi} = \log \frac{1-p_i}{p_i}$, and $\xi_m = P(e_m = -1) = 1 - P(e_m = +1)$ for $i = 1, \dots, J$. Here, e_i is assumed to be a statistically random variable independent of i . In Eqs. (57) and (58), p_i is the probability of an odd number of "-1" among all e_j exclusive of e_m in the products that constitute A_{mi} , the i th syndrome orthogonal on e_m . It follows that

$$p_i = \frac{1}{2} \left[1 - \prod_{j \in B_i(m)} (1 - 2\xi_j) \right]. \quad (59)$$

It should be noted that if $\xi_i < \frac{1}{2}$ for any $i = 1, \dots, n$, it follows that $0 < w_{mi} \leq w_{m0}$ for $i = 1, \dots, J$. The positive value of w_{mi} implies that there should be a positive statistical correlation between A_{mi} and e_m , i.e.,

$1 - p_i > p_i$. Equation (56) indicates that the Bayes optimal estimator e_m^* for e_m can be evaluated from the syndrome \mathbf{A}_m orthogonal on e_m if we can calculate the weight w_{mi} from that of ξ_i for $i = 1, \dots, J$.

The key points for deriving Eqs. (57)–(59) are as follows. The syndrome $\mathbf{A}_m = (A_{m1}, A_{m2}, \dots, A_{mJ})$ is selected in such a manner that all errors e_i ($m = 1, \dots, n$) are involved in at least one of the elements of \mathbf{A}_m but the errors e_m and $e_{i \neq m}$ are asymmetrical; e_m is involved in all elements of \mathbf{A}_m , whereas the other errors $e_{i \neq m}$ are involved in only one of the elements of \mathbf{A}_m . Comprehensive examples are presented later. Of course, $\mathbf{A}_m = +1$ if and only if $\mathbf{e} = +1$, where $+1$ is a constant vector with the element as $+1$. The right-hand side of Eq. (56) can be considered to be a function of the syndromes \mathbf{S} , as \mathbf{A}_m is a function of \mathbf{S} . That is, we can infer the error pattern for all spins by analyzing the syndrome pattern, which is very reasonable. It should be noted that a choice in Eq. (53) might be fair if the set $C_i(m)$ treats all readouts r_i of the spin variables symmetrically and the majority voting defined by Eq. (55) uses all syndromes [25]. The fair choice of the set $C_i(m)$ might be crucial for realizing efficient one-step MVD.

Equation (56) can be further simplified by modifying \mathbf{A}_m in the following manner [26, 29, 53]. First, we introduce $\mathbf{B}_m = (B_{m0}, B_{m1}, \dots, B_{mJ}) \in \{\pm 1\}^{J+1}$, where $B_{m0} = r_m$ and

$$\begin{aligned} B_{mi} &= r_m A_{mi} = \prod_{j \in C_i(m)} r_j \\ &= z_m \prod_{j \in C_i(m)} e_j \quad (m = 1, \dots, k; i = 1, \dots, J) \end{aligned} \quad (60)$$

We state that the \mathbf{B}_m estimators are orthogonal on z_m . Evidently, B_{mi} satisfies $z_m B_{mi} = z_m r_m A_{mi} = e_m A_{mi}$ for $m = 1, \dots, k$ and $i = 1, \dots, J$. Similar to Eq. (56), the Bayes optimal estimator z_m^* for z_m is expressed as

$$\begin{aligned} z_m^* &= \arg \max_{z_m = \pm 1} [P(z_m | \mathbf{B}_m)] = \operatorname{sgn} \left[\sum_{z_m = \pm 1} z_m P(z_m | \mathbf{B}_m) \right] \\ &= \operatorname{sgn} \left[\langle z_m \rangle_{P(z_m | \mathbf{B}_m)} \right]. \end{aligned} \quad (61)$$

If we assume spin-by-spin independence of the environmental noise, it follows that

$$z_m^* = \operatorname{sgn} \left[\sum_{i=0}^J w_{mi} B_{mi} \right], \quad (62)$$

where we have assumed an ignorance prior for the physical spin state \mathbf{z} , i.e., $P(z_m = +1) = P(z_m = -1)$. The equality $z_m B_{mi} = e_m A_{mi}$ implies $P(z_m B_{mi} = \pm 1 | z_m) = P(e_m A_{mi} = \pm 1 | e_m)$ for $m = 1, \dots, k$; that is, $P(B_{mi} = \pm V | z_m = V) = P(A_{mi} = \pm V | e_m = V)$, where $V \in \{\pm 1\}$. It is easy to confirm that w_{mi} in Eqs. (56) and (62) are the same,

because for $m = 1, \dots, k$,

$$\begin{aligned} P(B_{mi} = -1|z_m = +1) &= P(B_{mi} = +1|z_m = -1) \\ &= \begin{cases} \xi_m & \text{for } i = 0 \\ p_i & \text{for } i = 1, \dots, J \end{cases} \end{aligned} \quad (63)$$

and

$$\begin{aligned} P(B_{mi} = -1|z_m = -1) &= P(B_{mi} = +1|z_m = +1) \\ &= \begin{cases} 1 - \xi_m & \text{for } i = 0 \\ 1 - p_i & \text{for } i = 1, \dots, J \end{cases} \end{aligned} \quad (64)$$

hold. Equation (62) indicates that z_m^* is determined by the one-step majority vote of the $J + 1$ elements B_{mi} ($i = 0, \dots, J$) in the \mathbf{B}_m weighted by w_{mi} , that is,

$$z_m^* = \text{maj}(w_{m0}B_{m0}, w_{m1}B_{m1}, \dots, w_{mJ}B_{mJ}), \quad (65)$$

where we have used the following definition for the majority function of bipolar variables $y_0, y_1, \dots, y_J \in \{\pm 1\}^{J+1}$ [54]:

$$\text{maj}(y_0, y_1, \dots, y_J) = \begin{cases} +1, & \text{if } \sum_{i=0}^J y_i > 0 \\ -1, & \text{if } \sum_{i=0}^J y_i < 0 \\ \text{undefined} & \text{otherwise} \end{cases} \quad (66)$$

The sign of the weight w_{mi} describes the positive ($w_{mi} > 0$) or negative ($w_{mi} < 0$) statistical correlation that is expected between the orthogonal estimators B_{mi} (A_{mi}) and z_m (e_m) in Eq. (62) (Eq.(56)) on which Bayes inference relies. The magnitude of the weight $|w_{mi}|$ describes the measure of reliability of the estimator B_{mi} (A_{mi}), which is determined by the error probability ξ_j for the readout r_j that constitutes the estimator B_{mi} (A_{mi}). When $|w_{mi}|$ is larger, the estimator B_{mi} (A_{mi}) is more reliable. The optimal estimate for the remaining spin states z_i^* ($i \neq m$) can be performed by sifting the index of the spin cyclically and repeating the one-step MVD in the same manner. This is because if it is possible to form a set of J syndromes orthogonal on e_m , it is possible to form a set of J syndromes orthogonal on any spin e_i ($i \neq m$) if C is a cyclic code. Correct decoding of z_m is guaranteed if there are $\lfloor \frac{J}{2} \rfloor$ or fewer errors in the error of the readout \mathbf{r} .

Note that the calculation of the weight w_{mi} becomes computationally expensive when $n_{mi} = |C_i(m)| \gg 1$, even if all ξ_j ($j = 1, \dots, n$) are known, because w_{mi} is a complicated nonlinear function of ξ_j for the received state r_j , which is a member of $C_i(m)$. Therefore, it is often necessary to introduce some approximations in the calculation of Eq. (59), which is beyond the scope of our study and can be referenced in [30, 53]. Here, we note that the most simplified approximation assumes that $w_{mi} = \text{const.}$ for $i = 0, \dots, J$, which amounts to neglecting the imbalance in the reliability of the

estimators owing to imbalance in the error probabilities ξ_i of the readout r_i . In this simplified approximation, z_m^* is determined by the one-step majority vote of the $J + 1$ elements B_{mi} in \mathbf{B}_m ; that is,

$$z_m^* = \text{maj}(B_{m0}, B_{m1}, \dots, B_{mJ}). \quad (67)$$

A. Classical repetition code

We discuss two illustrative examples, namely the classical repetition code and PE scheme, to understand the one-step MVD comprehensively. Let us first consider the $(n, k) = (N, 1)$ classical repetition code, which encodes a logical spin variable $Z = z_1$ into N physical spin states $\mathbf{z} = (z_1, \dots, z_N) \in \{\pm 1\}^N$. The minimum code distance d_{min} can be increased by repeating the logical information N times; thus, $d_{min} = N$, which enables the correction of errors in the N physical spin states. In principle, the repetition code should be capable of correcting up to $t_{RP} = \lfloor \frac{d_{min}-1}{2} \rfloor$ spin-flip errors. The orthogonal syndrome appropriate for one-step MVD is expressed as $A_i = r_1 r_{i+1} = e_1 e_{i+1}$ for $i = 1, \dots, N-1$. Therefore, we can use the syndrome \mathbf{S} in Eq. (37) as the estimator for the error e_1 ; that is, $\mathbf{A} = \mathbf{S} = (S_1, S_2, \dots, S_{N-1}) \in \{\pm 1\}^{N-1}$. Thus, the repetition code is a self-orthogonal code [29, 30]. If we apply the second type of one-step MVD in Eq. (62), the set of $J + 1 = N$ estimators \mathbf{B} orthogonal on z_1 associated with the set of $J = N - 1$ syndromes \mathbf{A} orthogonal on e_1 is identified as $\mathbf{B} = \mathbf{r} = (r_1, \dots, r_N) \in \{\pm 1\}^N$. The Bayes-optimal estimator Z^* for Z is given by the one-step majority vote of the set of readouts \mathbf{r} , that is,

$$Z^* = z_1^* = \text{maj}(r_1, \dots, r_N), \quad (68)$$

if we neglect the imbalance for the reliability of the estimator r_i . Equation (68) implies that the one-step MVD can correct up to $\lfloor \frac{N-1}{2} \rfloor$ errors. Because a set \mathbf{A} of $J = d_{min} - 1$ syndromes orthogonal on error e_1 of the logical spin state can be formed, one-step MVD can achieve the error-correcting capability t_{RP} of the repetition code. Therefore, the repetition code can be completely orthogonalized in one step [26–30].

B. QAC

The repetition spin-flip code is used for the stabilizer subspace codes [55] in QAC to suppress the local spin-flip errors in QA [6, 17–24]. We focus on the classical model of N logical spins described by the logical Hamiltonian $\hat{H}^{logi}(\hat{\mathbf{Z}})$ (Eq. (42)), which are embedded into the $N \times K$ physical spin system described by the QAC Hamiltonian $\hat{H}^{QAC}(\hat{\mathbf{z}})$ (Eq. (40)). To this end, the quantum mechanical operators \hat{z}_i are replaced with the classical spin variables $z_i \in \{\pm 1\}$ and their associated readouts are considered to be $r_i \in \{\pm 1\}$. To describe the

state of the physical spins and its readout, we introduce the $N \times K$ matrices $\mathbf{z} \in \{\pm 1\}^{N \times K}$ and $\mathbf{r} \in \{\pm 1\}^{N \times K}$ ($\{\pm 1\}^{N \times K}$ denotes an $N \times K$ matrix of bipolar variables), whose elements z_{ij} and r_{ij} describe the state and its readout, respectively, of the physical spin specified by the index i ($= 1, \dots, N$) in the replica j ($= 1, \dots, K$).

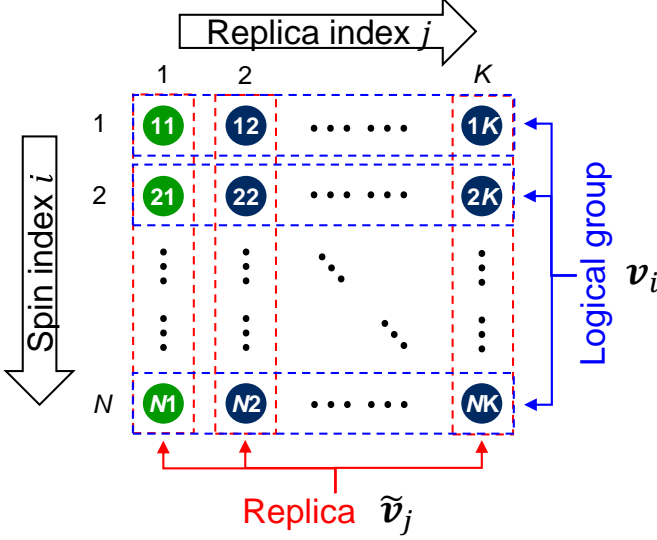


FIG. 6. Structure of the matrices $\mathbf{v} = \mathbf{z}$ or \mathbf{r} . The green circles are the elements corresponding directly to the logical spins.

To simplify the notation, we call \mathbf{z} and \mathbf{r} the physical state and readout, respectively. As shown in Fig. 6, each column of $\mathbf{v} = \mathbf{z}$ ($\mathbf{v} = \mathbf{r}$) describes the states (readouts) of N physical spins in each replica, whereas each row describes the states (readouts) of K physical spins in each logical group associated with the logical spin [6]. To simplify the notation, let $\mathbf{v}_i = (v_{i1}, \dots, v_{iK})$ denote the i th row vector of \mathbf{v} and let $\tilde{\mathbf{v}}_j = (v_{1j}, \dots, v_{Nj})^T$ denote the j th column vector of \mathbf{v} so that $\mathbf{v} = (\tilde{\mathbf{v}}_1, \dots, \tilde{\mathbf{v}}_K) = (\mathbf{v}_1, \dots, \mathbf{v}_N)^T$, where $\mathbf{v} = \mathbf{z}$ or \mathbf{r} . The vectors \mathbf{z}_i and $\tilde{\mathbf{z}}_j$ describe the state of the i th logical group associated with the i th logical spin and state of the j th replica, respectively. The spins in every replica share the intra-replica couplings J_{ij} that are defined in the logical Hamiltonian $H^{\text{logi}}(\mathbf{Z})$. Each logical spin variable Z_i is encoded by the classical $[K, 1]$ repetition code and constitutes the logical group \mathbf{z}_i ($i = 1, \dots, N$), each of which consists of K physical spins. We impose the parity constraints $z_{i,1}z_{i,j+1} = +1$ ($j = 1, \dots, K-1$) for the physical spin variables in each logical group i independently. Because N replicas share the same intra-replica couplings, we may expect that every weight w_{ij} of the estimator r_{ij} ($j = 1, \dots, K$) for the one-step MVD is independent of j based on symmetry consideration. Then, we can identify

$$A_{ij} = r_{i1}r_{ij+1} = e_{i1}e_{ij+1} \quad (j = 1, \dots, K-1) \quad (69)$$

for $K-1$ syndromes orthogonal on the error e_{i1} for

$i = 1, \dots, N$. Evidently, A_{ij} satisfies the requirements for orthogonal syndromes, as it involves a single common element r_{i1} and the other elements r_{ij+1} ($j = 1, \dots, K-1$) that appear only once in the $K-1$ element A_{ij} . Then, we can further identify $B_{i1} = r_{i1}$ and

$$B_{ij+1} = r_{i1}A_{ij} = r_{ij+1} = z_{i1}e_{ij+1} \quad (j = 1, \dots, K-1) \quad (70)$$

for K estimators that are orthogonal on every physical spin variable z_{i1} for $i = 1, \dots, N$. Thus, we obtain the Bayes-optimal estimator for the i th logical spin variable $Z_i = z_{i1}$ from the readouts \mathbf{r} as follows:

$$Z_i^* = z_{i1}^* = \text{maj}(B_{i1}, \dots, B_{iK}) = \text{sgn}[\langle \mathbf{r} \rangle_i], \quad (71)$$

$$\langle \mathbf{r} \rangle_i = \langle \mathbf{r}_i \rangle = \frac{1}{K} \sum_{j=1}^K r_{ij}, \quad (72)$$

where $\mathbf{B}_i = (B_{i1}, \dots, B_{iK}) = \mathbf{r}_i \in \{\pm 1\}^K$ corresponds to the orthogonal estimators for Z_i and the angular brackets $\langle \dots \rangle_i$ denote the average of the matrix elements in the i th row. Equations (71) and (72) indicate that the most probable value of the logical spin variable Z_i^* is determined by the average orientation of the readouts \mathbf{r}_i for the K physical spins in the associated logical group i . Thus, we can infer the most probable state \mathbf{Z}^* for N logical spins from the sign of the averaged readouts $\langle \mathbf{r} \rangle_i$ for $i = 1, \dots, N$.

Although this result appears rather trivial, it may nevertheless be interesting to compare it with the finite temperature decoding of the Sourlas code [49–51]. Consider the limit $\gamma \rightarrow 0$ for the QAC Hamiltonian $H^{\text{QAC}}(\mathbf{z})$. Then, the penalty Hamiltonian $H^{\text{pen}}(\mathbf{z})$, which forces the spins in each logical group i to be aligned for \mathbf{z} to become the code state, is absent. Thus, the K replicas run independently in parallel in $\gamma \rightarrow 0$. The same results should be applicable if a single replica runs K times according to the logical Hamiltonian and if the average orientation of every readout of the logical spin variables is evaluated, which is equivalent to finite temperature decoding. This implies that if the energetic penalty is sufficiently weak, thermal excitation might be beneficial for QAC when it is combined with the post-readout classical decoding. This aspect is discussed later in the paper.

Let us compare the following three post-readout classical decoding strategies for the $N \times K$ physical spins to obtain the ground state \mathbf{Z}_g of the logical Hamiltonian $H^{\text{logi}}(\mathbf{Z})$ (hereinafter referred to as the logical ground state) embedded in $H^{\text{QAC}}(\mathbf{z})$. (a) MAP decoding attempts to minimize $H^{\text{QAC}}(\mathbf{z})$ and simply reports its readout \mathbf{r} . This strategy is also called the energy minimization strategy [6]. (b) Best replica (BR) decoding after MAP decoding reports the readout $(\tilde{\mathbf{r}}_{j^*})^T$ (the transpose of column j^* of \mathbf{r}) with the smallest logical energy, i.e., $j^* = \arg \min_j H^{\text{logi}}(\tilde{\mathbf{r}}_j)$, where \mathbf{r} is the

readout of the MAP decoding. (c) One-step MVD after MAP decoding reports \mathbf{Z}^* obtained by one-step MVD $Z_i^* = \text{sgn}[\langle \mathbf{r} \rangle_i]$ for $i = 1, \dots, N$ from the readout \mathbf{r} of the MAP decoding. Note that $\langle \mathbf{r} \rangle_i$ can be calculated easily by averaging the i th row of the readout matrix \mathbf{r} . We first focus on strategies (a) and (b). Suppose that the readout \mathbf{r}_a of the (a) MAP decoding and (b) BR decoding on the readout \mathbf{r}_b of the MAP decoding successfully infers the target state $\mathbf{Z}^* = \mathbf{Z}_g$. Then, all columns of \mathbf{r}_a , i.e., $(\tilde{\mathbf{r}}_a)_j$ for $j = 1, \dots, N$, should agree with $(\mathbf{Z}_g)^T$ up to a global spin flip in strategy (a), as MAP decoding infers the most probable state for the physical ground state \mathbf{z}_g of $H^{QAC}(\mathbf{z})$, whereas it is sufficient for a column of \mathbf{r}_b , i.e., $(\tilde{\mathbf{r}}_b)_j$ for at least one j , to agree with $(\mathbf{Z}_g)^T$ up to a global spin flip in strategy (b). This suggests that strategy (b) can sample the logical ground state \mathbf{Z}_g more efficiently than strategy (a). For example, consider the limit $\gamma \rightarrow 0$ for simplicity, where the replicas are statistically independent. Then, it is reasonable to assume that every replica succeeds with the same probability p for sampling the logical ground state \mathbf{Z}_g . This implies that the probability for successfully sampling the target state \mathbf{Z}_g is $P_a = p^K$ for strategy (a), whereas the probability that the best of the K replicas will succeed is $P_b = 1 - (1 - p)^K > p$ for $K \geq 2$ for strategy (b). It follows that $P_A < p < P_B$ for $0 < p < 1$ and $P_A \ll p \ll P_B$ if $K \gg 2$. Therefore, strategy (b) will significantly improve the performance compared with the improvement when using strategy (a) for the same problem instance, at least in the limit $\gamma \rightarrow 0$.

Next, we compare strategy (c) one-step MVD after MAP decoding and strategy (a) MAP decoding. Suppose that one-step MVD on the readout \mathbf{r}_c of the MAP decoding successfully infers the logical ground state as the most probable state $\mathbf{Z}^* = \mathbf{Z}_g$. None of the columns of \mathbf{r}_c , i.e., $(\tilde{\mathbf{r}}_c)_j$, may agree with $(\mathbf{Z}_g)^T$ even if the logical ground state \mathbf{Z}_g is inferred successfully in strategy (c). This is possibly because one-step MVD can infer \mathbf{Z}_g if at least half of the elements in every readout \mathbf{r}_i associated with logical group i (every row of \mathbf{r}) are correct. Furthermore, QAC has a peculiar property that $H^{QAC}(\mathbf{z})$, $H^{enc}(\mathbf{z})$, and $H^{pen}(\mathbf{z})$ share the same physical ground state \mathbf{z}_g . This implies that the ground state of $H^{QAC}(\mathbf{z}) = \beta H^{enc}(\mathbf{z}) + \gamma H^{pen}(\mathbf{z})$ is independent of β and γ . Then, the majority of the erroneous but correctable states that contribute to the readout \mathbf{r}_c should be the excited states of $H^{QAC}(\mathbf{z})$, $H^{enc}(\mathbf{z})$, and $H^{pen}(\mathbf{z})$ with a small Hamming distance from the physical ground state \mathbf{z}_g . Thus, they should be distributed in the low-energy portion of the energy spectrum of $H^{QAC}(\mathbf{z})$, which should have a density of states that is much higher than that of the ground state \mathbf{z}_g . QAC can sample such excited states efficiently through sampling based on the Hamiltonian $H^{QAC}(\mathbf{z})$ at finite temperature (by local cooling [56, 57]) even in the limit $\gamma \rightarrow 0$, where the penalty Hamiltonian $H^{pen}(\mathbf{z})$ is absent. Thus, QAC may acquire great

benefit from the post-readout classical decoding even if $\gamma = 0$. This is similar to the finite temperature decoding of the Sourlas code, even though the target states differ. This discussion suggests that even though the energetic penalty is sufficiently weak, QAC may have better performance by applying one-step MVD of the readout after sampling at a finite temperature.

Our discussion also suggests that thermal excitation might be beneficial for QAC even if $\gamma > 0$ when it is combined with the post-readout classical decoding. This is evident from the discussion that, given two elements $H^{enc}(\mathbf{z})$ and $H^{pen}(\mathbf{z})$, the optimal values for the hyperparameter set $\{\beta, \gamma\}$ may depend on the post-readout decoding strategy. Recall that $H^{pen}(\mathbf{z})$ reflects the prior knowledge on the parity constraints on the physical spin variables. Suppose $\gamma > 0$ in the QAC Hamiltonian $H^{pen}(\mathbf{z})$ enforces K physical spins in every logical group to align by energetically penalizing the misalignment with their ferromagnetic interactions. The code states that satisfy all parity constraints are the degenerate ground states of $H^{pen}(\mathbf{z})$. If we consider the fact that the physical ground state \mathbf{z}_g of $H^{QAC}(\mathbf{z})$ is the common ground state of $H^{enc}(\mathbf{z})$ and $H^{pen}(\mathbf{z})$, it may be reasonable to balance two contributions for the energy gap in $H^{QAC}(\mathbf{z})$, i.e., $\beta \Delta H^{enc} \sim \gamma \Delta H^{pen} = \gamma$, to sample the common ground state efficiently, where ΔH^x is the energy gap between the first excited and ground states of H^x . Note that $\Delta H^{pen} = +1$. However, this might be reasonable only for strategy (a), where the desired readout \mathbf{r}_a is the physical ground state \mathbf{z}_g , but not for strategies (b) and (c), where the desired readouts \mathbf{r}_b and \mathbf{r}_c are very different from \mathbf{r}_a . In particular, in strategy (c), the desired readout \mathbf{r}_c is one of a majority of correctable erroneous states in which at least half of K physical spins in every logical group $(\mathbf{r}_c)_i$ are aligned correctly. Because such states are non-code states, redistributing the energy spectrum of $H^{QAC}(\mathbf{z})$ is preferable by controlling γ so that $\gamma < \beta \Delta H^{enc}$ to increase the sampling efficiency for the desired \mathbf{r}^c . We also note that a finite energy gap remains in $\beta \Delta H^{enc}$, even if $\frac{\gamma}{\beta}$ approaches zero. This residual gap $\beta \Delta H^{enc}$ might be the reason that thermal excitation is beneficial even if $\gamma \rightarrow 0$ for QAC when it is combined with post-readout classical decoding. This situation is in contrast with the PE scheme, where the energy gap closes as $\frac{\gamma}{\beta}$ becomes smaller, as considered later. It is important to note that this consideration would be justified if the population of the sampling results is distributed with a finite width so that the population of the relevant excited states has a finite probability. This conclusion holds true regardless of whether the final state reaches thermal equilibrium and the underlying dynamics approach the final state [58].

Some of the above suggestions are actually observed in the results of the QAC experiments in the literature. For example, in [19], Pudenz et al. demonstrated QAC using a programmable annealing processor. They used $K = 4$ replicated systems composed of a chain of N logical spins

that were anti-ferromagnetically coupled, and ran the annealing processor to sample the logical ground state. They claimed that a substantial improvement in the performance of the processors was observed compared with the result in the absence of error correction in the QAC. They attributed this improvement to the population of erroneous but correctable excited states of the QAC Hamiltonian, although they did not specify the origin of this population. It may be attributed to thermal excitation during the course of annealing. Because the annealing processor is a real-world machine, it is coupled to the thermal environment. Moreover, the user-specified parameters have finite strength and are controllable with finite speed. In fact, the D-Wave annealer is likely to sample the statistical ensemble of the readouts close to the thermal state, even though the spin dynamics during the annealing are not necessary classical and its temperature does not necessarily agree with (is higher than) the operating temperature of the device [52, 58–60]. The results of Ref. [19] suggest that post-readout classical decoding can improve the success probability for sampling the logical ground state by decoding the erroneous but correctable excited states of the QAC Hamiltonian. Furthermore, they presented an interesting result in their experiment: the optimal value of the penalty strength γ differs between our decoding strategies (b) and (c). For example, the sampling results for the two strategies are compared in Fig. 5 of Ref. [19]. In this figure, the success probability for sampling the logical ground state is plotted as a function of the anti-ferromagnetic chain length and penalty strength γ (penalty scale β in their definition) for three values of the strength β (problem scale α in their definition). Their results suggested that the optimal γ is significantly smaller for strategy (c) one-step MVD than strategy (b) BR decoding, which is consistent with our consideration. In addition, the success probability is relatively large for strategy (c) even though $\gamma \sim 0$, whereas it is very small for strategy (b), which is expected from the finite temperature decoding.

C. Parity encoding

Annealing is a heuristic optimization method, in which the solution is statistically inferred from an ensemble of many samples. Such samples can be obtained either through repeated runs using a single copy or through parallel runs using many copies. QAC can be interpreted as a system for statistically inferring the optimal solution through parallel runs of many copies based on the classical repetition codes. The solution can be obtained, for example, by selecting the best of the sampled readouts (strategy (b)) or by majority voting of the sampled readouts (strategy (c)). Now, let us consider the PE scheme. Although its interpretation is more subtle than that of QAC, the comparison between the PE scheme and QAC helps us to understand the error-correcting

capability of the PE scheme.

Consider the logical and encoded physical Hamiltonians $H^{\text{logi}}(\mathbf{Z})$ and $H^{\text{phys}}(\mathbf{z})$, given by Eqs. (23) and (20), respectively. We assume that the K -dimensional vector $\mathbf{Z} = (Z_1, \dots, Z_N)^T \in \{\pm 1\}^K$ describes the state of K logical spins. Then, let us consider a symmetric $K \times K$ bipolar matrix $\mathbf{z} = \mathbf{Z} \otimes \mathbf{Z} \in \{\pm 1\}^{K \times K}$, that is, $z_{ij} = Z_i Z_j$ ($1 \leq i, j \leq K$), which describes the physical spins in the code states and satisfies the parity-check equations $S_{ij}(\mathbf{z}) = z_{ij} z_{i+1, j+1} z_{i+1, j} z_{i, j+1} = +1$ for $1 \leq i < j \leq K-1$. Note that only $K-1$ physical variables are logically independent because we can determine \mathbf{Z} only up to the global spin flip. The matrix \mathbf{z} contains $N = \frac{K(K-1)}{2}$ independent variables. Therefore, a set of physical spin variables in \mathbf{z} constitutes the $\left(\frac{K(K-1)}{2}, K-1\right)$ block code. The matrix \mathbf{z} evolves according to the Hamiltonian $H^{\text{phys}}(\mathbf{z})$. We consider the general symmetric $K \times K$ bipolar matrix $\mathbf{r} \in \{\pm 1\}^{K \times K}$ with unit diagonal elements $r_{ii} = 1$ ($i = 1, \dots, N$) to describe the readout of the physical spin state. The readout \mathbf{r} may be the non-code state, i.e., $S_{i,j}(\mathbf{r}) = r_{ij} r_{i+1, j+1} r_{i+1, j} r_{i, j+1} \neq +1$ for some $1 \leq i < j \leq K$. In contrast, in QAC, the matrix $\mathbf{z}' \in \{\pm 1\}^{N \times K}$ describes the physical spins that evolve according to the Hamiltonian H^{QAC} . The matrices \mathbf{z} in the PE scheme and \mathbf{z}' in QAC differ in two manners. First, \mathbf{z} is a symmetric square matrix with unit diagonal elements, whereas \mathbf{z}' is not. Second, the row and column of \mathbf{z}' have direct physical interpretations, that is, they correspond to the physical spin variables in the same logical group and those in the same replica, respectively; however, the row and column of \mathbf{z} have no such direct physical interpretation.

At present, the error-correcting capability of the PE scheme has not been clarified specifically in terms of optimization application, although it was analyzed from the perspective of communication application based on the analogy of the LDPC code [25]. We note that these two viewpoints need to be distinguished, as explained previously. We consider the PE scheme from the viewpoint of optimization application. We show that physical noise is potentially useful in inferring the logical ground state \mathbf{Z}_g , not only for the QAC but also for the PE scheme below.

Now, let us consider the one-step MVD for the PE scheme. Here, we consider $K-2$ weight-three syndromes orthogonal on every error e_{ij} ,

$$A_{ijk}(\mathbf{r}) = r_{ij} r_{jk} r_{ki} = e_{ij} e_{jk} e_{ki} \in \{\pm 1\} \\ (\{i, j, k\}_c = 1, \dots, K), \quad (73)$$

as suggested by Pastawski and Preskill [25], where $\{i, j, k\}_c$ denotes one of $\binom{K}{3}$ combinations. Evidently, A_{ijk} satisfies the requirements for the orthogonal syndrome, as it involves the common element e_{ij}

and the other element $e_{jk}e_{ki}$ that appears only once in the $K - 2$ elements of A_{ijk} for every $i < j$. We can easily confirm that A_{ijk} can be represented as a product of weight-four syndromes $S_{ij}(\mathbf{r}) = r_{ij}r_{i+1}r_{i+1}r_{j+1}$, that is, a product of the readouts of the four physical spins associated with the plaquettes in the PE spin network [36], where r_{jj} is fixed at +1 by construction. For example, one can observe that $A_{247} = S_{24}S_{25}S_{26}S_{34}S_{35}S_{36}$ (see Fig. 2).

We can also identify $K - 1$ weight-two estimators orthogonal on z_{ij} :

$$B_{ijk}(\mathbf{r}) = r_{ij}A_{ijk}(\mathbf{r}) = r_{jk}r_{ki} = z_{ij}e_{jk}e_{ki} \in \{\pm 1\} \\ (\{i, j, k\}_c = 1, \dots, K). \quad (74)$$

It should be noted that $B_{iji} = B_{ijj} = r_{ij}$, which should be a member of the $K - 1$ elements of these syndromes. Then, if we simply apply the one-step MVD, it follows that

$$z_{ij}^* = \text{maj}(B_{ij1}, \dots, B_{ijK}) = \text{sgn}[\langle \mathbf{B}_{ij} \rangle], \quad (75)$$

where $\mathbf{B}_{ij} = (B_{ij1}, \dots, B_{ijK}) \in \{\pm 1\}^{K-1}$ corresponds to the estimators orthogonal on z_{ij} , and

$$\langle \mathbf{B}_{ij} \rangle = \sum_{k=1}^K r_{jk}r_{ki} - r_{ij} = (\mathbf{r}(\mathbf{r} - \mathbf{I}))_{ij}, \quad (76)$$

where \mathbf{I} is a K -dimensional identity matrix. Furthermore, if $K \gg 1$, Eq. (76) can be approximated to

$$\langle \mathbf{B}_{ij} \rangle \sim \sum_{k=1}^K r_{jk}r_{ki} = (\mathbf{r}^2)_{ij}. \quad (77)$$

Comparisons of Eqs. (71), (72), and (75)–(77) reveal a notable difference. Equation (71) indicates that although the Bayes optimal estimate of the logical spin variable $Z_i = z_{i1}$ is determined by the average of the readouts \mathbf{r}_i for the K physical spins in the associated logical group i in QAC, that of the physical spin variable z_{ij} is determined by the nonlocal correlations of the readouts for two physical spin variables in the PE scheme.

These correlations are according to prior knowledge on the parity constraints. However, to use this prior knowledge for majority voting, we need to be careful regarding its fair use. It should be remembered that our formula for one-step MVD in Eq. (62) has a theoretical background based on threshold decoding, where the fair use of the prior knowledge on the parity constraints is considered. In contrast, the previously reported one-step MVD has no theoretical background and uses a majority vote over different subsets of the products of physical spin variables that describe the spanning trees defined on the logical spins [9, 40], but not the orthogonal syndromes, for decoding. This spanning tree method does not consider the fair use of the prior knowledge and cannot be justified definitely; thus, its inference would

be unreliable as well as inefficient. It should also be noted that Eq. (75) is justified only if each weight for the estimator B_{ijk} is independent of k , which cannot be guaranteed in general. In the following section, we demonstrate the one-step MVD for the PE scheme. We prove that one-step MVD is effective for the PE scheme through numerical simulation. We also propose a novel method to improve the performance for sampling the physical ground state \mathbf{z}_g .

IV. EXPERIMENT AND RESULTS OF PE SCHEME

We performed a classical discrete-time Monte Carlo (DTMC) simulation to verify the validity of one-step MVD for the PE scheme. We used the rejection-free (RF) version of the MCMC simulation [35, 61], which is known as a jump or embedded-chain Monte Carlo [62–64]. In this method, all diagonal elements in the transition kernel are eliminated. This results in the elimination of self-loop transitions, that is, a state transitioning to itself, which is time consuming, specifically in low-temperature simulation. Although the modified kernel changes the stationary distribution from a Maxwell-Boltzmann (MB) distribution to a non-MB distribution, the mapping between these distributions is bijective so that we can always recover the MB distribution from the stationary distribution obtained by the RF MCMC simulation. The details of our RF MCMC algorithm are provided in the Appendix. We selected a spin-glass problem with $K = 14$ in which the coupling matrix \mathbf{J} is selected from random variables that are uniformly distributed in the range $[-1/4, 1/4]$ as an example. Figure 7 shows the spatial distribution of the assumed coupling matrix \mathbf{J} , wherein the element J_{ij} is the coupling coefficient between the spins i and j . The simulation was performed using the Mathematica[®] Ver. 13 platform on Windows 10/11 operating systems. Please refer to Ref. [35] for the details of our simulation.

Because the PE scheme has currently been developed for QA machines that are intended for solving combinatorial optimization problems, we consider that the target state to be sampled is the ground state \mathbf{Z}_g of the embedded logical spin systems described by the Hamiltonian $H^{\text{logi}}(\mathbf{Z})$ or, equivalently, the associated physical code state $\mathbf{z}_g = \mathbf{Z}_g \otimes \mathbf{Z}_g$. We compared the performance for sampling these target states using the decoding strategies (a) MAP decoding and (c) one-step MVD after MAP decoding.

For the MAP decoding, the RF MCMC attempts to sample the ground state \mathbf{z}'_g of the physical Hamiltonian $H^{\text{phys}}(\mathbf{z}) = -\beta H^{\text{loc}}(\mathbf{z}) - \gamma H^{\text{pen}}(\mathbf{z})$ in Eqs. (20)–(22) with $S_{ij}(\mathbf{z}) = S_{ij}^{\text{4w}}(\mathbf{z})$. Note that \mathbf{z}'_g depends on the set of weight parameters $\{\beta, \gamma\}$ and does not necessarily agree with \mathbf{z}_g ; it can even be a non-code state. This is in contrast with QAC, where the ground state of the Hamiltonians $H^{\text{QAC}}(\mathbf{z})$ (see Eq. (40))

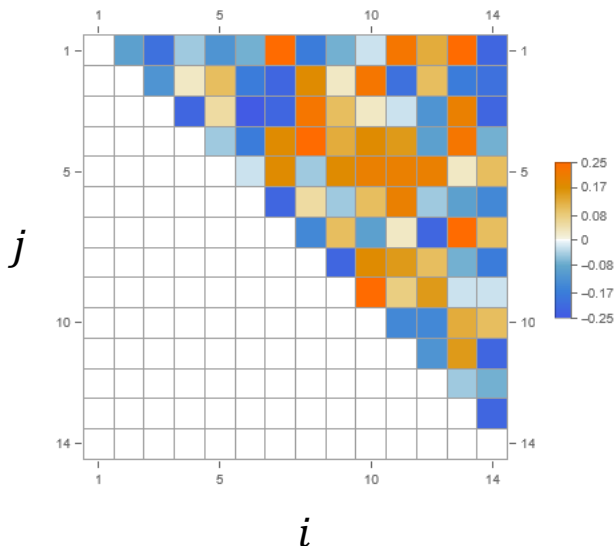


FIG. 7. Spatial distribution of the elements of the assumed coupling matrix \mathbf{J} .

is necessarily a code state because it is the common ground state of $H^{enc}(\mathbf{z})$ and $H^{pen}(\mathbf{z})$. Therefore, the condition $H^{pen}(\mathbf{z}) = 0$ is crucial for sampling the correct target state \mathbf{z}_g for the PE scheme. To sample the target state that is the lowest energy state of the local Hamiltonians $H^{loc}(\mathbf{z})$ in Eq. (20) under the condition $H^{pen}(\mathbf{z}) = 0$ using the Hamiltonian $H^{phys}(\mathbf{z})$, we implemented a bookkeeping operation after one-step MVD. We calculated the logical energy $H^{logi}(\mathbf{Z}^*)$ for the logical state \mathbf{Z}^* decoded from the readout \mathbf{r} sweep by sweep and retained only the readout with the lowest energy ever sampled in the bookkeeping. Using this online bookkeeping operation, which can be considered as an extra sampling or filtering process, we can achieve successful sampling at the end of the simulation once the target state is sampled during the annealing simulation.

In our previous study, we investigated the performance of the PE scheme based on only MAP decoding using the RF MCMC simulation [35]. We showed that the performance is largely dependent on the set of constant weight parameters $\{\beta, \gamma\}$ in the physical Hamiltonian $H^{phys}(\mathbf{z})$, which parameterizes the coupling strength of the thermal environment and its relative weight between two contributions $H^{loc}(\mathbf{z})$ and $H^{pen}(\mathbf{z})$ in the Hamiltonian $H^{phys}(\mathbf{z})$. Figure 8 shows the typical landscapes of the various probability distributions obtained by our simulation. Subfigures (a) and (b) depict the results of the MAP decoding, whereas (c) depicts the results of the one-step MVD inferred from the readout of the MAP decoding. In (a), the probability distribution p_c for sampling any code state that is the ground state of $H^{pen}(\mathbf{z})$, and in (b) and (c), the probability distribution p_g for sampling the target state \mathbf{z}_g and \mathbf{Z}_g , respectively, are plotted as functions of a set of weight parameters

$\{\beta, \gamma\}$. These results were obtained from the statistical analysis of 300 identical and independent simulations. We can observe from (a) that the code state can be obtained efficiently within a confined region on the $\{\beta, \gamma\}$ plane. Specifically, we note that p_c is very small for a sufficiently large γ , which might contradict the general belief that p_c should be almost unity for a sufficiently large γ . This might be a noteworthy observation. In addition, we cannot sample the code states for the region where γ is smaller than a certain limit, which is shown by the white broken line in (a). It is reasonable that the target state \mathbf{z}_g can be sampled only within the region on the $\{\beta, \gamma\}$ plane where the code states are available in (a), as the target state \mathbf{z}_g must be one of the code states. Therefore, the probability distribution in (b) is consistent with that in (a). However, if we introduce the one-step MVD after the MAP decoding, the probability distribution changes significantly.

In this study, we re-investigated the performance of the PE scheme after introducing one-step MVD for the readout sampled by the RF MCMC simulation, that is, the MP decoding. In addition to the one-step MVD given by Eqs. (75)–(77), we applied extra operations to deduce the logical state \mathbf{Z}^* from the physical state \mathbf{z}^* inferred by one-step MVD, as described later. Subfigure (c) in Fig. 8 is a typical result showing the landscapes of the probability distribution p_g for inferring the target state \mathbf{Z}_g successfully using the one-step MVD as a function of a set of weight parameters $\{\beta, \gamma\}$. We found that the MC iterations required to achieve a comparable success probability for inferring the target state were nearly 400 times smaller for one-step MVD after MAP decoding (subfigure (c)) than for MAP decoding (subfigure (b)). Remarkably, such a target state could be found only within the region $\{\beta, \gamma\}$, where we could not sample the code states using only MAP decoding. Note that the difference among these simulations lies in the post-readout one-step MVD as well as the bookkeeping operations to keep track of the best outcome during the simulation. This result suggests that the one-step MVD contributes sufficiently to the inference of the correct target state and this contribution originates from the non-code state sampled in the MAP decoding in the first stage.

Unfortunately, we could observe only the best result sampled during the simulation owing to the bookkeeping operation, which discards the useless readouts during the RF MCMC simulation. To understand the simulation, we performed a supplementary simulation to clarify the function and potential of the one-step MVD for the PE scheme. In the new simulation, we removed the bookkeeping operations from the algorithm. Instead, we sequentially pushed all sampled states during the RF MCMC simulation, that is, the MAP decoding, into the LIFO stack memory and copied its contents into storage memory. We performed an offline analysis for the stored series of readouts and investigated the function and potential of the one-step MVD. We investigated

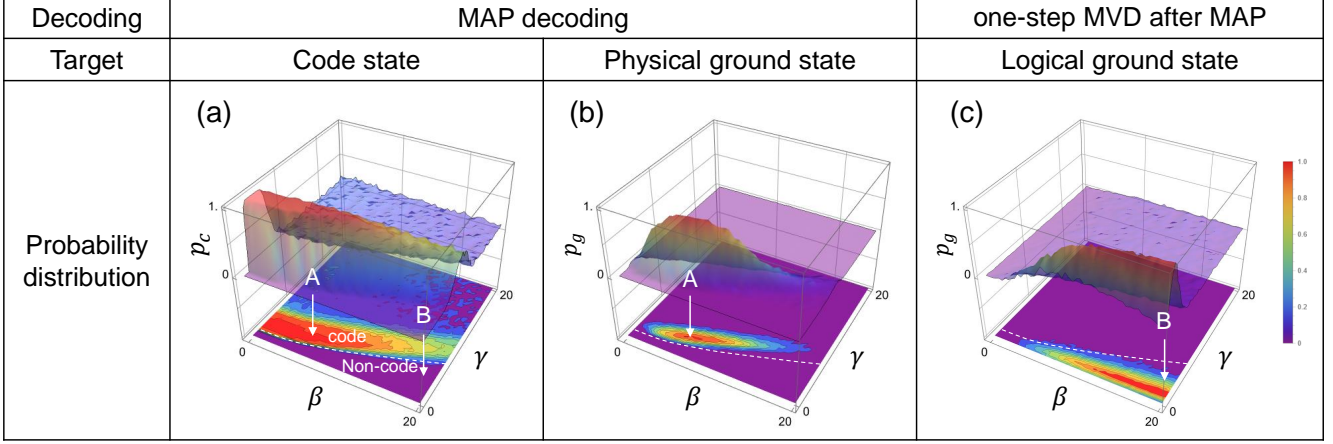


FIG. 8. Landscape of the probability distribution. Subfigures (a) and (b) are the results of the single-stage MAP decoding, whereas (c) is the result of one-step MVD for the readout of MAP decoding. The target state of (a) is any code state, whereas $\mathbf{z}_g = \mathbf{Z}_g \otimes \mathbf{Z}_g$ and \mathbf{Z}_g are the target states for (b) and (c), respectively. The probability distributions for sampling these target states are plotted as functions of the set of weight parameters $\{\beta, \gamma\}$.

two series of the associated readouts when the set of weight parameters $\{\beta, \gamma\}$ was fixed at A (case A) in Fig. 8, where both code and non-code states could be sampled, and B (case B) in Fig. 8, where only non-code states could be sampled by the MAP decoding. In the following, we first show the results for case A, followed by those for case B, and compare them. We analyzed $600K(K-1)-50$ samples with $K=14$, where the initial 50 samples in the burn-in periods were discarded.

Figure 9 shows the results for case A. The left panel shows the matrix plot of the marginal probability distribution for every spin, demonstrating an agreement between the orientations in the readout \mathbf{r} and target state \mathbf{z}_g , i.e., $r_{ij} = (z_g)_{ij}$. The warm-colored and cold-colored elements indicate probabilities higher and lower than $1/2$, respectively. Specifically, the orange and blue rectangles indicate the perfect alignment and anti-alignment of the orientation of the spin with that of the spin in the target state \mathbf{z}_g , respectively. Recall that the diagonal elements are fixed to $+1$ by construction. We can observe that the marginal probability distribution varies significantly spin by spin, and some spins tend to anti-align their orientations with the orientation of the spin in the target state \mathbf{z}_g . This marginal probability distribution depends on the distribution of the coupling constants as well as the values of the weight parameters $\{\beta, \gamma\}$. The panel on the right shows 10 readouts in the stored series of the readouts. The upper results are typical readouts randomly selected from the stored series, whereas the middle and lower results are the readouts for which the optimal estimate agrees with the code state, i.e., $\mathbf{z}^* = \mathbf{Z}^* \otimes \mathbf{Z}^*$, and the target state, i.e., $\mathbf{Z}^* = \mathbf{Z}_g$. In these figures, $\{\mathbf{e}(\mathbf{z}^*), \mathbf{E}(\mathbf{Z}^*)\}$ for the optimal estimates $\{\mathbf{z}^*, \mathbf{Z}^*\}$ and associated syndrome pattern $\mathbf{S}(\mathbf{z}^*)$ are plotted for a set of 10 selected readouts, where $\mathbf{e}(\mathbf{z}) =$

$\mathbf{z} \circ \mathbf{z}_g$ is an error pattern for the physical spin state \mathbf{z} , that is, $e_{ij} = z_{ij}(z_g)_{ij}$ ($i, j = 1, \dots, K$), and $\mathbf{E}(\mathbf{Z}) = \mathbf{Z} \circ \mathbf{Z}_g$ for the logical spin state \mathbf{Z} , that is, $E_i = Z_i(Z_g)_i$ ($i = 1, \dots, K$). Note that the elements in $\mathbf{e}(\mathbf{z})$ and $\mathbf{E}(\mathbf{Z})$ with a value of -1 imply that $z_{ij} \neq (z_g)_{ij}$ and $Z_i \neq (Z_g)_i$. Thus, they can be regarded as errors associated with the physical state \mathbf{z} and logical state \mathbf{Z} relative to their target states \mathbf{z}_g and \mathbf{Z}_g , respectively.

To clarify the interim readout \mathbf{r} before one-step MVD, we investigated the energy spectra for the readouts shown in Fig. 9. Figure 10 depicts various energy spectra when $\{\beta, \gamma\}$ is at point A . The upper histograms indicate the spectra of the Hamiltonian (a) $H^{phys}(\mathbf{r})$, (b) $H^{loc}(\mathbf{r})$, and (c) $H^{pen}(\mathbf{r})$, which are relative frequency distributions of the energy of the readout \mathbf{r} of the MAP decoding. It should be noted that \mathbf{r} may not necessarily be a code state. In these figures, the red bin indicates the contribution of the readouts for which the physical state \mathbf{z}^* inferred by one-step MVD agreed with the target state, i.e., $\mathbf{z}^* = \mathbf{z}_g$. In contrast, the gray bins indicate the contributions of the readouts for which the inferred state \mathbf{z}^* became the code state, i.e., $\mathbf{z}^* = \mathbf{Z}^* \otimes \mathbf{Z}^*$. The green bins indicate the contributions of the readouts for which the inferred state \mathbf{z}^* was not the code state, but the logical state \mathbf{Z}^* deduced from \mathbf{z}^* agreed with the target state \mathbf{Z}_g . The lower histogram (d) indicates the spectrum of the Hamiltonian $H^{logi}(\mathbf{Z}^*)$ after the readouts \mathbf{r} are decoded as the estimate \mathbf{Z}^* by the one-step MVD. It should be noted that if \mathbf{z} is a code state, $\mathbf{z} = \mathbf{Z} \otimes \mathbf{Z}$, and $H^{loc}(\mathbf{z}) = H^{logi}(\mathbf{Z})$ holds. The red, gray, and green bins in histogram (d) have the same meanings as those in the upper histograms. We can observe that green bins in histogram (b) are reduced to a single bin in histogram (d) after one-step MVD reflecting

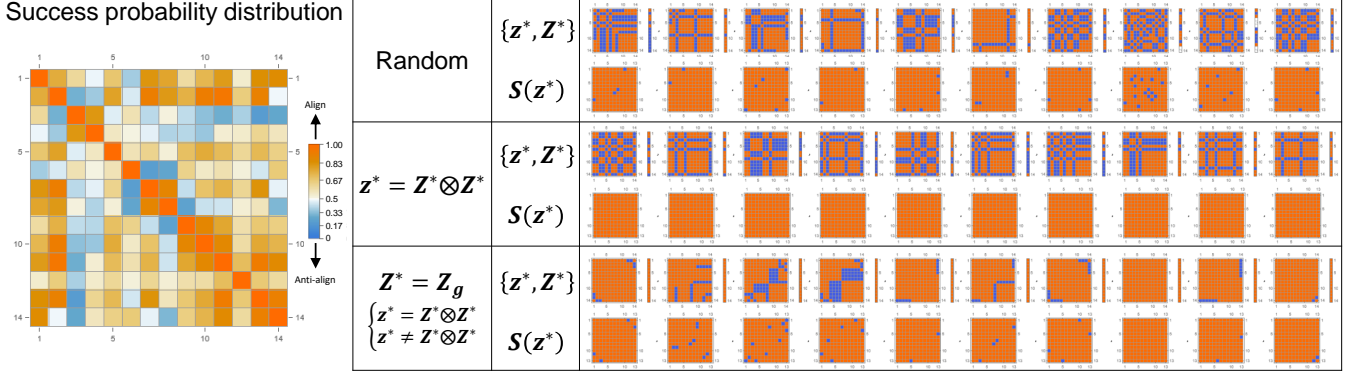


FIG. 9. Result of one-step MVD for the readout \mathbf{r} of MAP decoding when the weight parameters $\{\beta, \gamma\}$ are fixed to the value at which the code states can be frequently sampled. The left matrix plot shows the marginal probability distribution for every spin that demonstrated an agreement between the readout \mathbf{r} and target state \mathbf{z}_g . In the right panel, the error patterns $\{e(\mathbf{z}^*), \mathbf{E}(\mathbf{Z}^*)\}$ for the optimal estimate $\{\mathbf{z}^*, \mathbf{Z}^*\}$ (upper results) and associated weight-four syndrome pattern $\mathbf{S}(\mathbf{z}^*)$ (lower results) are shown for three selected sets of 10 readouts, i.e., randomly selected readouts, for which the inferred physical state \mathbf{z}^* agreed with one of the code states $\mathbf{z}^* = \mathbf{Z}^* \otimes \mathbf{Z}^*$, and for which the inferred logical state \mathbf{Z}^* agreed with the target state \mathbf{Z}_g . The blue element corresponds to an erroneous spin.

that decoding is a dimensionality-reducing operation. From histogram (d), we can observe that a significant number of the target states \mathbf{Z}_g is inferred by one-step MVD from the non-code states even if $\{\beta, \gamma\}$ is at point A. From the comparison of gray bins in histograms (b) and (d), we observe that the one-step MVD does not change the spectra of the code states.

Next, we discuss the results for case B in which $\{\beta, \gamma\}$ is fixed at point B in Fig. 11. The matrix plot of the marginal probability distribution for every spin exhibiting an agreement between the orientations in the readout \mathbf{r} and target state \mathbf{z}_g is shown on the left. We can observe that some spins have strong tendencies to anti-align their orientations with the orientation of the spin in the target state \mathbf{z}_g , which is similar to that when $\{\beta, \gamma\}$ is fixed at point A, although the distribution differs significantly. Specifically, several spins have a very large probability of being anti-aligned, with the value reaching nearly unity. The panels on the right-hand side show 10 readouts in the stored series of the readouts. The upper results are typical readouts that are randomly selected from the stored series, whereas the lower results are the readouts for which the optimal estimate agrees with the target state, i.e., $\mathbf{Z}^* = \mathbf{Z}_g$.

Figure 12 presents the various energy spectra of the readouts when $\{\beta, \gamma\}$ is at point B. The upper histograms indicate the spectra of the Hamiltonian (a) $H^{phys}(\mathbf{r})$, (b) $H^{loc}(\mathbf{r})$, and (c) $H^{pen}(\mathbf{r})$ for the readout \mathbf{r} , whereas the lower histogram shows the spectrum of the Hamiltonian (d) $H^{logi}(\mathbf{Z}^*)$ for the estimate \mathbf{Z}^* . In these figures, the colored bins have the same meaning as those in Fig. 10. It can be observed that there is no red bin, which indicates that no target state \mathbf{z}_g can be sampled by the MAP decoding. Nevertheless, a single

and significantly large green bin can be observed in the ground state $\mathbf{Z}^* = \mathbf{Z}_g$ of the Hamiltonian (d) $H^{logi}(\mathbf{Z}^*)$. It is evident from the spectrum of $H^{pen}(\mathbf{r})$ that the estimate \mathbf{Z}^* originates from the readouts in the non-code state space. This proves that our one-step MVD is suitable for decoding the target state \mathbf{Z}_g from the readouts \mathbf{r} , that is, the non-code states sampled by the MAP decoding in the first stage.

Unfortunately, we discovered later that our decoding algorithm had a flaw, although it was subsequently solved. The issue was related to the deduction of the estimator $\mathbf{Z}^* \in \{\pm 1\}^K$ from the optimal estimator $\mathbf{z}^* \in \{\pm 1\}^{K \times K}$ obtained through one-step MVD. If \mathbf{z}^* is the code state, we obtain $\mathbf{z}^* = (\mathbf{z}^*)^T = \mathbf{Z}^* \otimes \mathbf{Z}^*$. In this case, we can easily deduce \mathbf{Z}^* up to a global sign as

$$\mathbf{Z}^* = \mathbf{z}_i^* = (z_{i1}^*, \dots, z_{iK}^*) \quad (78)$$

for an arbitrary $i = 1, \dots, K$. However, if \mathbf{z}^* is a non-code state, $\mathbf{z}^* \neq \mathbf{Z}^* \otimes \mathbf{Z}^*$, and Eq. (78) does not necessarily hold. In this case, the derivation of \mathbf{Z}^* is nontrivial, although this is resolved later. We attempted to deduce the unique \mathbf{Z}^* in an ad-hoc manner, as follows. In our decoding algorithm, we first estimated the physical state using one-step MVD according to $\mathbf{z}^* = \text{sgn}[\mathcal{F}(\mathbf{r})]$, where $\mathcal{F}(\mathbf{r}) = \mathbf{r}(\mathbf{r} - \mathbf{I}) \sim \mathbf{r}^2$. Subsequently, we performed an extra majority vote for \mathbf{z}^* by assuming that $\text{sgn}[(\mathbf{z}^* \mathbf{z}^*)_{1i}] = \text{sgn}\left[\sum_{k=1}^K z_{1k}^* z_{ki}^*\right]$ gives a good estimate of $\mathbf{Z}_1^* \mathbf{Z}_i^*$, where z_{1k}^* is considered to eliminate a global sign flip of \mathbf{Z}^* . Note that, if $\mathbf{z}^* = \mathbf{Z}^* \otimes \mathbf{Z}^*$ holds, we have $z_{ij}^* = \mathbf{Z}_i^* \mathbf{Z}_j^*$ and $\mathbf{Z}_i^* = \mathbf{Z}_1^* \text{sgn}[(\mathbf{z}^* \mathbf{z}^*)_{1i}]$, but this ad-hoc assumption is not justifiable theoretically. All of the above results were obtained using this strategy. However, we found later that this was not an appropriate

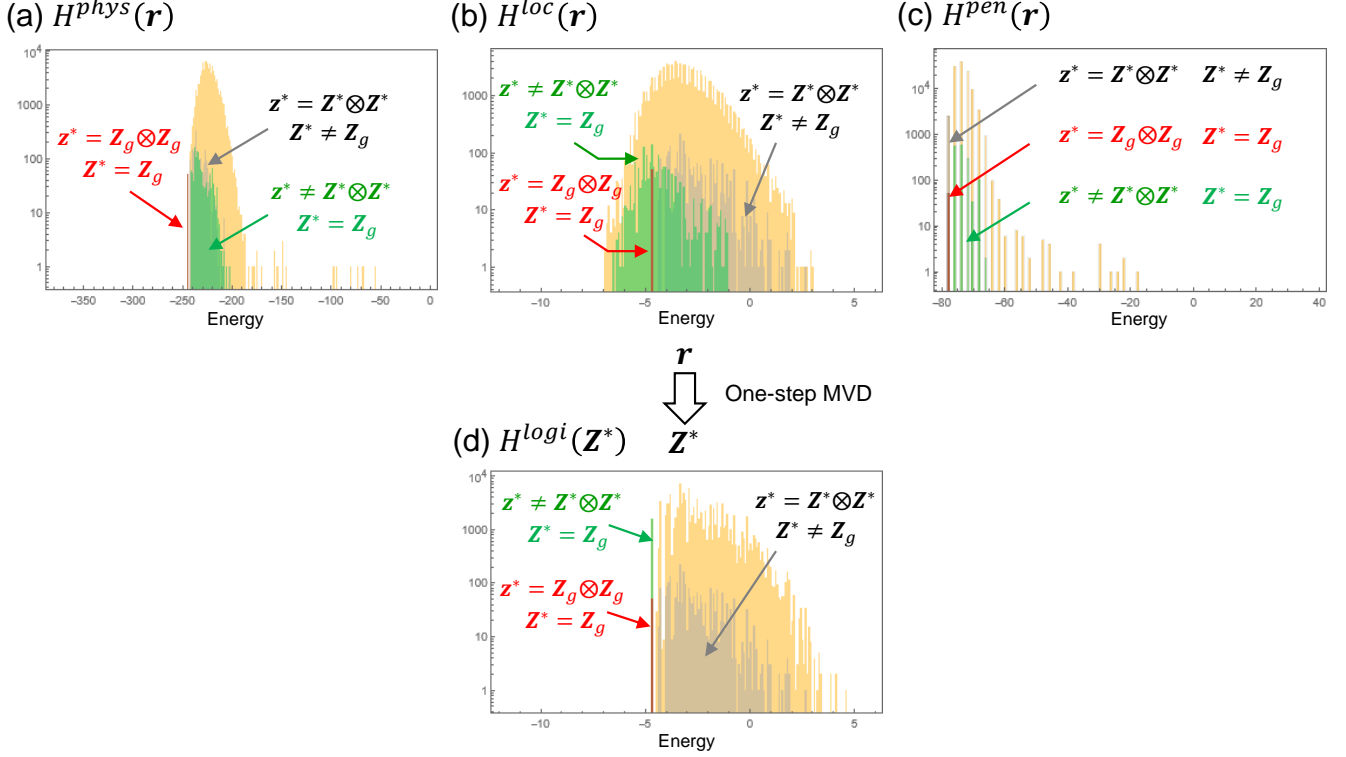


FIG. 10. Energy spectra of the sampled readouts \mathbf{r} (upper histograms) and estimate \mathbf{Z}^* obtained from \mathbf{r} (lower histogram). The upper histograms (a)-(c) indicate the energy spectra associated with the Hamiltonian (a) $H^{phys}(\mathbf{r})$, (b) $H^{loc}(\mathbf{r})$, and (c) $H^{pen}(\mathbf{r})$. The lower histogram (d) indicates the energy spectra associated with the Hamiltonian $H^{logi}(\mathbf{Z}^*)$. The red, gray, and green bins show the contributions of the readouts for which $\mathbf{z}^* = \mathbf{z}_g$, $\mathbf{z}^* = \mathbf{Z}^* \otimes \mathbf{Z}^*$ but $\mathbf{Z}^* \neq \mathbf{Z}_g$, and $\mathbf{Z}^* = \mathbf{Z}_g$ but $\mathbf{z}^* \neq \mathbf{Z}^* \otimes \mathbf{Z}^*$, respectively.

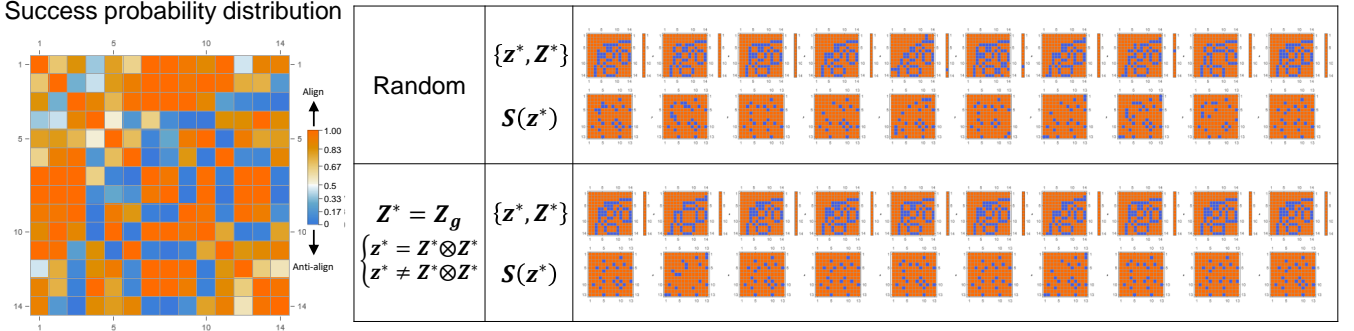


FIG. 11. Results of one-step MVD for the readout of MAP decoding when the weight parameters $\{\beta, \gamma\}$ are fixed to the value at which almost no code state can be sampled. The left matrix plot shows the marginal probability distribution for every spin exhibiting an agreement between the orientation in the readout \mathbf{r} and the target state \mathbf{z}_g . In the right panel, the error patterns $\{e(\mathbf{z}^*), \mathbf{E}(\mathbf{Z}^*)\}$ for the optimal estimate $\{\mathbf{z}^*, \mathbf{Z}^*\}$ (upper results) and associated weight-four syndrome pattern $\mathbf{S}(\mathbf{z}^*)$ (lower results) are shown for two sets of 10 readouts, i.e., for randomly selected readouts and the readouts for which the inferred logical state \mathbf{Z}^* agreed with the target state \mathbf{Z}_g .

approach. To comprehend the related problem, let us consider an example of the readout \mathbf{r} shown in Fig. 13 that was inferred as the target state \mathbf{Z}_g in our strategy. The plots in (a) depict the target states: the upper and lower traces are the target physical state $\mathbf{z}_g = \mathbf{Z}_g \otimes \mathbf{Z}_g$

and logical ground state \mathbf{Z}_g , respectively. The plots in (b) depict the readout state \mathbf{r} (upper) and the state \mathbf{Z}^* decoded through our strategy (lower), which is the target state \mathbf{Z}_g . The plots in (c) depict the error patterns $e(\mathbf{r}) = \mathbf{r} \circ \mathbf{z}_g$ for the readout \mathbf{r} and $\mathbf{E}(\mathbf{Z}^*) = \mathbf{Z}^* \circ \mathbf{Z}_g$ for

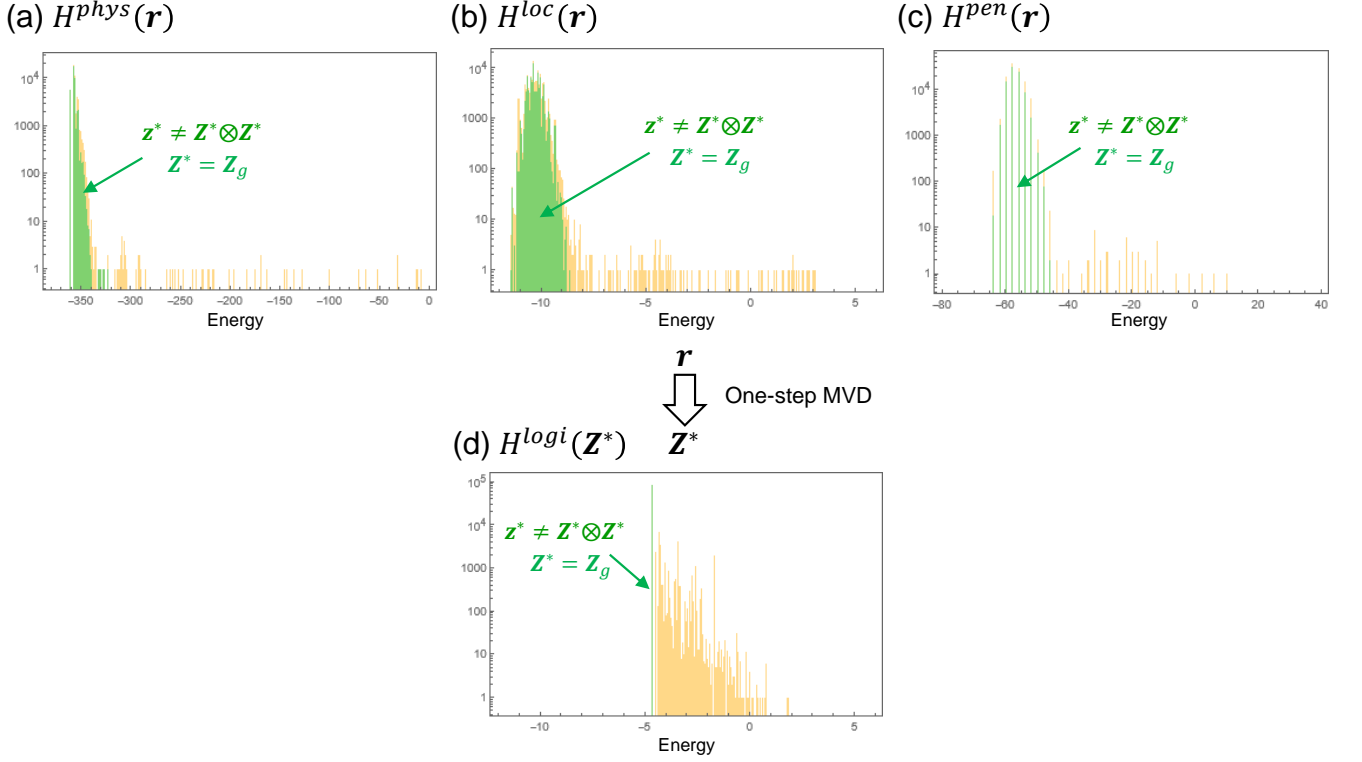


FIG. 12. (a)-(c) Energy spectra of the sampled readouts \mathbf{r} (upper histograms) and (d) estimate \mathbf{Z}^* obtained from \mathbf{r} (lower histogram).

the estimator \mathbf{Z}^* . The error patterns $\mathbf{e}(\mathbf{r})$ and $\mathbf{E}(\mathbf{Z}^*)$ have elements with values of -1 , i.e., erroneous spins.

We can transform the Hamiltonian $H^{phys}(\mathbf{z})$ into $H^{phys}(\mathbf{e})$ through the gauge transformations $J_{ij} \rightarrow J_{ij}(z_g)_{ij}$ and $z_{ij} \rightarrow e_{ij}$ if we know z_g a priori. The Hamiltonian $H^{phys}(\mathbf{e})$ has a trivial ground state \mathbf{e}_g with $(e_g)_{ij} = +1$ for all i and j . We can also transform the Hamiltonian $H^{logi}(\mathbf{Z})$ into $H^{logi}(\mathbf{E})$ using the gauge transformations $J_{ij} \rightarrow J_{ij}(Z_g)_i(Z_g)_j$ and $Z_i \rightarrow E_i$ if we know \mathbf{Z}_g a priori. The Hamiltonian $H^{logi}(\mathbf{E})$ has a trivial ground state \mathbf{E}_g with $(E_g)_i = +1$ for all i . The upper and lower results in (c) depict the error patterns $\mathbf{e}(\mathbf{r})$ and $\mathbf{E}(\mathbf{Z}^*)$ for the readout state \mathbf{r} shown in (b). We can observe that the error pattern $\mathbf{e}(\mathbf{r})$ reflects the marginal probability distribution shown in Fig. 11, although the error pattern $\mathbf{E}(\mathbf{Z}^*)$ is its ground state \mathbf{E}_g . It should be noted that the error pattern $\mathbf{e}(\mathbf{r})$ has the elements $(\mathbf{e}(\mathbf{r}))_{i1} = (\mathbf{e}(\mathbf{r}))_{1i} = +1$ and $(\mathbf{e}(\mathbf{r}))_{i2} = (\mathbf{e}(\mathbf{r}))_{2i} = +1$ for $i = 1, \dots, N$, which implies that the readouts $r_{ij} = r_{ji}$ ($j = 1$ or 2) are sufficient to infer the target state \mathbf{Z}_g up to its global sign. These error-free elements with respect to the target logical state \mathbf{Z}_g may be the reason that our strategy for inferring the ground state \mathbf{Z}_g succeeded. Figure 14 depicts the calculated results of $Z(i) = \text{sgn}[(\mathbf{z}^* \mathbf{z}^*)_{ij}]$ for $i = 1, \dots, N$ using the readout \mathbf{r} shown in Fig. 13 (b). Clearly, the target state \mathbf{Z}_g can be inferred up to its global sign only if we

select $i = 1$ and 2 . This suggests that the crucial reason for the success of our strategy is the subset of the error-free readouts $\mathbf{r}_i = (r_{i1}, \dots, r_{iK})$ or $\tilde{\mathbf{r}}_i = (r_{1i}, \dots, r_{Ki})^T$ associated with the logical lines for $i = 1$ and 2 of the readout state \mathbf{r} . That is, the simulation results presented thus far depended on these readouts.

Our strategy is not sufficient to infer the target state for general problem instances. To demonstrate this, we show the result for another problem instance with the inverted coupling constants $\mathbf{J} \rightarrow -\mathbf{J}$. The left plot in Fig. 15 indicates the landscape of the probability distribution p_g for successfully inferring the target logical state \mathbf{Z}_g using our strategy, and the right plot indicates the marginal probability distribution for successfully sampling the target physical state $\mathbf{z}_g = \mathbf{Z}_g \otimes \mathbf{Z}_g$ when the weight parameters $\{\beta, \gamma\}$ are fixed at point B' in the left plot. In contrast to the previous result shown in Figs. 7, 8, and 11, we could not find a logical line where the success probability for all involved elements was no less than $1/2$. This suggests that our strategy has limited validity and its success depends on the problem instances. In fact, the success probability for sampling the target state was smaller for this instance than in the instance shown in Fig. 8 (c), even though the number of readout samples was the same.

Eventually, we concluded that it is important and necessary to develop a decoding method that can infer the target state for any problem instance without its

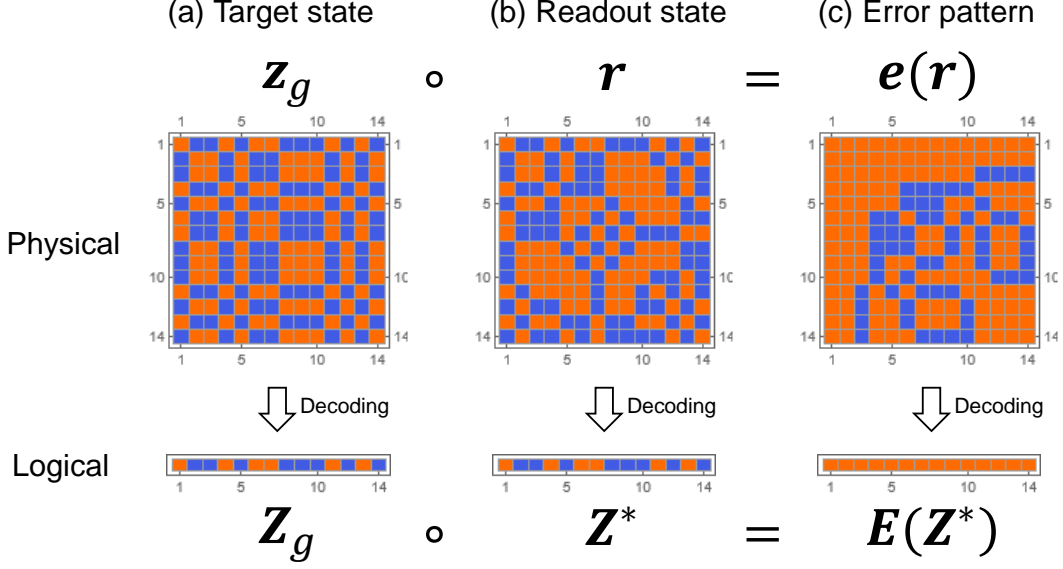


FIG. 13. An example of the results of our strategy to deduce \mathbf{Z}^* .

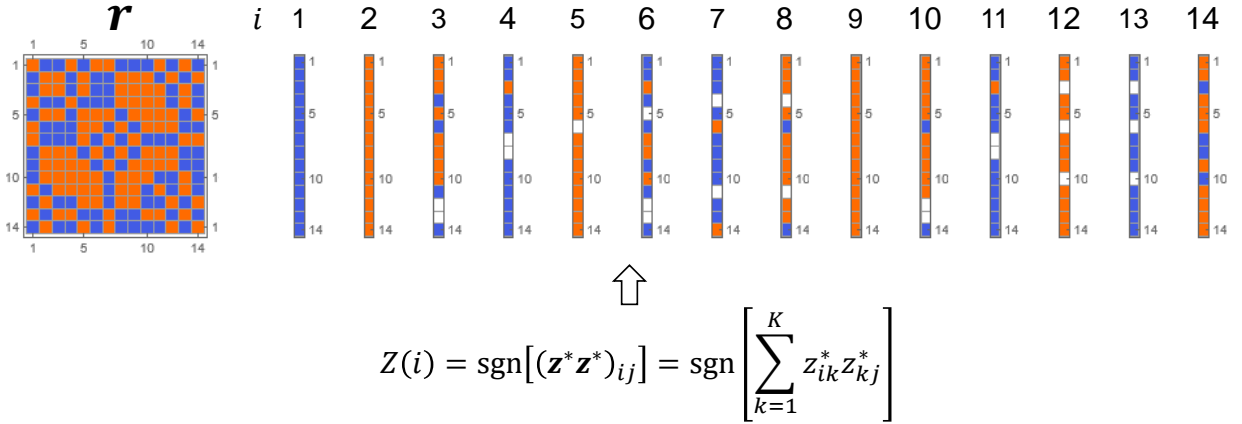


FIG. 14. Evidence of a flaw in our strategy. The white elements denote an undefined state associated with the tie vote.

detailed knowledge. For this purpose, we developed a decoding method that can infer the physical target state $\mathbf{z}_g = \mathbf{Z}_g \otimes \mathbf{Z}_g$ without errors. This is a novel post-readout decoding procedure that is applicable to an arbitrary problem instance. We show that this is actually possible by extending our one-step MVD algorithm to the incorporation of majority voting of greater than weight-two orthogonal estimators. Let us consider the following matrix function:

$$\mathcal{F}(\mathbf{X}) := \mathbf{X}(\mathbf{X} - \mathbf{I}), \quad (79)$$

where \mathbf{X} is a symmetric square bipolar matrix with unit diagonal elements and \mathbf{I} is the identity matrix in the matrix space of \mathbf{X} . Then, the standard one-step MVD is based on up to weight-two orthogonal estimators

$$\mathbf{z}^* = \text{sgn}[\mathcal{F}(\mathbf{r})]. \quad (80)$$

Next, we extend this to include up to weight- $2n$ orthogonal estimators

$$\mathbf{z}^*(n) = \text{sgn} \left[\mathcal{F}^{(n)}(\mathbf{r}) \right], \quad (81)$$

where

$$\mathcal{F}^{(n)}(\mathbf{X}) := \mathcal{I} \circ \underbrace{\mathcal{F} \circ \mathcal{F} \circ \dots \circ \mathcal{F}}_n(\mathbf{X}) \quad (82)$$

is an n -iteration of \mathcal{F} on \mathbf{X} . Note that $\mathcal{F}^{(n)}(\mathbf{r})$ consists of the sum of the terms involving up to $2n$ -multiplication of matrix elements r_{ij} , where every r_{ij} is treated symmetrically and on an equal footing, that is, exchanging two arbitrary r_{ij} and $r_{i'j'}$ does not change $\mathcal{F}^{(n)}(\mathbf{r})$. In addition, the matrix element

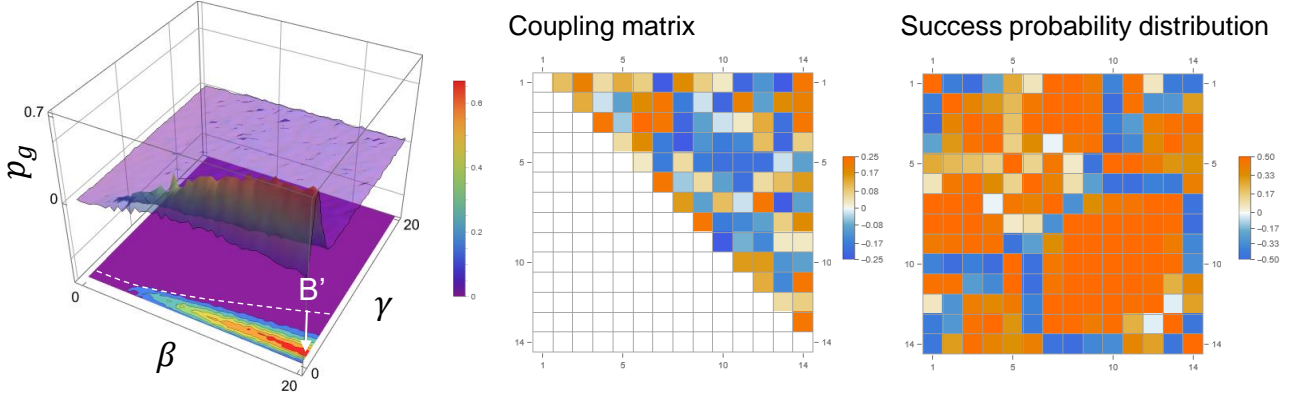


FIG. 15. Another problem instance demonstrating the limitation of our strategy. The success probability for sampling the target state \mathbf{Z}_g using our strategy, coupling matrix \mathbf{J} , and marginal probability distribution for every spin exhibiting an agreement between the orientation in the readout \mathbf{r} and the target state \mathbf{z}_g .

$(\mathcal{F}^{(n)}(\mathbf{r}))_{ij}$ is considered to consist of all possible weight- $2m$ ($m = 1, \dots, n$) estimators orthogonal on z_{ij} , which would ensure fair majority voting. It has been pointed out that majority voting involving such high-weight syndromes may improve the performance at the expense of increasing the calculation cost [25]. We compared the estimator obtained from Eq. (81) for an increasing number of iterations n . Figure 16 depicts the matrix plots of the error pattern of $\mathbf{z}^*(n)$ for the two readouts \mathbf{r} shown in Figs. 11 and 15. It is clear that the errors in $\mathbf{z}^*(n)$ are reduced as n increases and reaches the target state \mathbf{z}_g . We investigated numerous examples to check the trend of $\mathbf{z}^*(n)$ against an increasing n and confirmed similar behaviors for all the examples. Therefore, we concluded that Eq. (81) is a practical and effective estimator for the physical target state \mathbf{z}_g for a large n . By combining this technique with the energy calculation, we expect that this technique can assist in sampling the physical target states \mathbf{z}_g using various sampling techniques. For example, we can consider two scenarios, as follows. We calculate the physical energy $H^{phys}(\mathbf{z}^*(n))$ for the estimated state $\mathbf{z}^*(n)$ for a given n . We can keep track of the lowest possible value of $H^{phys}(\mathbf{z}^*(n))$ and the associated $\mathbf{z}^*(n)$ during the sampling process in bookkeeping, and output the best physical state $\mathbf{z}^*(n) = \min_n H^{phys}(\mathbf{z}^*(n))$ at the end of the simulation. Alternatively, we can calculate the logical energies $H^{logi}(z_i^*(n))$ of the estimator $z_i^*(n)$ for a given n and $i = 1, \dots, N$, where $\mathbf{z}^*(n) = (z_{i1}^*(n), \dots, z_{iN}^*(n))$ is the logical line i (the i th row vector) of $\mathbf{z}^*(n)$. We can track the lowest possible value of $H^{logi}(z_i^*(n))$ and the associated $z_i^*(n)$ during the sampling process and output the best logical state $z_i^*(n) = \min_n H^{logi}(z_i^*(n))$ at the end of the simulation. Obviously, both methods consume some classical computational resources, which should be a polynomial of the size of the problem N if we can fix n . However, it is plausible that n depends

on N . In this case, we need to introduce an appropriate cutoff for n to cope with the problems associated with the performance tradeoff. Further analysis is required to clarify the validity of the present method and optimize it for the PE scheme.

Both MAP decoding and one-step MVD after MAP decoding may infer the correct target state. However, their working principles are very different. MAP decoding attempts to sample the target state \mathbf{z}_g directly by statistically sampling the state that minimizes the physical Hamiltonian $H^{phys}(\mathbf{z})$, by which the state should satisfy the parity constraints. In contrast, one-step MVD after MAP decoding samples a neighboring state of the target state $\mathbf{r} \sim \mathbf{z}_g$, regardless of whether it violates the parity constraints in the first-stage MAP decoding, and converts it into the target state \mathbf{z}_g deterministically using the information on syndrome patterns without supplemental information in the second-stage one-step MVD. Thus, MAP decoding can be regarded as a purely stochastic algorithm, whereas one-step MVD after the MAP decoding can be regarded as a hybrid of stochastic and deterministic algorithms. Our two-stage decoding method for the PE scheme can be regarded as similar to the proposal of Sourlas for soft annealing, wherein computationally difficult problems can be simplified by embedding them into those in the larger system because one can circumvent the barriers using the deterministic algorithm and accelerate the dynamics of the algorithm while retaining all essential properties of the problem [7]. Similarly, finite temperature decoding of QAC may be regarded as an alternate version of soft annealing based on the classical repetition codes [22, 23].

We should comment on an inconsistency between the previously reported result and the current result. We concluded that one-step MVD is very useful in inferring the correct target state from the erroneous but correctable states that may arise in the PE scheme.

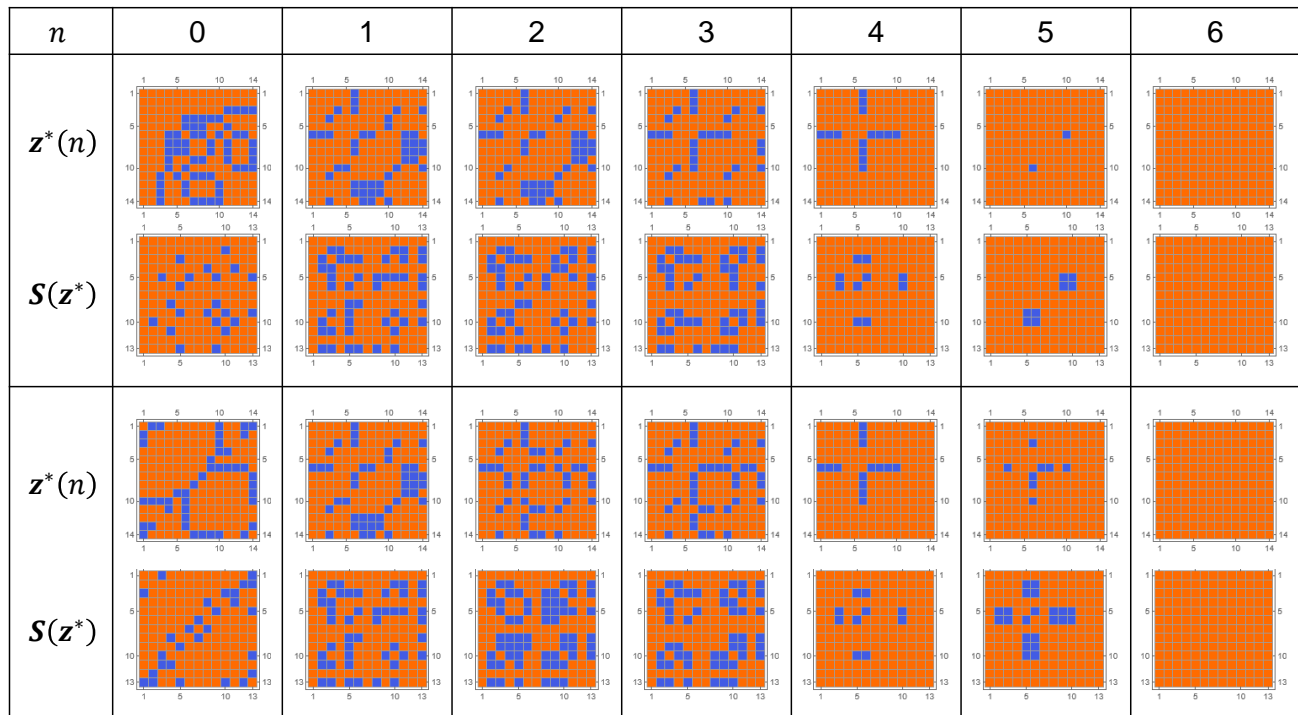


FIG. 16. Matrix plots for visualizing the error patterns of $\mathbf{z}^*(n)$ and weight-four syndrome patterns $\mathcal{S}(\mathbf{z}^*(n))$ with the element $S_{ij}^{4w}(\mathbf{z}^*(n))$ for two readouts \mathbf{r} . Note that $\mathbf{z}^*(n=0) = \mathbf{r}$.

Albash et al. reported a contradictory conclusion in their study [9], in which the validity of one-step MVD on the PE scheme was investigated based on classical Monte Carlo simulations. They reported that no clear evidence for the validity of the one-step MVD was observed. They claimed that majority voting schemes that attempt to exploit a large number of decoding trees are not beneficial because the error generated during the simulations is not an uncorrelated random error. Their claim appears to be in conflict with ours, as we confirmed that our novel one-step MVD using iterative matrix multiplications is valid for a wide range of error patterns in the readout \mathbf{r} , provided that the maximum number of errors N_{err} in every row (column) of \mathbf{r} satisfies $N_{err} < \frac{K-1}{2}$. Note that a row (column) of \mathbf{r} , i.e., its logical line, is a star-like spanning tree with $K-1$ variable elements (recall that all diagonal elements of \mathbf{r} are fixed to $+1$ by assumption). We point out two possible reasons for the inconsistency between the two studies. First, the estimator used for inferring the target state differs between the two studies. In our study, we used the estimator derived from orthogonal syndromes, which would ensure fair majority voting. In contrast, the previous study used a majority vote over the subsets of the readouts \mathbf{r} , describing the spanning trees on the logical spins to determine the target state \mathbf{Z}_g up to a global spin flip fully. However, this approach lacks theoretical grounding and may be questionable from the viewpoint of the fairness of the majority vote. Second, the previous study focused on

simulations with specific simulation parameters and an annealing schedule selected based on values associated with actual QA devices. The authors did not necessarily preclude the validity of post-readout decoding of the PE scheme for any simulation parameter or schedule. In our opinion, the first reason is rather important. The majority vote based on the random spanning tree method does not consider the fair use of the prior knowledge on the parity constraints and cannot be justified.

V. CONCLUSIONS

We have studied two classical error-correcting schemes for solving combinatorial optimization problems based on the dynamical relaxation process of Ising spins towards their ground states. First, we reviewed the concept of soft annealing introduced by Sourlas and examined how an Ising spin Hamiltonian is embedded into an extended Hamiltonian with classical error-correction codes and the tacit assumptions made therein. It was clarified that the informative prior for parity constraints is the source of the penalty Hamiltonian, which was introduced ad-hoc into the Hamiltonian in many previous studies.

Subsequently, we addressed two classical error-correction schemes used for QA, namely the QAC and PE schemes, and investigated their derivation from the above concept. In QAC, the classical repetition code is merged to the logical Hamiltonian and encoded into

the Hamiltonian describing a larger system composed of many copied systems (replicas). These replicas are mutually independent if the penalty Hamiltonian is omitted; otherwise, they are mutually correlated. It is obvious that if the copies are independent, the QAC executes sampling and measurement for independent replicas in parallel in a single-shot operation, instead of repeating the same operation on a single copy. The results should be consistent with the measurements of repeated experiments using a single copy. If the penalty term is introduced, it should produce a positive correlation among the replicas, which may be utilized to improve the sampling efficiency. This is very similar to extended ensemble algorithms, such as replica exchange and parallel tempering, in classical statistical physics [65] as well as simulated QA using the path-integral Monte Carlo method [43–46], where the dynamics of an ensemble comprising the mutually interacting replicas are considered [66–68]. In the PE scheme, soft annealing provides the encoded physical Hamiltonian directly, but its interpretation is not necessarily straightforward compared with that of the QAC.

The information in the logical Hamiltonian that is embedded in the physical Hamiltonian should be retrieved by decoding. By exploiting the advantage of the informative prior for the parity constraints, we can increase the reliability of the decoding in two manners. In the case of MAP decoding, the readouts of all physical spins provide the outcome without post-readout processing. We need to sample the code state with the lowest energy to infer the target state. This can only be achieved by balancing the weights of the penalty and non-penalty Hamiltonians appropriately. In this case, the informative prior is used only for the pre-readout process, that is, the stochastic sampling process. In addition, we can exploit the advantage of the informative prior for the post-readout process. By exploiting this advantage, we can retrieve the target state from the non-code but correctable erroneous state in which some of the parity constraints may be violated. This can be accomplished through one-step MVD, which fairly exploits the parity constraints as an informative prior. We discussed the one-step MVD for QAC and the PE scheme. One-step MVD for QAC is relatively simple to understand. We identify logical groups as sets of physical spins connected by ferromagnetic penalty couplings in the QAC Hamiltonian [6, 17–24]. The spins in the logical Hamiltonian are identified with the logical groups in the QAC Hamiltonian. One-step MVD is equivalent to assigning the average orientation of the physical spins in the logical group to the orientation of the associated logical spin. If these assignments are successful for every logical spin with respect to the target logical spin states, we obtain a successful inference. If the penalty Hamiltonian is absent, this is analogous to finite temperature decoding, where thermal fluctuation contributes to improving the decoding performance.

In contrast, the post-readout decoding for the PE

scheme is more subtle. In this study, we found that efficient decoding through one-step MVD is possible by exploiting the higher-weight syndromes in the optimal estimators. We demonstrated the algorithm for realizing this using an iteration of matrix multiplications and sign decisions for each element in the resultant matrix. We confirmed the validity of our algorithm for numerous examples with various error patterns. The RF MCMC simulation showed that a huge number of non-code but correctable erroneous states contributes to the inference of the target state by exploiting the advantage of the informative prior in one-step MVD. Although our simulation results strongly suggest that one-step MVD might be more advantageous than MAP decoding in terms of performance, the classical overhead related to post-readout processing should be considered. The advantageousness of the approach depends on the sampler used for the first stage as well as the available classical computing resources. A detailed study is required to decide the usefulness of our technique in practical scenarios.

ACKNOWLEDGMENTS

The author acknowledges Dr. Yuki Susa, Dr. Yuki Kobayashi, Dr. Ryouji Miyazaki, Dr. Akihiro Yatabe, Dr. Tomohiro Yamaji, and Dr. Masayuki Shirane of NEC Corporation for their helpful discussions and comments. This paper is partly based on the results obtained from a project, JPNP16007, commissioned by the New Energy and Industrial Technology Development Organization (NEDO), Japan.

Appendix: Rejection-free Markov chains

In this appendix, we explain rejection-free Markov chains (RFMCs) and the connection between the stationary distribution for an RFMC and Maxwell Boltzmann (MB) distribution, which is the stationary state for standard reversible Markov chains (standard MCs). The standard MC is the reasonable classical model for an open system connected to a thermal environment. We focused on a discrete-time Markov chain (DTMC). We conducted a Monte Carlo simulation to confirm the theoretical prediction using a toy model. First, we briefly reviewed the stationary state in the reversible DTMC and RFMC. The reversible DTMC is characterized by its transition kernel

$$\mathbf{P} = \begin{pmatrix} p_{11} & p_{12} & p_{13} & \cdots & p_{1n} \\ p_{21} & p_{22} & p_{23} & \cdots & p_{2n} \\ p_{31} & p_{32} & p_{33} & \cdots & p_{3n} \\ \vdots & \vdots & \vdots & \ddots & \vdots \\ p_{n1} & p_{n2} & p_{n3} & \cdots & p_{nn} \end{pmatrix}, \quad (\text{A.1})$$

where p_{ij} is the transition probability of the system from state i to state j . Because \mathbf{P} is a stochastic matrix, the

sum of the matrix elements in each row is unity.

$$\mathbf{P}\mathbf{1} = \sum_{j=1}^n p_{ij} = \mathbf{1}, \quad (\text{A.2})$$

where $\mathbf{1} = (1, \dots, 1)^T$ is the column vector with all elements having the value 1. Therefore, the vector $\mathbf{1}$ is a right eigenvector with eigenvalue $\lambda = 1$. Here, the diagonal elements p_{ii} ($i = 1, \dots, n$) represent the probability of self-loop transition, i.e., a state transitioning to itself, resulting in no change in the state. The probability $\alpha_i = \sum_{j \neq i} p_{ij} = 1 - p_{ii}$ is the transition probability from i to another state $j \neq i$. In the Markov chains characterized by the transition kernel \mathbf{P} (abbreviated chain \mathbf{P}), a series of events with only two possible outcomes, i.e., the event that the system escapes from the state i and its exclusive event that the system stays in the state i , is described using Bernoulli trials, with the probability of success in each trial equal to α_i . Thus, the probability $p_i(t)$ that the system remains in the state i for t rounds is given by the geometric distribution characterized by a parameter α_i , that is,

$$p_i(t) = (1 - \alpha_i)^{t-1} \alpha_i. \quad (\text{A.3})$$

The average value of t is called the waiting time

$$\langle t_i \rangle = \sum_{t=1}^{\infty} t p_i(t) = \frac{1}{\alpha_i}. \quad (\text{A.4})$$

Consider the probability vector $\mathbf{v} = (v_1, \dots, v_n)^T$ with the element $v_i \in [0, 1] \in \mathbb{R}$, which is the probability that the system is in the state i and satisfies

$$\sum_{i=1}^n v_i = 1. \quad (\text{A.5})$$

If the chain \mathbf{P} is ergodic and satisfies the detailed balance conditions $v_i p_{ij} = v_j p_{ji}$, \mathbf{v} approaches a unique stationary distribution $\boldsymbol{\pi} = (\pi_1, \dots, \pi_n)^T$ that satisfies the global balance equation

$$\boldsymbol{\pi}^T = \boldsymbol{\pi}^T \mathbf{P} \quad (\text{A.6})$$

after numerous rounds of state transition. Equation (A.1) indicates that $\boldsymbol{\pi}$ is the left eigenvector of the eigen-equation with eigenvalue $\lambda = 1$. Furthermore, if the chain \mathbf{P} is aperiodic, $\boldsymbol{\pi}$ is also a limiting distribution, that is, $\boldsymbol{\pi} = \lim_{t \rightarrow \infty} \mathbf{v}$. If the system is open to the thermal environment, the detailed balance conditions lead to

$$\frac{\pi_i}{\pi_j} = \frac{p_{ji}}{p_{ij}} = \frac{\exp(-\beta E_i)}{\exp(-\beta E_j)} = \exp[-\beta(E_i - E_j)], \quad (\text{A.7})$$

where β is the inverse temperature of the environment and E_i is the energy of the system when it is in the state i . In this case, $\boldsymbol{\pi}$ is given by the MB distribution

$$\pi_i = \frac{\exp[-\beta E_i]}{Z}, \quad (\text{A.8})$$

where Z is a normalization constant called the canonical partition function.

Based on the above formulation for the standard MC, we define the RFMC and clarify how it is different from the standard MC. We define the RFMC as a reversible MC with the transition kernel given by the following matrix $\tilde{\mathbf{P}}$, whose diagonal elements are all zero:

$$\begin{aligned} \tilde{\mathbf{P}} &= \begin{pmatrix} \tilde{p}_{11} & \tilde{p}_{12} & \tilde{p}_{13} & \cdots & \tilde{p}_{1n} \\ \tilde{p}_{21} & \tilde{p}_{22} & \tilde{p}_{23} & \cdots & \tilde{p}_{2n} \\ \tilde{p}_{31} & \tilde{p}_{32} & \tilde{p}_{33} & \cdots & \tilde{p}_{3n} \\ \vdots & \vdots & \vdots & \ddots & \vdots \\ \tilde{p}_{n1} & \tilde{p}_{n2} & \tilde{p}_{n3} & \cdots & \tilde{p}_{nn} \end{pmatrix} \\ &= \begin{pmatrix} 0 & \frac{p_{12}}{\alpha_1} & \frac{p_{13}}{\alpha_1} & \cdots & \frac{p_{1n}}{\alpha_1} \\ \frac{p_{21}}{\alpha_2} & 0 & \frac{p_{23}}{\alpha_2} & \cdots & \frac{p_{2n}}{\alpha_2} \\ \frac{p_{31}}{\alpha_3} & \frac{p_{32}}{\alpha_3} & 0 & \cdots & \frac{p_{3n}}{\alpha_3} \\ \vdots & \vdots & \vdots & \ddots & \vdots \\ \frac{p_{n1}}{\alpha_n} & \frac{p_{n2}}{\alpha_n} & \frac{p_{n3}}{\alpha_n} & \cdots & 0 \end{pmatrix} \\ &= \begin{pmatrix} 0 & \langle t_1 \rangle p_{12} & \langle t_1 \rangle p_{13} & \cdots & \langle t_1 \rangle p_{1n} \\ \langle t_2 \rangle p_{21} & 0 & \langle t_2 \rangle p_{23} & \cdots & \langle t_2 \rangle p_{2n} \\ \langle t_3 \rangle p_{31} & \langle t_3 \rangle p_{32} & 0 & \cdots & \langle t_3 \rangle p_{3n} \\ \vdots & \vdots & \vdots & \ddots & \vdots \\ \langle t_n \rangle p_{n1} & \langle t_n \rangle p_{n2} & \langle t_n \rangle p_{n3} & \cdots & 0 \end{pmatrix}. \end{aligned} \quad (\text{A.9})$$

Evidently, $\tilde{\mathbf{P}}$ is a stochastic matrix. Because the chain $\tilde{\mathbf{P}}$ is reversible, its detailed balance condition should be

$$\tilde{\pi}_i \tilde{p}_{ij} = \tilde{\pi}_j \tilde{p}_{ji}, \quad (\text{A.10})$$

where the vector $\tilde{\boldsymbol{\pi}} = (\tilde{\pi}_1, \dots, \tilde{\pi}_n)^T$ represents the stationary distribution for the chain $\tilde{\mathbf{P}}$. The detailed balance conditions are fulfilled if $\tilde{\pi}_i$ is expressed in terms of π_i as

$$\tilde{\pi}_i = \frac{\pi_i \alpha_i}{\sum_{j=1}^n \pi_j \alpha_j} = \frac{\pi_i / \langle t_i \rangle}{\sum_{j=1}^n \pi_j / \langle t_j \rangle}. \quad (\text{A.11})$$

Conversely, π_i is written in terms of $\tilde{\pi}_i$, as follows:

$$\pi_i = \frac{\tilde{\pi}_i / \alpha_i}{\sum_{j=1}^n \tilde{\pi}_j / \alpha_j} = \frac{\tilde{\pi}_i \langle t_i \rangle}{\sum_{j=1}^n \tilde{\pi}_j \langle t_j \rangle}. \quad (\text{A.12})$$

Therefore, the reversible chain $\tilde{\mathbf{P}}$ should have the stationary distribution $\tilde{\boldsymbol{\pi}}$ given by Eq. (A.11). The zeroes in the diagonal elements of $\tilde{\mathbf{P}}$ represent the chain $\tilde{\mathbf{P}}$ with no self-loop transitions. The matrix $\tilde{\mathbf{P}}$ is the transition kernel of the embedded DTMC that is associated with the continuous-time Markov chains (CTMCs) [62–64], which tracks only the states visited directly after each transition and moves from a state to another state according to the transition probabilities given by $\tilde{\mathbf{P}}$. Equations (A.11) and (A.12) can be interpreted as follows: Because π_i considers the states after the self-loop transition occurring with the probability $p_{ii} = 1 - \alpha_i$, only a fraction α_i of π_i can

contribute to $\tilde{\pi}_i$ on average. Therefore, it is reasonable that $\tilde{\pi}_i \propto \pi_i \alpha_i$ and Eq. (A.11) provide the probability distribution. Note that even if the kernel $\tilde{\mathbf{P}}$ has a stationary distribution $\tilde{\pi}$, it is not necessarily the limiting distribution, as $\tilde{\pi}$ may be a periodic function of the round t of state transition. It is evident that if π is an MB distribution, $\tilde{\pi}$ is not an MB distribution owing to the i -dependence of α_i . Nevertheless, it should be noted that we can recover the MB distribution π from $\tilde{\pi}$ using Eq. (A.12) and $\alpha_i = \sum_{j \neq i} p_{ij}$, which is, in principle, calculable if we can calculate the energy differences between the states.

The RFMC is not merely a theoretical model but can actually be implemented and demonstrated using Monte Carlo simulation. We focus on the RFMC Monte Carlo simulation based on the Metropolis algorithm. When the standard algorithm is applied to an N -spin system, the transition probability from the current state 0 is given by the following Metropolis rule:

$$p_{0i} = \begin{cases} \frac{1}{N} \min \{1, \exp(-\beta \Delta E_i)\} & i \in S_0 \\ 1 - \alpha_0 & i = 0 \\ 0 & \text{otherwise} \end{cases}, \quad (\text{A.13})$$

where S_0 is a set of neighboring states for the current state $i = 0$, that is, the states in which a single spin is flipped, and $\Delta E_i = E_i - E_0$ is the transition energy from the current state 0 to the next state in which the spin i is flipped. Because $p_{00} = 1 - \alpha_0$, it follows that

$$\alpha_0 = \sum_{i \in S_0} p_{0i} = \frac{1}{N} \sum_{i \in S_0} \min \{1, \exp(-\beta \Delta E_i)\}. \quad (\text{A.14})$$

Therefore, α_0 (p_{00}) represents the acceptance (rejection) probability for flipping the spin. We can also regard it as the escaping (trapping) probability that the standard MC will move away from (stay in) the current state in the next step. Then, the ensemble sampled by the standard Monte Carlo simulation approaches the stationary as well as limiting distribution given by Eq. (A.8), i.e., the MB distribution. From Eq. (A.9), it follows that the transition kernel of the RFMC is given by the transition probability

$$\tilde{p}_{0i} = \begin{cases} \frac{p_{0i}}{\sum_{i \in S_0} p_{0i}} & i \in S_0 \\ 0 & \text{otherwise} \end{cases} \quad (\text{A.15})$$

The random choice of the next state to move with the transition probability p_{0i} can be implemented by making use of the conventional acceptance-rejection (AR) method using a pseudo random number generator. In contrast, the random choice of the next state with the transition probability \tilde{p}_{0i} can be implemented by making use of various algorithms for generating a non-uniform random variate, as shown in the following, although their calculations are more expensive than that of the conventional AR method.

In fact, the RFMC was demonstrated through the Monte Carlo simulation using the following toy model. Consider $N = 3$ ($n = 2^N = 8$) spins described by the following Ising Hamiltonian:

$$H(\{s_1, s_2, s_3\}) = \sum_{i=1}^N h_i s_i + \sum_{i,j=1}^N J_{ij} s_i s_j \quad (\text{A.16})$$

with

$$\{h_1, h_2, h_3, J_{12}, J_{13}, J_{23}, \text{others}\} = \{+2, +1, 0, +1, -2, -1, 0\}. \quad (\text{A.17})$$

Table A.1 shows the eight possible spin configurations and associated energies, and Fig. A.1 depicts the energy spectrum of the associated density of states ρ . The transition kernels of the standard MC and RFMC are given by

i	(s_1, s_2, s_3)	Energy
1	(-1, -1, -1)	-5
2	(-1, -1, +1)	+1
3	(-1, +1, -1)	-1
4	(+1, -1, -1)	-1
5	(-1, +1, +1)	-3
6	(+1, -1, +1)	+1
7	(+1, +1, -1)	+7
8	(+1, +1, +1)	+1

TABLE A.1. Possible spin configurations and associated energies for our toy model with $N = 3$ spins.

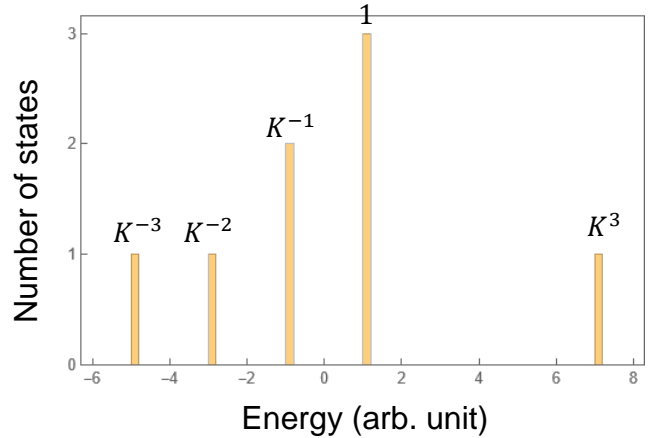


FIG. A.1. Energy spectrum of the associated density of states for our toy model with $N = 3$ spins. The symbols ($K^{-3}, K^{-2}, \dots, K^3$) indicate the relative ratios of the probability distribution for the stationary MB distribution π in Eq. (A.20).

$$\mathbf{P} = \frac{1}{3} \begin{pmatrix} -K^3 - 2K^2 + 3 & K^3 & K^2 & K^2 & 0 & 0 & 0 & 0 \\ 1 & 0 & 0 & 0 & 1 & 1 & 0 & 0 \\ 1 & 0 & -K^4 + 1 & 0 & 1 & 0 & K^4 & 0 \\ 1 & 0 & 0 & -K^4 - 2K + 2 & 0 & K & K^4 & 0 \\ 0 & K^2 & K & 0 & -2K^2 - K + 3 & 0 & 0 & K^2 \\ 0 & 1 & 0 & 1 & 0 & 0 & 0 & 1 \\ 0 & 0 & 1 & 1 & 0 & 0 & 0 & 1 \\ 0 & 0 & 0 & 0 & 1 & 1 & K^3 & -K^3 + 1 \end{pmatrix}, \quad (\text{A.18})$$

$$\tilde{\mathbf{P}} = \begin{pmatrix} 0 & \frac{K}{K+2} & \frac{1}{K+2} & \frac{1}{K+2} & 0 & 0 & 0 & 0 \\ \frac{1}{3} & 0 & 0 & 0 & \frac{1}{3} & \frac{1}{3} & 0 & 0 \\ \frac{1}{K^4+2} & 0 & 0 & 0 & \frac{1}{K^4+2} & 0 & \frac{K^4}{K^4+2} & 0 \\ \frac{1}{K^4+K+1} & 0 & 0 & 0 & 0 & \frac{K}{K^4+K+1} & \frac{K^4}{K^4+K+1} & 0 \\ 0 & \frac{K}{2K+1} & \frac{1}{2K+1} & 0 & 0 & 0 & 0 & \frac{K}{2K+1} \\ 0 & \frac{1}{3} & 0 & \frac{1}{3} & 0 & 0 & 0 & \frac{1}{3} \\ 0 & 0 & 1 & 1 & 0 & 0 & 0 & 1 \\ 0 & 0 & 0 & 0 & \frac{1}{K^3+2} & \frac{1}{K^3+2} & \frac{K^3}{K^3+2} & 0 \end{pmatrix}, \quad (\text{A.19})$$

respectively, where $K = \exp(-2\beta)$. The transition

kernels \mathbf{P} and $\tilde{\mathbf{P}}$ have the left eigenvectors of the eigen-equation with eigenvalue $\lambda = 1$, which offer the stationary distributions

$$\boldsymbol{\pi} = \mathcal{N}[(K^{-3}, 1, K^{-1}, K^{-1}, K^{-2}, 1, K^3, 1)]^T, \quad (\text{A.20})$$

$$\tilde{\boldsymbol{\pi}} = \mathcal{N}\left[\left(\frac{1+2K^{-1}}{3}, 1, \frac{K^3+2K^{-1}}{3}, \frac{K^3+1+K^{-1}}{3}, \frac{2+K^{-1}}{3}, 1, K^3, \frac{K^3+2}{3}\right)\right]^T, \quad (\text{A.21})$$

where $\mathcal{N}[\dots]$ denotes the consideration of a normalized vector. The stationary distribution $\boldsymbol{\pi}$ is the MB distribution. Figure A.2 depicts the energy spectra of $\boldsymbol{\pi}$ and $\tilde{\boldsymbol{\pi}}$ when $K = 0.25$ is assumed. Note that the density of states $\boldsymbol{\rho}$ was considered in these spectra. Evidently, these energy spectra differ.

We performed Monte Carlo simulations to confirm whether these stationary states are actually reproduced. We compared the following three algorithms for the Monte Carlo simulations: (a) Standard MC: Fig. A.3 (a) shows the block diagram of the standard MC. The Metropolis method was used in this simulation. We generated a uniform random number $U(1, N) \in \mathbb{N}$ to select a spin to be flipped in the next state transition and a uniform random variate $U(0, 1) \in \mathbb{R}$ to determine whether it was accepted or rejected for flipping its sign. If the energy ΔE_i required to flip the chosen spin i is such that $\beta \Delta E_i < -\ln U(0, 1)$, it is accepted; otherwise, it is rejected. We can easily obtain the required elements of the kernel \mathbf{P} sweep by sweep in the standard MC iteration. In the standard MC algorithm, all the spin states are recorded as the sampled data, regardless of

whether the chosen spin is accepted or rejected for flipping, which is analyzed after the completion of the simulation. (b) Rejection-discarded MC: Fig. A.3 (b) shows the modified version of the standard MC. This algorithm differs from (a) in the recording of the sampled data. Only the spin states after the accepted transitions are recorded as the sampled data and those after the rejected transitions are discarded. Because the states after the rejected transitions are the same as those before it, discarding the state directly after the rejected transition implies disregarding the states associated with the self-loop transitions. (c) RFMC: To realize the kernel $\tilde{\mathbf{P}}$, we apply the algorithm for the non-uniform random number generation. The algorithm generates a set of N exponential random variables $\{\tau_1, \dots, \tau_N\}$, each of which is characterized by its own rate parameter p_{0i} , e.g., $\tau_i \sim \text{Exponential}(p_{0i})$. The random variable τ_i is regarded as the holding time required to flip the spin i in the CTMC. We accept the smallest of these and flip the corresponding spin. According to the properties of the exponential random variate, the associated probability is

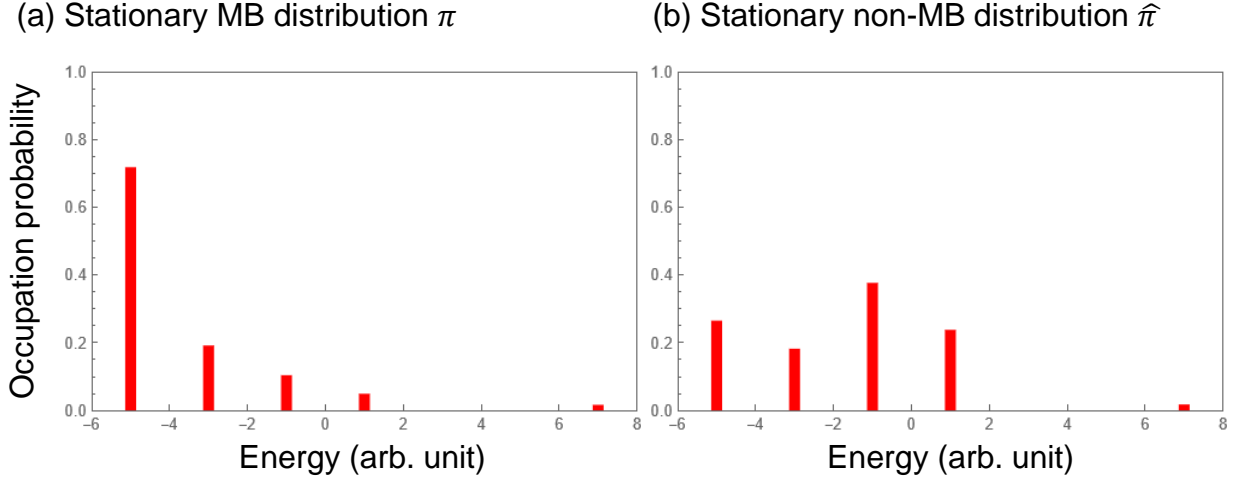


FIG. A.2. Energy spectra of stationary distributions π and $\tilde{\pi}$ when $K = 0.25$ is assumed.

given by

$$\Pr\left(\tau_i = \min_i \{\tau_1, \dots, \tau_N\}\right) = \frac{p_{0i}}{\sum_{i=1}^N p_{0i}}. \quad (\text{A.22})$$

This is a well-known non-uniform random number generation (or weighted random choice) algorithm for selecting one item from N items according to the weight $\{p_{01}, \dots, p_{0N}\}$ [35]. Thus, we can obtain the required elements in the transition kernel $\tilde{\mathbf{P}}$ recursively in the MC iteration. In this algorithm, all spin states directly after flipping the selected spin are recorded as the sampled data.

We performed Monte Carlo simulations using the three algorithms to obtain a sufficiently large quantity of sampled data and compared the energy spectra of their stationary distributions with those shown in Fig. A.2. Figure A.4 shows the energy spectra for the stationary distributions and associated temporal developments for the sampled data. The rounds of MC iterations were adjusted so that the number of spin flips was approximately 5000 in these simulations. The temporal developments of the energy of the spin system associated with the last 200 of the sampled data are shown in the lower plots of Fig. A.4. The computation times of algorithms (a) and (b) were comparable but that of algorithm (c) was approximately half.

We can observe that once the spins are trapped at a lower-energy state, numerous trials to flip are required to escape from such a state to the next state in the temporal profiles in Fig. A.4 (a), which is accounted for by the self-loop transitions. In contrast, such state trapping is not observed in Fig. A.4 (b) and (c). The number of trials to flip that is required to escape from the trapped state is a geometric random variable $\tau \sim \text{Geometric}(\alpha_0)$ associated with the trapped state 0 in which the average number is given by $\langle \tau \rangle = \frac{1}{\alpha_0}$. Note

that α_0 depends on the trapped state and changes after every spin flip. In addition, there are two points to note. The first is that the short trapping to the states with energy = +1 in the lower plots of Fig. A.4 is not attributed to the self-loop transition, but to the transition among the energetically degenerated states. The second is that the chain $\tilde{\mathbf{P}}$ has a left eigenvalue -1 so that the stationary distribution $\tilde{\pi}$ is not the limiting distribution [69]. This is because the MC with no self-loop transition is never aperiodic and exhibits oscillatory behavior with period $d > 1$, as shown in Fig. A.4 (b) and (c). These differences in the temporal developments for the algorithms are directly reflected in their energy spectra. Figure A.4 also depicts the energy spectra of the stationary distributions for the three algorithms. The energy spectrum for algorithm (a) agrees with the MB distribution π associated with the transition kernel \mathbf{P} . In contrast, the energy spectra for algorithms (b) and (c) agree with the non-MB distribution $\tilde{\pi}$ associated with the kernel $\tilde{\mathbf{P}}$. Therefore, the temporal developments as well as the energy spectra of algorithms (b) and (c) agree. This implies that the difference between two stationary distributions π and $\tilde{\pi}$ originates from any immediately repeated state after the transition, i.e., self-loop transition. In fact, we can confirm that the MB distribution π reproduces the temporal development and spectra for the non-MB distribution $\tilde{\pi}$ if we simply omit these states due to the self-loop transitions.

We should emphasize that the self-loop transitions also play an important role in sampling the ground state of the Ising spins by Monte Carlo simulation. If we simulate a standard reversible MC using the Monte Carlo method, a sampled series converges to the MB distribution after a sufficiently large number of transitions. Then, if we maintain the spin systems at a low temperature, the lower energy portion of the MB distribution π increases so that the sampling probability of the ground state

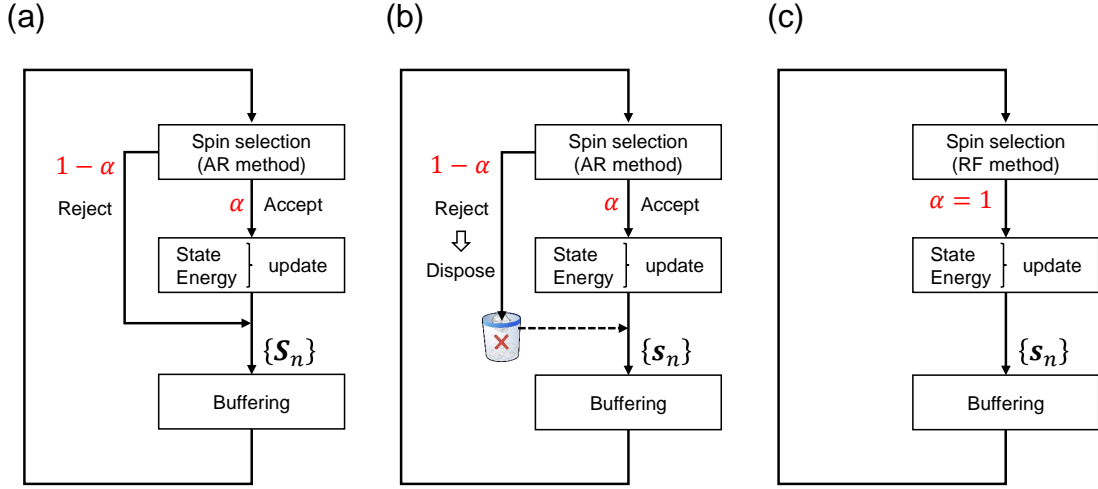


FIG. A.3. Comparison of three algorithms for MCMC simulation: (a) standard MC, (b) rejection-discarded MC, and (c) RFMC.

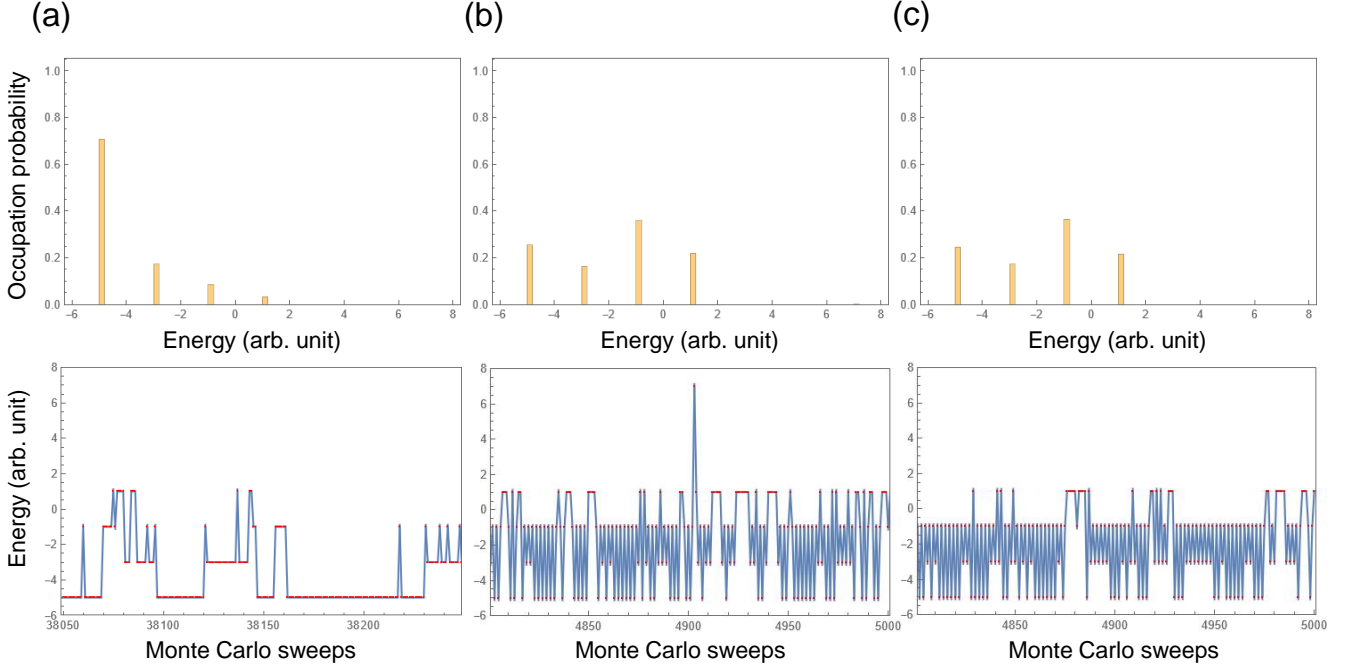


FIG. A.4. Energy spectra of the occupation probability and associated temporal development for the sampled data associated with algorithms (a)-(c).

increases. However, this is necessarily accompanied by a decreased acceptance probability α_0 for the low lying state and an associated increase in the number of repeated states immediately after the transition owing to self-loop transition. The presence of the low-lying excited states may affect the time required for successfully sampling the ground state, as not only the ground state but also the low-lying excited states have a large self-loop transition probability. Once the system is trapped

to one such low-lying excited state, many sweeps would be wasted before a successful escape from the trapped state. Thus, extra time is required to sample the ground state successfully. This deceleration in sampling the ground state has been frequently pointed out as a serious problem in simulated annealing. Although this problem may be relaxed by dynamically controlling the hyperparameters such as the temperature to a certain extent, the approach has limited benefits. This is a

common problem for conventional simulated annealing that reads out the state at an arbitrary timing as a sample using a trial-and-error approach. Therefore, mutually incompatible requirements exist regarding self-loop transitions: increasing the probability of the self-loop transitions is desirable to increase the sampling efficiency for the ground state, whereas decreasing it is desirable to quickly approach the MB distribution as well as the ground state quickly.

RFMC offers the potential to overcome this situation. Because it has no self-loop transition, it approaches its stationary distribution more rapidly than the standard MC method. The drawback of the trial-and-error sampling approach can be overcome by keeping track of the spin state as well as its energy sweep by sweep and updating the bookkeeping to hold the best state to find the ground state. This can be easily incorporated into the Monte Carlo simulation. We should note that although the stationary distribution of the RFMC deviates from the MB distribution, we can recover the MB distribution by implementing the additional calculation required to recover it. Because the RFMC considers the same chain as the standard DTMC, except for the omission of any repeated states owing to self-

loop transitions, it loses the information on the waiting time for a chain of readout states. Suppose that the k th state in an RFMC chain is obtained by omitting M_k repetitions of the states owing to the self-loop transition in the standard DTMC [64]. Then, the multiplicity $M_k \sim \text{Geometric}(\alpha_0(k)) + 1$ is lost, where $\alpha_0(k)$ is the acceptance rate for the k th state. This lost information can be easily calculated during the iterations of the Monte Carlo simulation because the set $\{p_{01}, \dots, p_{0N}\}$ of the transition probability is necessarily calculated to choose the next spin state in the RFMC algorithm, which can be accomplished relatively inexpensively by keeping track of the bookkeeping list $\{\Delta E_1, \dots, \Delta E_n\}$. Then, we can calculate the acceptance rate $\alpha_0 = \sum_{i \in S_0} p_{0i}$

and multiplicity $M \sim \left\lfloor \frac{\ln U(0,1)}{\ln(1-\alpha_0)} \right\rfloor + 1$ for the current state sweep by sweep to form the multiplicity list M_k , which is the number of times that the standard chain remains in the same state after the transition, where $\lfloor x \rfloor$ denotes the integer part of x and the well-known formulae $\text{Geometric}(\lambda) = \lfloor \text{Exponential}(-\ln(1-\lambda)) \rfloor$ and $\text{Exponential}(\lambda) = -\frac{\ln U(0,1)}{\lambda}$ are used to express M [61, 64].

-
- [1] S. Kirkpatrick, C. D. Gelatt, and M. P. Vecchi, *Science* **220**, 671 (1983).
- [2] T. Kadowaki and H. Nishimori, *Phys. Rev. E* **58**, 5333 (1998).
- [3] V. Choi, *Quantum Inf. Process.* **7**, 193 (2008).
- [4] V. Choi, *Quantum Inf. Process.* **10**, 343 (2011).
- [5] W. Lechner, P. Hauke, and P. Zoller, *Sci. Adv.* **1**, e1500838 (2015).
- [6] W. Vinci, T. Albash, G. Paz-Silva, I. Hen, and D. A. Lidar, *Phys. Rev. A* **92**, 042310 (2015).
- [7] N. Sourlas, *Phys. Rev. Lett.* **94**, 070601 (2005).
- [8] S. Puri, C. K. Andersen, A. L. Grimsmo, and A. Blais, *Nat. Commun.* **8**, 1 (2017).
- [9] T. Albash, W. Vinci, , and D. A. Lidar, *Phys. Rev. A* **94**, 022327 (2016).
- [10] S. Ding, G. Maslennikov, R. Hablützel, H. Loh, and D. Matsukevich, *Phys. Rev. Lett.* **119**, 150404 (2017).
- [11] A. Grimm, N. E. Frattini, S. Puri, S. O. Mundhada, S. Touzard, M. Mirrahimi, S. M. Girvin, S. Shankar, and M. H. Devoret, *Nature* **584**, 205 (2020).
- [12] N. E. Frattini, R. G. Cortiñas, J. Venkatraman, X. Xiao, Q. Su, C. U. Lei, B. J. Chapman, V. R. Joshi, S. M. Girvin, R. J. Schoelkopf, S. Puri, and M. H. Devoret, “The squeezed kerr oscillator: spectral kissing and phase-flip robustness,” arXiv:2209.03934v1 [quant-ph].
- [13] Z. Wang, M. Pachal, E. A. Wollback, and P. Arrangoiz-Arriola, *Phys. Rev. X* **9**, 021049 (2019).
- [14] T. Yamaji, S. Kagami, A. Yamaguchi, T. Satoh, K. Koshino, H. Goto, Z. R. Lin, Y. Nakamura, and T. Yamamoto, *Phys. Rev. A* **105**, 023519 (2022).
- [15] T. Yamaji, S. Masuda, A. Yamaguchi, T. Satoh, A. Morioka, Y. Igarashi, M. Shirane, and T. Yamamoto, *Phys. Rev. Appl.* **20**, 014057 (2023).
- [16] N. Chancellor, S. Zohren, and P. A. Warburton, *NPJ Quantum Inf.* **3**, 1 (2017).
- [17] S. P. Jordan, E. Farhi, and P. W. Shor, *Phys. Rev. A* **74**, 052322 (2006).
- [18] K. C. Young, R. Blume-Kohout, and D. A. Lidar, *Phys. Rev. A* **88**, 062314 (2013).
- [19] K. L. Pudenz, T. Albash, and D. A. Lidar, *Nat. Commun.* **5**, 3243 (2014).
- [20] K. L. Pudenz, T. Albash, and D. A. Lidar, *Phys. Rev. A* **91**, 042302 (2015).
- [21] A. D. Bookatz, E. Farhi, and L. Zhou, *Phys. Rev. A* **92**, 022317 (2015).
- [22] S. Matsuura, H. Nishimori, T. Albash, and D. A. Lidar, *Phys. Rev. Lett.* **116**, 220501 (2016).
- [23] S. Matsuura, H. Nishimori, W. Vinci, T. Albash, and D. A. Lidar, *Phys. Rev. A* **95**, 22308 (2017).
- [24] A. Pearson, A. Mishra, I. Hen, and D. A. Lidar, *NPJ Quantum Inf.* **5** (2019).
- [25] F. Pastawski and J. Preskill, *Phys. Rev. A* **93**, 52325 (2016).
- [26] J. L. Massey, *Threshold decoding*, Ph.D. thesis, Massachusetts Institute of Technology, Research Laboratory of Electronics (1962).
- [27] J. L. Massey, in *Advances in Communication Systems*, Vol. 3, edited by A. Balakrishnan (Elsevier, 1968) pp. 91–115.
- [28] C. Laferriere, “Error correcting capability of 1-step majority logic decoding,” <http://hdl.handle.net/10393/10473> (1977).
- [29] G. J. C. Clerk and B. J. Cain, *Error-Correction Coding for Digital Communications* (Plenum Press, 1981).
- [30] L. Shu and J. J. D. Costello, *Error Control Coding: fundamentals and applications*, 2nd ed. (Pearson Prentice

- Hall, NJ, 2004).
- [31] N. Sourlas, *Physica A* **302**, 14 (2001).
- [32] N. Sourlas, in *Winter School on Complex Systems*, edited by J. Mazoyer, M. Morvan, and N. Schabanel (IXXI, Lyon, 2002).
- [33] D. Gottesman, *Phys. Rev. A* **54**, 1862 (1996).
- [34] R. Vicente, D. Saad, and Y. Kabashima, in *Advances in Imaging and Electron Physics*, Vol. 125 (Elsevier, 2003) pp. 231–353.
- [35] Y. Nambu, *IEEE Access* **10**, 84279 (2022).
- [36] A. Rocchetto, S. C. Benjamin, and Y. Li, *Sci. Adv.* **2** (2016).
- [37] K. Ender, A. Messinger, M. Fellner, C. Daska, and W. Lechner, *PRX Quantum* **3**, 030304 (2022).
- [38] M. Fellner, A. Messinger, K. Ender, and W. Lechner, *Phys. Rev. Lett.* **129**, 180503 (2022).
- [39] F. G. Fuchs, K. O. Lye, H. M. Nilsen, A. J. Stasik, and G. Sartor, *Algorithms* **15**, 202 (2022).
- [40] A. Weidinger, G. B. Mbeng, and W. Lechner, (2023), arXiv:2301.05042v1 [quant-ph].
- [41] A. Messinger, M. Fellner, and W. Lechner, “Constant depth code deformations in the parity architecture,” (2023), arXiv:2303.08602v1 [quant-ph].
- [42] M. S. Kozl, G. Mazzola, A. J. Ochoa, H. G. Katzgraber, and M. Troyer, *Phys. Rev. A* **100** (2019).
- [43] R. Martoňák, G. E. Santoro, and E. Tosatti, *Phys. Rev. B* **66**, 094203 (2002).
- [44] B. Heim, T. F. Ronnow, S. V. Isakov, and M. Troyer, *Science* **348**, 215 (2015).
- [45] H. M. Waidyasooriya and M. Hariyama, *IEEE Access* **8**, 67929 (2020).
- [46] J. Hu and Y. Wang, *J. Comput. Graph. Stat.* **30**, 284 (2021).
- [47] W. Vinci, T. Albash, and D. A. Lidar, *NPJ Quantum Inf.* **2**, 1 (2016).
- [48] A. B. Dodds, V. Kendon, C. S. Adams, and N. Chancellor, *Phys. Rev. A* **100**, 032320 (2019).
- [49] H. Nishimori, *J. of Phys. Soc. Japan* **62**, 2973 (1993).
- [50] P. Rujan, *Phys. Rev. Lett.* **70**, 2968 (1993).
- [51] H. Nishimori and K. Y. M. Wong, *Phys. Rev. E* **60**, 132 (1999).
- [52] N. Chancellor, S. Szoke, W. Vinci, G. Aeppli, and P. A. Warburton, *Sci. Rep.* **6**, 22318 (2016).
- [53] H. Tanaka, K. Furusawa, and S. Kaneku, *IEEE Trans. Inf. Theory* **IT-26**, 244 (1980).
- [54] L. Rudolph and W. Robbins, *IEEE Trans. Inf. Theory* **IT-18**, 446 (1972).
- [55] D. A. Lidar, *Phys. Rev. A* **100**, 022326 (2019).
- [56] K. C. Young, M. Sarovar, and R. Blume-Kohout, *Phys. Rev. X* **3**, 041013 (2013).
- [57] M. Sarovar and K. C. Young, *New J. Phys.* **15**, 125032 (2013).
- [58] M. H. Amin, *Phys. Rev. A* **92**, 052323 (2015).
- [59] M. Benedetti, J. Realpe-Gomez, R. Biswas, and A. Perdomo-Ortiz, *Phys. Rev. A* **94**, 22308 (2016).
- [60] J. Marshall, D. Venturelli, I. Hen, and E. G. Rieffel, *Phys. Rev. Appl.* **11**, 044083 (2019).
- [61] H. Watanabe, S. Yukawa, M. A. Novotny, and N. Ito, *Phys. Rev. E* **74**, 026707 (2006).
- [62] R. R. Mazumdar, “Continuous-time markov chains (ctmc),” https://ece.uwaterloo.ca/~mazum/ECE605_2012/Notes/MarkovChains_CTMC.pdf (2012).
- [63] S. Parekh, “Continuous time markov chains,” <https://inst.eecs.berkeley.edu/~ee126/fa20/notes/ctmcs.pdf> (2020).
- [64] J. S. Rosenthal, A. Dote, K. Dabiri, H. Tamura, S. Chen, and A. Sheikholeslami, *Comput. Stat.* **36**, 2789 (2021).
- [65] Y. Iba, *Int. J. Mod. Phys. C* **12**, 623 (2001).
- [66] Y. Iba, *Trans. Jpn. Soc. Artif. Intell.* **16**, 279 (2001).
- [67] F. Campillo, R. Rakotozafy, and V. Rossi, *Math. Comput. Simul.* **79**, 3424 (2009).
- [68] O. Cappe, A. Guillin, J. M. Marin, and C. P. Robert, *J. Comput. Graph. Stat.* **13**, 907 (2004).
- [69] E. Seabrook and L. Wiskott, “A tutorial on the spectral theory of markov chains,” (2022), arXiv:2207.02296v2 [cs.LG].
- [70] J. J. Hopfield and D. W. Tank, *Science* **233**, 625 (1986).
- [71] N. Sourlas, *Nature* **339**, 693 (1989).
- [72] H. Goto, K. Tatsumura, and A. R. Dixon, *Sci. Adv.* **5**, eaav2372 (2019).
- [73] T. Inagaki, Y. Haribara, K. Igarashi, T. Sonobe, S. Tamate, T. Honjo, A. Marandi, P. L. McMahon, T. Umeki, K. Enbutsu, O. Tadanaga, H. Takenouchi, K. Aihara, K. Kawarabayashi, K. Inoue, S. Utsunomiya, and H. Takesue, *Science* **354**, 603 (2016).
- [74] I. Marvian and D. A. Lidar, *Phys. Rev. Lett.* **113**, 260504 (2014).
- [75] M. Marvian and D. A. Lidar, *Phys. Rev. Lett.* **118**, 030504 (2017).